

A RAYLEIGH - BRILLOUIN SPECTROPHOTOMETER

Thesis for the Degree of Ph. D.

MICHIGAN STATE UNIVERSITY

STUART J. GAUMER

1973

This is to certify that the

thesis entitled

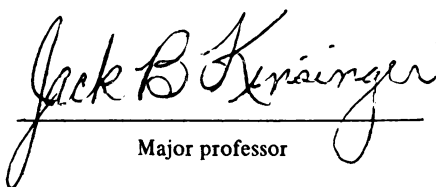
A Rayleigh-Brillouin Spectrophotometer

presented by

Stuart J. Gaumer

has been accepted towards fulfillment  
of the requirements for

Ph.D. degree in Chemistry

  
Major professor

Date February 20, 1973









## ABSTRACT

### A RAYLEIGH-BRILLOUIN SPECTROPHOTOMETER

By

Stuart J. Gaumer

A Rayleigh-Brillouin spectrophotometer was designed, constructed, and characterized. This instrument consists of: (1) a vibration free optical table, (2) a variable scattering angle mechanism, (3) a temperature controlled sample cell system, (4) lasers, (5) a piezo-electrically scanned Fabry-Perot interferometer and, (6) an analog electronic detection system augmented by a photon-counting-digital-data collection system. Furthermore, in order to provide versatility, the optics may easily be changed to accommodate different types of scattering experiments.

The versatility, accuracy and precision of this apparatus were characterized by performing some classical Rayleigh light scattering experiments, measurement of depolarization ratios and their temperature and wavelength dependence, and some more modern experiments such as the evaluation of polarization coherency matrix elements and high resolution Brillouin spectra. While the spectrometer was

being characterized, several techniques for its alignment and calibration were developed.

Computer programs were written to analyze the Brillouin spectra data for pure liquids in terms of the linearized hydrodynamic theory. These computer programs were used on "theoretical data sets" in order to help specify what accuracy and precision were needed in the spectra in order to deduce fundamental thermodynamic parameters characterizing a liquid.

A RAYLEIGH-BRILLOUIN SPECTROPHOTOMETER

By

Stuart J. Gaumer

A THESIS

Submitted to  
Michigan State University  
in partial fulfillment of the requirements  
for the degree of

DOCTOR OF PHILOSOPHY

Departments of Chemistry and Physics

1973

G-86308

## ACKNOWLEDGMENTS

The author wishes to express his thanks to the National Science Foundation, the National Institute of Health and the chemistry department of Michigan State University for the fellowships and assistantships providing financial support for his family.

The author is very grateful to the graduate students in his research group, especially L. R. Dosser, for their innumerable hours of thought provoking discussion. He is also thankful to the glassblowers and machinist for many hours of discussion relative to the design and construction of the instrumental system.

The author wishes to express appreciation to Professor J. B. Kinsinger for his counsel and guidance. Dr. Kinsinger has been very encouraging, understanding and critical.

Lastly, the author is extremely indebted to his wife, Fran, children Mary Kay, Steven, and Matthew for their endurance of these difficult times and for their unlimited encouragement.

## TABLE OF CONTENTS

	Page
ACKNOWLEDGEMENT . . . . .	ii
LIST OF TABLES . . . . .	vi
LIST OF FIGURES . . . . .	vii
Chapter	
I. INTRODUCTION . . . . .	1
Modern Interest in Light Scattering . . . . .	1
Purpose of this Research . . . . .	8
Identification of Brillouin Spectra . . . . .	8
II. THEORETICAL FORMULISM . . . . .	15
Electromagnetic Theory of Liquid Light Scattering . . . . .	15
Linearized Hydrodynamic Liquid Theory . . . . .	18
Fabry-Perot Interferometry . . . . .	22
Polarization Coherency Matrix . . . . .	30
Convolution and Deconvolution . . . . .	34
III. DATA ANALYSIS TECHNIQUES . . . . .	38
Introduction . . . . .	38
Spectra Deconvolution . . . . .	39
Brillouin Spectra Simulation . . . . .	40
Brillouin Spectra Parameter Estimation . . . . .	44
IV. INSTRUMENTAL SYSTEM . . . . .	59
General Design Aspects-Introduction . . . . .	59
Optical Table . . . . .	63
Light Sources . . . . .	66
Traditional Light Sources . . . . .	66
Lasers . . . . .	67
Argon Ion Laser . . . . .	69
Incident Optics . . . . .	70
Sample Cell System . . . . .	71
Variable Scattering Angle Mechanism . . . . .	71
Sample Cell and Thermostatting Jacket . . . . .	74
Temperature Controller . . . . .	79
Temperature Monitor . . . . .	80

Chapter	Page
Collection Optics and Beam Analyzer . . . . .	87
Interferometer Subsystem . . . . .	91
Interferometer . . . . .	91
High Voltage Scanner . . . . .	93
Mirrors . . . . .	94
Stability . . . . .	96
Post-Interferometer Optics . . . . .	97
Detection Electronics . . . . .	100
Introduction . . . . .	100
Photomultiplier Tube, Housing, and Power Supply . . . . .	102
Picoammeter . . . . .	105
Recorders . . . . .	106
Photon Counting . . . . .	107
Digital Control Unit . . . . .	109
V. ALIGNMENT AND CALIBRATION TECHNIQUES . . . . .	118
Introduction . . . . .	118
Optical Table Leveling . . . . .	118
Initial Assembly . . . . .	119
Collection Optics Alignment . . . . .	121
Interferometer Alignment . . . . .	122
Post-Interferometer Alignment . . . . .	124
Incident Laser Beam Alignment . . . . .	125
Sample Cell Positioning . . . . .	126
Interferometer Calibration . . . . .	127
Temperature Calibration . . . . .	129
Polarization Alignment and Calibration . . . . .	131
Introduction . . . . .	131
Theoretical Discussion . . . . .	132
Experimental Technique . . . . .	147
VI. SAMPLE PREPARATION AND HANDLING . . . . .	151
VII. EXPERIMENTAL RESULTS . . . . .	153
Temperature Dependence of Depolarization Ratio . . . . .	153
Wavelength Dependence of Benzene Depolarization Ratio . . . . .	163
Polarization Coherency Matrix for Benzene Scattered Light . . . . .	165
Angular Dependence of Light Scattering . . . . .	170
Landau-Placzek Ratio and Relative Brillouin Shift for Glycerine . . . . .	173
Brillouin Spectra of Carbon Tetrachloride . . . . .	181

Chapter	Page
VIII. CONCLUSIONS . . . . .	188
Summary . . . . .	188
Future Research . . . . .	189
BIBLIOGRAPHY . . . . .	192
APPENDIX . . . . .	199



# LIST OF TABLES

Table	Page
2.1. Instrumental Parameters for Fabry-Perot Interferometer . . . . .	29
3.1. First Data Card for BRILSPEC . . . . .	42
3.2. Second Data Card for BRILSPEC . . . . .	42
3.3. Parameter Data Cards for BRILSPEC . . . . .	43
3.4. Program Parameters for BSPEP . . . . .	56
5.1. Platinum Resistance Thermometer Calibration . .	130
7.1. Depolarization Ratio Versus Temperature for Benzene . . . . .	156
7.2. Depolarization Ratio Versus Temperature for Carbon Tetrachloride . . . . .	157
7.3. Analysis of Benzene Depolarization Data . . .	160
7.4. Analysis of Carbon Tetrachloride Depolarization Data . . . . .	161
7.5. Vertical Depolarization Ratio Versus Wavelength for Benzene . . . . .	164
7.6. Polarization Coherency Matrix Data for Benzene .	168
7.7. Angular Dependence of Light Scattering Data . .	172
7.8. Landau-Placzek Ratio and Relative Brillouin Shift for Glycerine . . . . .	178
7.9. Theoretical and Experimental Values for Carbon Tetrachloride Brillouin Spectra Parameters .	184

## LIST OF FIGURES

Figure	Page
1. 1. Typical Brillouin-Raman Spectrum . . . . .	10
1. 2. Classical Description of Brillouin Spectra . . .	12
1. 3. Quantum Mechanical Description of Brillouin Spectra . . . . .	13
2. 1. Fabry-Perot Interferometry . . . . .	25
3. 1. Trilorentzian Model with Parameter Set A . . .	45
3. 2. Trilorentzian Model with Parameter Set B . . .	46
3. 3. Trilorentzian Model with Parameter Set C . . .	47
3. 4. Initial Curve Fit for Single Relaxation Model . . . . .	48
3. 5. Final Curve Fit for Single Relaxation Model . . .	49
3. 6. Initial Curve Fit for Trilorentzian Model . . .	50
3. 7. Final Curve Fit for Trilorentzian Model . . .	51
3. 8. Flow Chart for BSPEP . . . . .	55
4. 1. Rayleigh-Brillouin Spectrophotometer . . . . .	60
4. 2. Optical Table . . . . .	64
4. 3. Thermostatted Sample Cell . . . . .	75
4. 4. Corrections for Temperature Controller Settings . . . . .	81
4. 5. Block Diagram of Temperature Monitor . . . . .	82
4. 6. Thermilinear Electronics A . . . . .	84
4. 7. Thermilinear Electronics B . . . . .	85

Figure	Page
4. 8. Optical Detection Train . . . . .	88
4. 9. Temperature Correlation of Interferometer Instability . . . . .	98
4.10. Photomultiplier Dark Currents . . . . .	104
4.11. Photon Counter . . . . .	108
4.12. Digital Control Unit Circuitry . . . . .	112
4.13. Logic of Digital Control Unit . . . . .	113
4.14. Piezoelectric Transducer Voltage when Controlled by Digital Control Unit . . . . .	116
5. 1. Coordinate System for Discussion of Polarization Alignment Technique . . . . .	133
5. 2. Reflectances of a Dielectric . . . . .	135
5. 3. Refractive Index Dependence of Incidence Angle Maximizing $r_s - r_p$ . . . . .	142
5. 4. $r_s - r_p$ Dependence on Angle of Incidence for a Refractive Index of 1.5 . . . . .	143
5. 5. Refractive Index Dependence of Brewster Angle .	144
5. 6. Refractive Index Dependence of $r_s - r_p$ . . . . .	146
5. 7. Polarization Alignment . . . . .	149
7. 1. Temperature Dependence of Benzene Depolarization . . . . .	158
7. 2. Temperature Dependence of Carbon Tetrachloride Depolarization . . . . .	159
7. 3. Wavelength Dependence of Benzene Depolarization . . . . .	166
7. 4. Angular Dependence of Light Scattering . . . .	174
7. 5. Temperature Dependence of Landau-Placzek Ratio for Glycerine . . . . .	179
7. 6. Temperature Dependence of Relative Brillouin Shift for Glycerine . . . . .	180

Figure		Page
7. 7.	Brillouin Spectra for Carbon Tetrachloride . .	182
7. 8.	Calculated Brillouin Spectra for Carbon Tetrachloride . . . . .	186
10. 1.	Frequency Stabilized Short Plasma Tube Laser .	200
10. 2.	Frequency Stabilized Long Plasma Tube Laser .	208

## CHAPTER I

### INTRODUCTION

#### Modern Interest in Light Scattering

Since its first recorded observation by Richter (1) in 1802, light scattering has become a useful experimental technique for probing the micro-and macroscopic nature of matter. In 1869, Tyndall (2) discovered that, if the incident radiation was plane polarized, the light scattered by an aerosol was visible in only one plane (perpendicular to the polarization vector) and proposed an explanation based upon the laws of reflection. In 1871 and 1881, Rayleigh (3) showed that the correct explanation was one of diffraction and that the polarization phenomenon was a consequence of Fresnel's theory of wave motion. With Rayleigh's theory, the blue color of daylight and the red-oranges of the setting sun were explained. However, Rayleigh's original treatment, which was based on Maxwell's electromagnetic theory, applies only to independent, transparent, optically isotropic particles small compared to the wavelength of the incident radiation. Using reversible statistical thermodynamics, Einstein, Schmoluchowski and Gans (4) developed a fluctuation

theory which has proven to be useful for light scattering in pure liquids and in mixtures. Mie (5), in 1908, developed a general and rigorous electromagnetic theory of light scattering by spherical, noninteracting "particles" of an arbitrary size. Mie's theory has been particularly useful for analyzing the scattering by particles large compared to the wavelengths of light; this theory has successfully explained many color phenomena.

Originally, the spectra of light scattered by atoms and molecules were assumed to be composed of a single Rayleigh peak corresponding to elastically scattered light. In 1922, Brillouin (30) predicted the spectral distribution of scattered light should have two Doppler shifted peaks corresponding to inelastic scattering from acoustical phonons. In 1928 (6), Raman discovered a different inelastic scattering phenomenon due to the non-linear polarizability and this phenomenon has become a very important complement to infrared spectroscopy for the elucidation of molecular vibrational and rotational motions as well as macroscopic structure.

Now light scattering investigations can be separated into two categories: (1) an investigation of the spectral distribution of the scattered radiation and, (2) photometric studies or the measurement of the total scattered intensity as a function of scattering angle, wavelength of incident radiation, etc. Brillouin and Raman spectroscopy represent

examples of the first type of experiment defined above; traditional Rayleigh and depolarization studies are examples of the second type of experiment.

Debye (7) extended the Rayleigh and Einstein theories to dilute solutions of high molecular weight polymers. During the period 1937-1958, Fixman (8), Zimm (9), and others (10,11,12) improved Einstein's statistical-thermodynamical theory of Rayleigh scattering from a microscopic point of view assuming a scattering medium of small, optically isotropic molecules. In a first approximation, this isotropic scattering is related directly to the two-molecule radial distribution function  $g(\underline{r})$  (whereas, in higher order approximations, it is also related to the multi-molecular radial distribution functions) and provides information about the radial distribution functions in a manner analogous to X-ray, neutron and other scattering experiments. However, most substances consist of nonspherical, optically anisotropic molecules which, even in their pseudo-noninteracting gaseous state, give rise to optical phenomena which are not explained by these isotropic theories. The depolarization of scattered light is an example. In liquids, this anisotropic scattering is related to the angularly dependent molecular interactions given by a more general radial-orientational distribution function  $g(\underline{r}, \omega)$  and it has been discussed by Anselm (13) and others (14,15,16,17). Even though these

theories adequately explain many photometric experiments, they do not explain the spectral distribution of the scattered light.

In the 1960's, Theimer (18), Paul, Frisch (19), Komarov (20) and Fisher have extended Van Hove's (21) X-ray and neutron scattering theory for interacting systems to light scattering; these authors have theoretically related light scattering to  $g(\underline{r}, \omega)$  in a manner which describes the spectral distribution of the scattered light. Mountain (22-27), Nichols and Carome (28), Bhatia and Tong (29) introduced a linearized hydrodynamic phenomenological theory for the description of Brillouin spectra of liquids which implicitly accounts for molecular interactions.

It was not until 1928-1930 that Gross (31) experimentally verified Brillouin's prediction: Soon after the discovery of the Raman effect, Gross attempted to determine whether or not spectral peaks corresponding to the molecule's rotational transitions (analogous to the more evident vibrational transition peaks) were present in the Raman spectra of various organic liquids. These peaks were expected to be situated very close to the central peak of elastically scattered light. In the course of these experiments, Gross discovered that the broadened Rayleigh peak (broad compared to that of a gaseous sample) resolved into a triplet as opposed to a doublet predicted by



Brillouin. In 1934, Landau and Placzek (37) explained this triplet by using the representation  $\epsilon = \epsilon(p, S)$  for the dielectric constant instead of the more common representations  $\epsilon = \epsilon(\rho, T)$  or  $\epsilon = \epsilon(V, T)$ . They calculated the ratio of the intensity of the central peak ( $I_C$ ) to the intensity of the Doppler shifted peaks ( $2I_B$ ) from a classical density fluctuation theory to be

$$\frac{I_C}{2I_B} = \gamma - 1 \quad (1-1)$$

wherein  $\gamma = C_p/C_v$ . Many experimenters have found this relationship to be valid, within experimental error, for many liquids with the notable exceptions of carbon disulfide and carbon tetrachloride. Mountain, Nichols and Carome (28) have recently explained these exceptions essentially by including another nonpropagating density fluctuation.

Cummins and Gammon (32), Stoicheff (33), Rank (34) and his colleagues have recently made careful studies of the state of polarization of the Rayleigh fine structure. They have concluded that the unmodified Rayleigh line and the Brillouin components are highly polarized and that the depolarization of the scattered light is due to a third contribution associated with a highly damped rotational motion.

To date, even though some investigators (35,36,23) have made temperature and viscosity studies, especially

of the central component and on the state of polarization, Brillouin spectra have primarily been used to obtain sound velocities in liquids and to study critical phenomena.

Until the 1960's and apart from Raman spectroscopy, the most important practical application of light scattering photometry has been directed toward the study of high molecular weight polymers and proteins primarily because these studies were least restricted by experimental limitations. Sufficiently high signal-to-noise ratios were obtained only in experiments utilizing green, blue and near ultraviolet light sources. Three primary reasons for these difficulties are: (1) According to Rayleigh's law, the intensity of the scattered light is proportional to  $\lambda^{-4}$ . (2) The most intense light sources available had a dominance of green, blue and near ultraviolet radiations. (3) The available photomultiplier tubes were most sensitive to these wavelengths. These relatively high energies often gave rise to ambiguities due to fluorescence. There were large uncertainties in wavelength because of the associated broad spectral distributions of the incident light. Furthermore, there were additional problems associated with multiple scattering, uncertainty in the geometry of the scattering volume, and optical and electronic noise.

The development of the laser by Maiman (38) and Javan (39) in 1961 has greatly helped to alleviate many of the experimental problems, allowing one to study more

effectively the fine structure of the scattered light spectrum. The laser's radiation is highly monochromatic, highly coherent, well collimated, very intense and available at longer wavelengths. These assets reduce fluorescence, multiple scattering, spatial and temporal uncertainties. Moreover, the highly monochromatic laser light permits one to resolve the fine structure of the scattered light spectrum more completely.

Recent advances in Fabry-Perot interferometry, photomultiplier tube technology, and detection electronics (especially digital photon counting equipment) also represent significant improvements in the experimental techniques available.

In summary, the modern impetus in light scattering is due both to the refinement in liquid theories and to improvements in experimental techniques. In addition to enhancing the data obtained from traditional experiments, modern light scattering techniques (especially the spectral techniques) should become useful in several new areas, for example: (a) the determination of a liquid's phenomenological coefficients, (b) the elucidation of relaxational processes in liquids (40), especially relative to NMR spectra and reaction kinetics, (c) the determination of activity coefficients (41), (d) the investigation of fast reaction kinetics (42,43), (e) the determination of molecular structure, and (f) possibly more important, the experimental

basis of theoretical studies of the liquid state. Since most biological reactions occur in the liquid state, light scattering will provide fundamental knowledge about the corresponding macromolecules.

#### Purpose of this Research

Motivated by this modern impetus in light scattering, the primary purpose of the research reported on in this thesis is the design, construction, optimization and characterization of a versatile, convenient light scattering spectrophotometer capable of photometric type experiments as well as the acquisition of Brillouin spectra.

Compared to the traditional photometric light scattering experiments, the design requirements on a light scattering spectrometer suitable for Brillouin spectroscopy are much more demanding. Traditional light scattering photometry may be viewed as a subset of Brillouin spectroscopy; therefore, the discussion of this instrumental system will center on Brillouin spectroscopy.

#### Identification of Brillouin Spectra

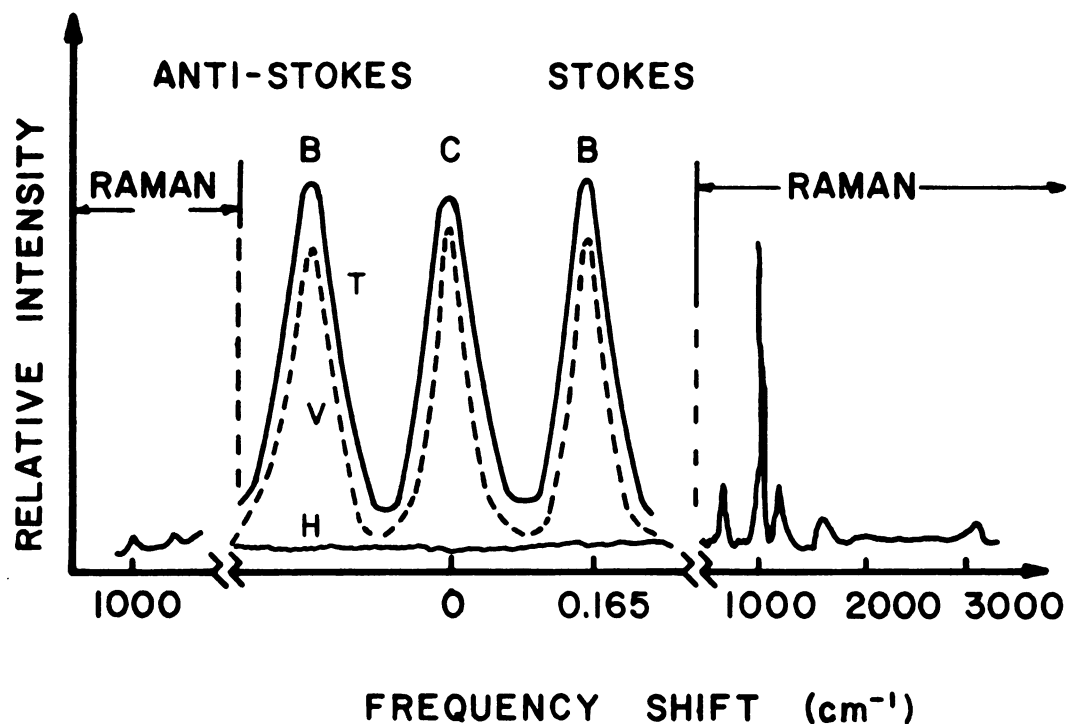
From an experimental point of view, if one passes scattered light through a high resolution spectrometer, he finds that the spectra of the scattered light, in the region of the incident beam's frequency, are typically composed of three peaks. The central peak corresponds to true elastic scattering; the other two inelastic peaks

have equal intensity and are symmetrically shifted from the central line. In his theoretical prediction of these spectra, Brillouin (30) computed the frequency shift of these two peaks from the central peak to be

$$\Delta\nu = \pm 2\nu_0 \left(\frac{v}{c}\right) n \sin(\phi/2) \quad (1-2)$$

wherein:  $\nu_0$  is the frequency of the incident radiation,  $\Delta\nu$  is the frequency separation of the two shifted peaks from  $\nu_0$ ,  $v$  is the velocity of sound in the medium,  $c$  is the velocity of light in a vacuum,  $n$  the refractive index of the media and  $\phi$  is the scattering angle, that is, the angle between the emerging incident light beam and the line of view. These two quasi-elastic peaks are the Stokes and anti-Stokes peaks corresponding to the inelastic collision of an incident photon with a phonon. (Note that this phonon corresponds to a collective state rather than an independent particle.) Figure 1.1 illustrates most of the essential features of a Brillouin spectrum in relation to the corresponding Raman spectrum.

Brillouin scattering may be discussed either in classical electromagnetic language or via quantum mechanics. Classically, we recall, at equilibrium, a liquid is in thermal motion which produces local fluctuations in the density and hence fluctuations in the local dielectric constant and refractive index. These fluctuations are



- C: CENTRAL - RAYLEIGH PEAK
- B: BRILLOUIN - SHIFTED PEAKS
- T: TOTAL SIGNAL
- H: SIGNAL POLARIZED IN THE SCATTERING PLANE
- V: SIGNAL POLARIZED PERPENDICULAR TO THE SCATTERING PLANE

Figure 1.1. Typical Brillouin-Raman Spectrum.

optical inhomogeneities which cause light to be scattered. Some of these fluctuations propagate through the media in a manner similar to sound propagations. Just as compressions and rarefractations arise from a transducer and propagate through air carrying sound, this very same process occurs in liquids. However, contrary to the infinite (or at least very long) wave train so implied above, the "density oscillations" in a liquid transfer their energy into other modes of motion and these "oscillations" are dampened rapidly. The finite lifetime of this "sound wave" explains the line broadening in the frequency shifted peaks. In liquids, the Brillouin peaks are much wider than the central Rayleigh peak.

As a sound wave propagates, a periodic array in density yields a medium with a property corresponding to the grating effect of a crystal. Thus one might envision "light as being diffracted by thermally excited sound waves," and consequently the Bragg diffraction law should apply. However, this "grating" is moving with the speed of sound so that the frequency of the "reflected" light is reduced or increased by a Doppler shift. This explanation is schematically illustrated in Figure 1.2.

From a quantum mechanical viewpoint, we consider the Brillouin peaks to arise from inelastic photon-phonon collisions; this description is outlined in Figure 1.3. Because the ratio of the velocity of sound,  $v$ , to the

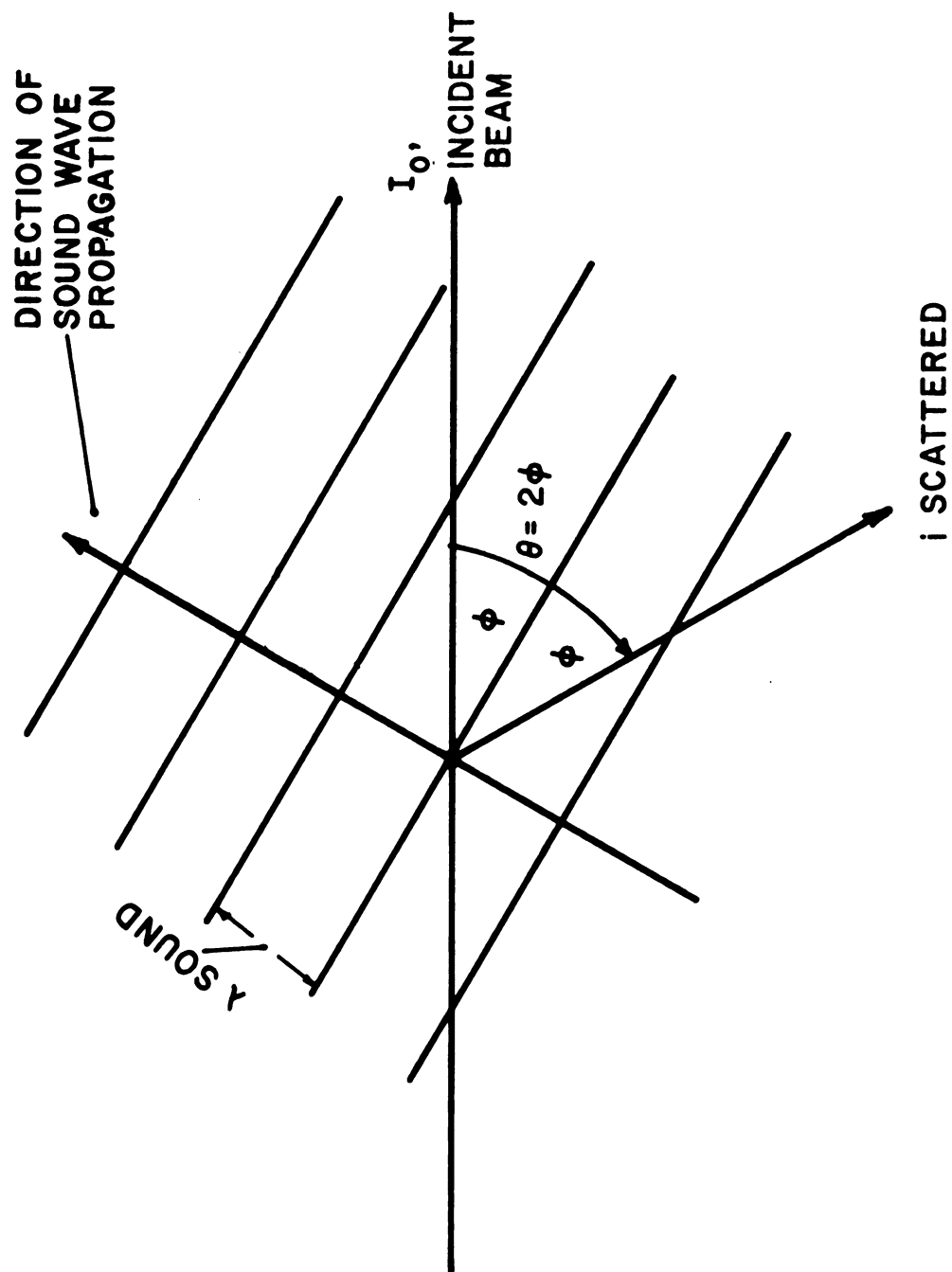
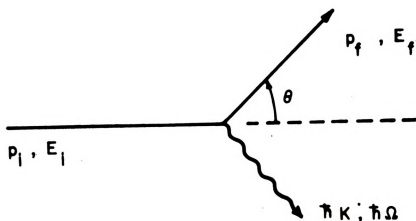


Figure 1.2. Classical Description of Brillouin Spectra.





INELASTIC PHOTON-PHONON COLLISION REQUIRES

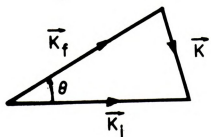
(a) ENERGY CONSERVATION;  $E_f = E_i \pm \hbar \Omega$

(b) MOMENTUM CONSERVATION;  $p_f = p_i \pm \hbar K$

+ : "ANTI-STOKES" OR PHONON ANNIHILATION

- : "STOKES" OR PHONON CREATION

(a)



WHICH, BY GEOMETRY YIELDS:  $|\vec{K}| = 2 |\vec{K}_i| \sin \theta/2$

(b)

Figure 1.3. Quantum Mechanical Description of Brillouin Spectra.

velocity of light,  $c$ , is small, that is  $\bar{K}$  is small, one essentially obtains the same result as he would from the classical description.



## CHAPTER II

### THEORETICAL FORMULISM

#### Electromagnetic Theory of Liquid Light Scattering

Maxwell's equations for the electromagnetic field vectors for a non-conducting, non-magnetic media are:

$$\nabla \times \underline{E} = - \frac{1}{c} \frac{\partial \underline{H}}{\partial t} \quad (2-1)$$

$$\nabla \times \underline{H} = \frac{1}{c} \frac{\partial \underline{D}}{\partial t} + \underline{j} \quad (2-2)$$

$$\nabla \cdot \underline{D} = 0 \quad (2-3)$$

$$\nabla \cdot \underline{B} = 0 \quad (2-4)$$

and the constitutive relationships are:

$$\underline{B} = \underline{H} \quad (2-5)$$

$$\underline{D} = \underline{\epsilon} \underline{E} \quad (2-6)$$

where  $\underline{\epsilon}$  is the dielectric tensor which for an isotropic, non-absorbing, non-optically active media becomes a scalar. (If one wants to avoid these assumptions, the mathematical analysis becomes quite complex. Such an analysis is not needed for this discussion. A more general analysis, not

invoking these simplifying assumptions has been made by Pecora (16), Anselm (13), and others [14,15,17].)

By eliminating  $\underline{H}$  from the first two equations and utilizing the second two as well as the constitutive relationships, an inhomogeneous wave equation for  $\underline{D}$  may be obtained:

$$\nabla^2 \underline{D} - \frac{\epsilon}{c^2} \frac{\partial^2 \underline{D}}{\partial t^2} = \frac{\epsilon}{c} \frac{\partial \underline{j}}{\partial t} \quad (2-7)$$

Following Komarov and Fisher's adaptation of Van Hove's liquid X-ray, neutron scattering theory, if our system is irradiated by a monochromatic plane wave with electric field vector

$$\underline{E}_0(\underline{r}, t) = \underline{E}_0 e^{i(\underline{k}_0 \cdot \underline{r} - \omega_0 t)} \quad (2-8)$$

then a dipole moment density is induced and may be given by

$$\underline{p}(\underline{r}, t) = \alpha \underline{E}_0(\underline{r}, t) \sum_i \delta(\underline{r}_i - \underline{r}) \quad (2-9)$$

wherein  $\alpha$  is an effective polarizability of a single molecule in the total electric field of its neighbors. The summation is over all particles in the liquid, or at least over the finite physical volume element described by these equations. Assuming the polarizability to be frequency independent at optical frequencies, the current associated with the dipole moment density is given by

$$\underline{j} = \frac{1}{c} \frac{\partial \underline{p}}{\partial t} = \frac{\alpha}{c} \frac{\partial [\underline{E}_0(\underline{r}, t) \rho(\underline{r}, t)]}{\partial t} \quad (2-10)$$

wherein

$$\rho(\underline{r}, t) = \sum_i \delta(\underline{r}_i - \underline{r}) \quad (2-11)$$

is the local density of the liquid.

The scattered radiation (electromagnetic field due to this induced, oscillating dipole moment density) is given by the solution of the inhomogeneous wave equation (2-7) with the current source given by this dipole moment, equation (2-10). Solving this equation with a Fourier transform analysis and recalling that what we measure is the field intensity given by

$$I(\underline{R}, \omega) d\omega = |\underline{E}(\underline{R}, \omega)|^2 d\omega \quad (2-12)$$

we obtain the solution:

$$I(\underline{R}, \omega) d\omega = I_0 \left[ \frac{k_i^2 \alpha \sin \phi}{R} \right]^2 \left\{ \int_{-\infty}^{\infty} \frac{dt}{2\pi} \langle \rho(\underline{k}, 0) \rho^*(\underline{k}, t) \rangle e^{-i\omega t} \right\} \quad (2-13)$$

wherein we have introduced the definitions:  $I_0$  and  $k_i$  are the intensity and wave vector of the plane-polarized incident beam (a time averaged intensity),  $R$  is the distance from the scattering volume element to the

observation point,  $\phi$  is the angle between  $\underline{R}$  and the electric field vector of the incident wave,  $\underline{k} \equiv n(\underline{k}_0 - \underline{k}_i)$  is the change in wave vector in the media of refractive index  $n$  and is given by

$$k = |\underline{k}| = 2nk_i \sin (\theta/2) \quad (2-14)$$

for this quasi-elastic scattering at the observation angle  $\theta$ ,  $\rho(\underline{k}, t)$  is the spatial Fourier transform

$$\int d\underline{r}^3 \rho(\underline{r}, t) e^{i\underline{k} \cdot \underline{r}}$$

and  $\langle \rho(\underline{k}, 0) \rho^*(\underline{k}, t) \rangle$ , mathematically equivalent to  $\langle \rho(\underline{k}, 0) \langle \rho^*(\underline{k}, t) \rangle_0 \rangle$ , is the Fourier associated, time dependent density-density correlation function. Many of the mathematical properties and physical interpretations of this double ensemble average are elucidated by Van Hove, Komarov and Fisher. In summary, let it be said that  $\langle \rho^*(\underline{k}, t) \rangle_0$  is a conditional ensemble average. It is the average of the values which  $\rho^*(\underline{k}, t)$  can have at time  $t$  after it had the initial value  $\rho^*(\underline{k}, 0)$ . After obtaining this ensemble average, one calculates the final ensemble average of all the possible weighted products of this with the initial values  $\rho(\underline{k}, 0)$ .

### Linearized Hydrodynamic Liquid Theory

According to the work of Mountain (22-27), Nichols and Carome (28), this conditional ensemble average may be

obtained from an equation of motion originating from a linearized hydrodynamic theory of the liquid. The pertinent equations are (1) the continuity equation:

$$\frac{\partial \rho}{\partial t} + \rho_0 \nabla \cdot \underline{v} = 0 \quad (2-15)$$

(2) the longitudinal part of Navier-Stokes equation modified by the addition of time-dependent viscosity terms (for the justification of this see (27):

$$\begin{aligned} m\rho_0 \frac{\partial \underline{v}}{\partial t} = & -\nabla p_1 + \left(\frac{4}{3}\eta_s + \eta_v\right) \nabla(\nabla \cdot \underline{v}) \\ & + \sum_{j=i}^N \int_{-\infty}^t \eta_j(t-t') \nabla[\nabla \cdot \underline{v}(t')] dt' \end{aligned} \quad (2-16)$$

and (3) the energy transport equation:

$$m\rho_0 T_0 \frac{\partial S}{\partial t} = \kappa \nabla^2 T \quad (2-17)$$

In these equations:

$$\rho = \rho_0 + \rho_1(\underline{r}, t) \quad (2-18)$$

$$T = T_0 + T_1(\underline{r}, t) \quad (2-19)$$

$\rho_0$  and  $T_0$  are space-time number averages,  $\rho_1$ ,  $T_1$  and  $p_1$  are the excess number density, temperature and hydrostatic



pressure respectively,  $S$  is the entropy per unit mass,  $m$  is the molecular mass,  $\kappa$  is the thermal conductivity,  $\eta_s$   $\eta_v$  are the frequency independent shear and volume (intrinsic) viscosities respectively,  $N$  is the number of frequency-dependent viscosity terms  $\eta_j(t)$  and  $\underline{v}(\underline{r}, t)$  is the irrotational part of the local velocity field whose average is zero.

To solve these phenomenological equations, Mountain et al. invoked the Laplace time-frequency transform:

$$\rho(\underline{k}, s) = \int_0^{\infty} e^{-st} \rho(\underline{k}, t) dt \quad (2-20)$$

and obtained the solution:

$$I(\omega) = I_0 \left[ \frac{k_i^2 \alpha \sin \phi}{R} \right]^2 \langle |\rho(\underline{k}, 0)|^2 \rangle \sigma(k, \omega) \quad (2-21)$$

wherein<sup>1</sup>

$$\sigma(k, \omega) = 2 \operatorname{Re} \left[ \frac{F(k, i\omega)}{G(k, i\omega)} \right] \quad (2-22)$$

$$\begin{aligned} F(k, s) = s^2 + s \left( ak^2 + bk^2 + \sum_i \frac{b_i k^2}{(1+s\tau_i)} \right) + abk^4 \\ + \sum_i \frac{ab_i k^4}{(1+s\tau_i)} + \underline{v}_0^2 \frac{k^2 (\gamma-1)}{\gamma} \end{aligned} \quad (2-23)$$

---

<sup>1</sup>Inherent in this derivation is Mountain's (22) conversion of the memory factors of equation (2-16) to a form which utilizes  $\tau_i$ , the time constant associated with  $\eta_i$ .

$$G(k,s) = s^3 + s^2 \left[ ak^2 + bk^2 + \sum_i \frac{b_i k^2}{(1+s\tau_i)} \right] \quad (2-24)$$

$$+ s \left[ v_o^2 k^2 + abk^4 + \sum_i \frac{ab_i k^4}{(1+s\tau_i)} \right] + \frac{av_o^2 k^4}{\gamma}$$

$$a \equiv \kappa/\rho_o C_v \quad (2-25)$$

$$b \equiv \left(\frac{4}{3} \eta_s + \eta_v\right)/m\rho_o \quad (2-26)$$

$$b_i \equiv \eta_i/m\rho_o \quad (2-27)$$

The expression for the structure factor  $\sigma(k,\omega)$  can be converted into a form more convenient for discussing the spectra, namely partial fractions. To do this, one first converts the ratio of the  $F(k,s)$  and  $G(k,s)$  functions into a ratio of polynomials,  $F_N(k,s)$  and  $G_N(k,s)$ , by multiplying both the numerator and denominator by the product of the  $(1+s\tau_i)$  terms. Then one (a) calculates the roots of the dispersion equation,  $G_N(s) = 0$ , (b) constructs a factored form of  $G_N(s)$  and (c) splits  $\sigma(k,\omega)$  into partial fractions using these factors as the denominators. For a liquid with a single relaxation process ( $N=1$ , for example carbon tetrachloride), these equations take on the forms:

$$G_1(s) = \tau_1 (s+\Gamma_B - i\omega_B) (s+\Gamma_B + i\omega_B) (s+\Gamma_{CT}) (s+\Gamma_{CI}) \quad (2-28)$$

$$\sigma(k,\omega) = 2 \left\{ A_{CT} \frac{\Gamma_{CT}}{\Gamma_{CT}^2 + \omega_B^2} + A_{CI} \frac{\Gamma_{CI}}{\Gamma_{CI}^2 + \omega_B^2} \right\} \quad (2-29)$$

$$\begin{aligned}
& + A_{BS} \left[ \frac{\Gamma_B}{\Gamma_B^2 + (\omega + \omega_B)^2} + \frac{\Gamma_B}{\Gamma_B^2 + (\omega - \omega_B)^2} \right] \\
& + A_{BA} \left[ \frac{\omega + \omega_B}{\Gamma_B^2 + (\omega + \omega_B)^2} - \frac{\omega - \omega_B}{\Gamma_B^2 + (\omega - \omega_B)^2} \right] \left. \vphantom{\begin{aligned} & + A_{BS} \left[ \frac{\Gamma_B}{\Gamma_B^2 + (\omega + \omega_B)^2} + \frac{\Gamma_B}{\Gamma_B^2 + (\omega - \omega_B)^2} \right] \\ & + A_{BA} \left[ \frac{\omega + \omega_B}{\Gamma_B^2 + (\omega + \omega_B)^2} - \frac{\omega - \omega_B}{\Gamma_B^2 + (\omega - \omega_B)^2} \right] \end{aligned}} \right\} \quad (2-29-- \\
& \qquad \qquad \qquad \text{cont.})
\end{aligned}$$

The roots of equation (2-24), or Brillouin spectral parameters, (line widths and position) are related to the thermodynamic parameters of the liquid through some rather complex relationships. The purpose of experimental Brillouin spectroscopy is to determine the spectral parameters directly. It is more convenient to compare experimental and theoretical values of the spectral parameters using numerical techniques rather than analytical expressions to calculate the roots of equation (2-24). Approximate expressions for these roots are available in the literature (22,23,26,28).

Since Brillouin spectroscopy deals only with  $\sigma(k, \omega)$ , we can ignore absolute intensity measurements and fix the coordinate scale factor by requiring  $\sigma(k, \omega)$  to integrate to unity. The other factors in the  $I(\omega)$  expression are related to classical light scattering experiments and are discussed extensively elsewhere.

### Fabry-Perot Interferometry

To study the fine structure of a Brillouin spectrum, one needs a device of very high resolving power. Optical homo- or heterodyne techniques are of extremely high



resolving power but have a very limited spectral range; double grating and many interferometric techniques would easily scan the entire spectral range but have an insufficient resolving power and present many other problems from a practical point of view. Fabry-Perot interferometry compromises these two extremes and presents the best method for resolving Brillouin spectra.

The applications of Fabry-Perot interferometers have become extremely varied; these interferometers are used for spectral resolution (dispersion) and as tuned resonant circuits for optical generators, namely, cavities for lasers. The Fabry-Perot interferometers (first described by Fabry and Perot in 1897) originally consisted of a pair of plane-parallel mirrors. Later, Connes extended the concepts and technology to a pair of spherical mirrors. For laser cavities spherical mirrors are used primarily because it is easier to obtain higher finesse (resolving power) with them than with the plane-parallel mirrors from an experimental point of view. However, the spherical mirrors are not as versatile as the plane-parallel mirrors for Brillouin spectral analysis because their free spectral range is fixed.

The theory (and application) of Fabry-Perot interferometry has been discussed in the literature extensively (44-59). However, in order to conveniently explain the light scattering instrument later, the essential features will be presented here.

The physical phenomenon responsible for Fabry-Perot interferometry is the constructive or destructive recombination of a multiple reflected beam. This is illustrated in Figure 2.1(a). The transmission of this multiple-beam interferometer is usually given by the analytical expression (an Airy function):

$$\tau(\theta, \lambda) \equiv \frac{I_t(\theta, \lambda)}{I_o(\theta, \lambda)} = \left( \frac{T}{1-R} \right)^2 \frac{1}{1 + \frac{4R}{(1-R)^2} \sin^2 \delta/2} \quad (2-30)$$

or

$$\tau(\theta, \lambda) = \left( \frac{TF}{\pi} \right)^2 \frac{1}{1 + \left( \frac{2F}{\pi} \sin \delta/2 \right)^2} \quad (2-31)$$

wherein:

$$F \equiv \text{finesse} = \frac{\pi \sqrt{R}}{(1-R)} \approx \frac{\pi}{(1-R)} \quad \text{for } R \rightarrow 1.0$$

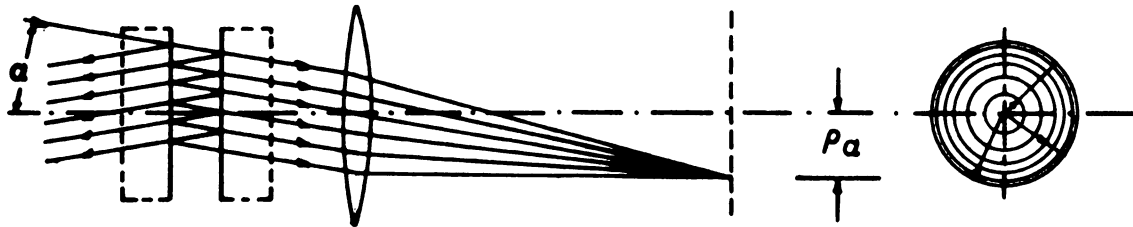
$$\delta \equiv \text{scanning parameter} = \frac{4\pi}{\lambda} d \cos \theta$$

$d \equiv$  optical path separation of mirrors  $= nl$

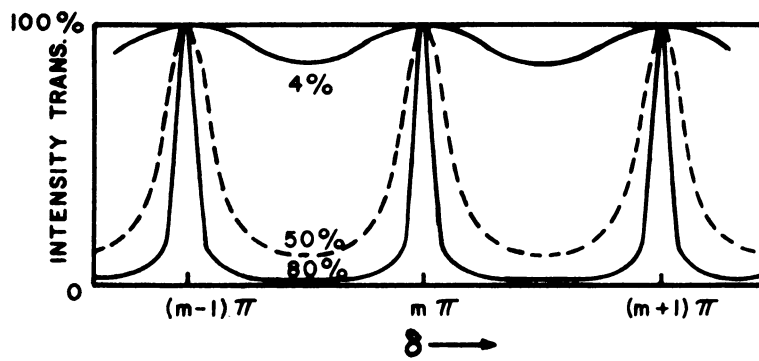
$n \equiv$  refractive index of media between reflecting surfaces

$l \equiv$  physical separation of mirrors

$R = \sqrt{R_1 R_2} \equiv$  the geometric mean reflectivity of the two mirrors



(a)



(b)

Figure 2.1. Fabry-Perot Interferometry.

$T = \sqrt{T_1 T_2} \equiv$  the geometric mean transmission of the two mirrors

$\theta \equiv$  angle of incidence

In the derivation of this expression it was assumed that the mirrors were perfectly flat, perfectly parallel to one another, extended infinitely- perpendicular to their axis and do not absorb or scatter light. These assumptions are difficult to realize in practice. The imperfect nature of a practical instrument is conveniently dealt with by re-defining the finesse as:

$$\frac{1}{F} = \sum_i \frac{1}{F_i} \quad (2-32)$$

Each  $F_i$  is associated with one of the finesse degrading factors and is given by:

Reflectivity limited finesse,  $F_R = \frac{\pi\sqrt{R}}{(1-R)} \quad (2-33)$

Mirror-figure-of-merit limited finesse,

$$F_f = \frac{\lambda}{2\Delta} \quad (2-34)$$

Mirror-tilt limited finesse,  $F_\phi = \frac{\lambda}{2d\phi} \quad (2-35)$

Aperture diffraction limited finesse,

$$F_D = \frac{D^2}{2\lambda d} \quad (2-36)$$

(for normally incident beam)



and

Beam attenuation limited finesse,

$$F_L \approx \frac{\pi}{L} \quad (2-37)$$

wherein:

$L \equiv$  (small) loss due to absorption and scattering in  
a single transit of the interferometer

$D \equiv$  effective aperture diameter (at mirrors)

$\lambda \equiv$  mean wavelength

$\phi \equiv$  mirror tilt angle in radians

$\Delta \equiv$  RMS mirror surface deformation

$F_f \leq m/2$  if the mirrors are flat to  $\lambda/m$

Historically, the Fabry-Perot spectra were recorded photographically; the various rings, illustrated in Figure 2.1(a), were photographed and the photograph was scanned with a densitometer across a diameter to obtain the spectra illustrated in Figure 2.1(b). However, in modern interferometry, a pinhole and photomultiplier tube replace the photographic plate and the spectra are scanned by varying one of the variables (especially  $n$  or  $l$  but sometimes  $\theta$ ) in the scanning parameter  $\delta$  above. Our interferometer varies  $l$  by applying a voltage to a piezoelectric transducer which supports one of the mirrors.

Instrumental parameters related to the spectra are:  
The spectral separation of two adjacent transmission maxima

is termed the free spectral range and determines the maximum frequency span which a spectrum may have (in other words, the maximum spectral range which can be observed) without overlap from adjacent transmission modes. The width (full width at half of maximum) of each of these transmission maxima, the apparent bandwidth observed for a perfectly monochromatic incident beam, is termed the instrumental bandwidth. It determines the minimum resolvable spectral increment. The ratio of the free spectral range to the bandwidth is equal to the experimental finesse. The acceptance angle is the maximum full-cone angle over which the incident beam may be collected without degradation of a specified finesse; it is given by

$$\Delta\theta \leq 2\left(\frac{\lambda}{Fd}\right)^{1/2} \quad (2-38)$$

Expressions for these instrumental parameters and their dimensional units are summarized in Table 2.1.

The effective parallelism and flatness of the mirrors may be greatly improved by selecting a high quality portion of the mirror's total aperture. However, in addition to reducing the beam intensity (hence, subsequent electronic signal to noise ratio), reducing the interferometer's aperture degrades the interferometer's effective finesse through walk-off and diffraction effects. An aperture diameter which maximizes the net finesse, the best

TABLE 2.1.--Instrumental Parameters for Fabry-Perot Interferometer.

	Wavenumber	Wavelength	Frequency
Free spectral range	$\Delta\sigma^* = \frac{1}{2d}$	$\Delta\lambda^* = \frac{\lambda^2}{2d}$	$\Delta\nu^* = \frac{c}{2d}$
Bandwidth	$\delta\sigma$	$\delta\lambda$	$\delta\nu$
Finesse, F	$F = \frac{\Delta\sigma^*}{\delta\sigma}$	$F = \frac{\Delta\lambda^*}{\delta\lambda}$	$F = \frac{\Delta\nu^*}{\delta\nu}$

compromise between misalignment and diffraction or walk-off effects, is given by the expression:

$$D_{\text{opt}} = \left( \frac{\lambda^2 d}{\phi} \right)^{1/3} \quad (2-39)$$

when the mirrors are tilted at  $\phi$  to each other.

When a photoelectric method is used to record spectra, a lens, focal length  $f_L$ , focuses the beam onto a plane which contains a pinhole. The radii of the Fabry-Perot rings associated with different angles of incidence,  $\alpha$ , of a monochromatic beam are given by

$$\rho_\alpha = f_L \tan \alpha \quad (2-40)$$

From this expression, we see that if the radius of the pinhole is too large, the instrument's finesse is obviously destroyed. However, the pinhole radius may



be increased to a point corresponding to the acceptance angle without degrading the instrument's linewidth. The pinhole may be made conveniently large (approximately 2 mm dia., assuming an acceptance angle of 1 milliradian and a focal length lens of 100 cm) by using long focal length collection lenses.

Alignment and calibration will be explained later, in the chapter on the alignment of the entire instrumental system. Also, the inherent compromise between the interferometer's free spectral range and bandpass, as well as serious stability problems will be discussed.

#### Polarization Coherency Matrix

With the invention of the laser, as well as many other improvements in modern optical technology, the matrix representations of optics are becoming more prevalent and provide great utility. The Jones calculus is especially useful to discuss the statistical properties of a propagating electromagnetic field and the action of optical devices on the beam relative to intensity, polarization and coherence.

This formulism is extensively elucidated in the modern optics literature (44,60-63) and will not be given detailed consideration. However, for the reader's convenience, the definitions, methods, etc. used in this work will be summarized.

With the more classical vector representation of the monochromatic electromagnetic field,



$$\underline{E} = \begin{bmatrix} E_x \\ E_y \end{bmatrix} \quad (2-41)$$

many physical properties of some propagating beams, for example an unpolarized (natural) or partially coherent beam, are difficult to discuss. To ease this difficulty we mathematically formulate the polarization coherency matrix (PCM) representation of the radiation field; namely

$$\underline{J} = \langle \underline{E} \underline{E}^\dagger \rangle = \begin{bmatrix} \langle E_x E_x^* \rangle & \langle E_x E_y^* \rangle \\ \langle E_y E_x^* \rangle & \langle E_y E_y^* \rangle \end{bmatrix} = \begin{bmatrix} J_{xx} & J_{xy} \\ J_{yx} & J_{yy} \end{bmatrix} \quad (2-42)$$

wherein,  $\underline{E}^\dagger$  is the Hermitian conjugate of  $\underline{E}$  and the brackets  $\langle \cdot \cdot \rangle$  imply a time average. If we represent an instrument by the operator  $\underline{L}$ , then the incoming  $\underline{E}$  and outgoing  $\underline{E}'$  fields are related by matrix multiplication:

$$\underline{E}' = \underline{L} \underline{E} \quad (2-43)$$

or, in terms of the PCM representation:

$$\underline{J}' = \underline{L} \underline{J} \underline{L}^\dagger \quad (2-44)$$

The PCM representation of some of the common (quasi-monochromatic) radiation fields and optical instruments are tabulated in (60).

The total intensity of a field is given by:

$$I = \text{Tr } \underline{J} = J_{xx} + J_{yy} \quad (2-45)$$

The degree of polarization,  $P$ , is defined as the ratio of the intensity of the polarized part of the field to the total intensity of the field; namely

$$P = \frac{I_{\text{pol}}}{I_{\text{tot}}} \quad (2-46)$$

and its definition in terms of the coherency matrix is:

$$P = \sqrt{1 - \frac{4 \det \mathbf{J}}{(\text{Tr } \mathbf{J})^2}} \quad (2-47)$$

The depolarization ratio is:

$$\rho = \frac{I_{\text{hor}}}{I_{\text{vert}}} = \frac{J_{yy}}{J_{xx}} \quad (2-48)$$

The normalized cross-correlation function  $\mu_{xy}$  is defined by

$$\mu_{xy} = \frac{J_{xy}}{\sqrt{J_{xx}} \sqrt{J_{yy}}} \quad (2-49)$$

and gives the state of wave polarization.

The utility of the PCM evolves from its measurability. There are several sequences of measurements which will yield the PCM elements. The choice here was arbitrary; a rather extensive discussion of the chosen technique may be found in Born and Wolf (44). Basically,





this consists of placement of a retarder and polarizer into the beam and the measurement of the intensity for various orientations of them. If the retarder introduces a phase delay,  $\epsilon$ , of the y component relative to the x component and the polarizer is at an angle  $\theta$  with respect to the x axis, then it may be shown that the transmitted intensity is given by:

$$I(\theta, \epsilon) = J_{xx} \cos^2 \theta + J_{yy} \sin^2 \theta + J_{xy} e^{-i\epsilon} \cos \theta \sin \theta + J_{yx} e^{i\epsilon} \cos \theta \sin \theta \quad (2-50)$$

In particular

$$J_{xx} = I(0, 0) \quad (2-51)$$

$$J_{yy} = I(\pi/2, 0) \quad (2-52)$$

$$J_{xy} = \frac{1}{2} \left\{ I\left(\frac{\pi}{4}, 0\right) - I\left(\frac{3\pi}{4}, 0\right) \right\} + \frac{i}{2} \left\{ I\left(\frac{\pi}{4}, \frac{\pi}{2}\right) - I\left(\frac{3\pi}{4}, \frac{\pi}{2}\right) \right\} \quad (2-53)$$

$$J_{yx} = \frac{1}{2} \left\{ I\left(\frac{\pi}{4}, 0\right) - I\left(\frac{3\pi}{4}, 0\right) \right\} - \frac{i}{2} \left\{ I\left(\frac{\pi}{4}, \frac{\pi}{2}\right) - I\left(\frac{3\pi}{4}, \frac{\pi}{2}\right) \right\} \quad (2-54)$$

if the different values of  $\theta$  correspond to different rotations of the polarizer but the two values for  $\epsilon$ , and 0 and  $\pi/2$ , correspond to a quarter wave plate being in or out of the beam, respectively.



### Convolution and Deconvolution

Since the frequency distribution of the incident radiation and the transmission of the interferometer are not delta functions, the experimental spectrum is a broadened version of the true spectrum of scattered light. The experimental spectrum  $I_e$  is related to the true spectrum  $I_t$  by the convolution relationship

$$I_e(\omega) = \int_{-\infty}^{\infty} f(\omega - \omega') I_t(\omega') d\omega' \quad (2-55)$$

wherein  $f(\omega - \omega')$  is the normalized instrumental profile which may be measured by directing a divergent laser beam into the detection optics or approximated very well by the central peak of a pure liquid.  $\omega$  is the experimental frequency and  $\omega'$  is a dummy integration variable.

However, a scanning interferometer has several transmission modes spaced at a free spectral range ( $\Delta f$ ) apart. Thus, the observed spectra ( $I_{obs}$ ) is really the overlap of several of the spectrum  $I_e$ , namely:

$$I_{obs}(\omega) = \sum_{n=-\infty}^{\infty} I_e(\omega + n 2\pi\Delta f) \quad (2-56)$$

or

$$I_{obs}(\omega) = \sum_{n=-\infty}^{\infty} \int_{-\infty}^{\infty} f(\omega + n2\pi\Delta f - \omega') I_e(\omega') d\omega' \quad (2-57)$$



Now, we recognize this as the sum of convolution integrals and apply the convolution theorem from Fourier analysis to obtain

$$F[I_{\text{obs}}(\omega)] = \sum_{n=-\infty}^{\infty} F[f(\omega + n2\pi\Delta f)] F[I_e(\omega)] \quad (2-58)$$

Factoring out the "constant" factor  $F[I_e(\omega)]$ , recalling the shift theorem from Fourier analysis, that is

$$F[f(\omega + n2\pi\Delta f)] = F[f(\omega)] e^{-in2\pi\Delta f\zeta} \quad (2-59)$$

and then regarding  $F[f(\omega)]$  as "constant" factor, we obtain

$$F[I_{\text{obs}}(\omega)] = F[I_e(\omega)] F[f(\omega)] \sum_{n=-\infty}^{\infty} e^{-in2\pi\Delta f\zeta} \quad (2-60)$$

or

$$F[I_{\text{obs}}(\omega)] = F[I_e(\omega)] F[f(\omega)] \left[ 1 + 2 \sum_{n=1}^{\infty} \cos(n2\pi\Delta f\zeta) \right] \quad (2-61)$$

From this expression, if we measure  $I_{\text{obs}}(\omega)$  and  $f(\omega)$ , we may calculate (deconvolute) the true spectrum:

$$I(\omega) = F^{-1} \left\{ \frac{F[I_{\text{obs}}(\omega)]}{F[f(\omega)] \left[ 1 + 2 \sum_{n=1}^{\infty} \cos(2\pi\Delta f\zeta) \right]} \right\} \quad (2-62)$$

If the free spectral range and finesse of the interferometer are large enough, only the adjacent

interferometer modes contribute significantly to the measured spectrum and the above relation becomes:

$$I(\omega) = F^{-1} \left\{ \frac{F[I_{\text{obs}}(\omega)]}{F[f(\omega)][1+2 \cos(2\pi\Delta f\zeta)]} \right\} \quad (2-63)$$

Utilizing the numerical technique of Singleton (65), Cooley and Tukey, namely the fast Fourier transform (FFT), we may numerically evaluate these Fourier transforms (and inverse transform) easily and rapidly on a computer. We only need the data sets (experimental spectra and instrumental profile); we do not need to make any assumption relative to the analytical form of the instrumental profile or the observed spectrum. Furthermore, if the central point of either data set is really off center by  $\omega_e$  or  $\omega_i$ , and if  $I_{\text{obs}}(\omega)$  and  $f(\omega)$  have the Fourier transforms  $F_e$  and  $F_i$  respectively, then, using the shift theorem:

$$R \equiv \frac{F[I_{\text{obs}}(\omega)]}{F[f(\omega)]} = \frac{e^{i\omega_e\zeta} F_e}{e^{i\omega_i\zeta} F_i} = \frac{F_e}{F_i} e^{i(\omega_e - \omega_i)\zeta} \quad (2-64)$$

Then, multiplying by the complex conjugate:

$$RR^* = \frac{F_e F_e^*}{F_i F_i^*} \quad (2-65)$$





or

$$|R| = \frac{|F_e|}{|F_i|} \quad (2-66)$$

Thus, we see that a data set need not be centered with extreme accuracy. The Fourier transforms of off center data sets will be complex but if one takes the real part of this complex quantity, the data sets are inherently centered without knowing  $\omega_e$  and  $\omega_i$ .

## CHAPTER III

### DATA ANALYSIS TECHNIQUES

#### Introduction

In order to study Brillouin spectroscopy conveniently, it was found useful to have available three computer programs: (1) a program for the simulation of Brillouin spectra assuming various models; (2) a program to eliminate instrumental effects from an experimental curve and generate the true spectrum; (3) a program for the deduction or estimation of spectral parameters from an experimental data set after it was corrected for instrumental effects. The first and last of these programs will be discussed in following sections. Several programs were written for the purpose of eliminating particular experimental effects but since data collection procedures were not standardized, no single correction program was adopted. Experimental corrections include curve smoothing, baseline correction, frequency scaling, intensity scaling, shift to a more convenient data point spacing, deconvolution of the instrumental profile from the experimental curve, and elimination of the contributions from adjacent interferometer modes. These last two effects must be considered in the quantitative discussion of any spectrum.

### Spectra Deconvolution

The mathematical procedure to deconvolute the instrumental profile and eliminate the effects of adjacent interferometer modes is indicated in equation (2-63):

(1) calculate the Fourier transform of the observed experimental spectrum, (2) calculate the Fourier transform of the instrumental profile, (3) divide this latter function into the first function, (4) divide by a trigonometric factor to eliminate adjacent interferometer mode effects (One now has the Fourier transform of the true spectrum.), and (5) take the inverse transform in order to obtain the true spectrum. Inverse Fourier transformation is equivalent to calculating a Fourier transform; thus, the important aspect of this deconvolution procedure is the numerical evaluation of a Fourier transform. These numerical techniques are discussed in the literature (64-69). The numerical technique adapted in the subroutine FFTS<sup>1</sup> is based on the Cooley-Tukey algorithm (65) for computing finite Fourier transforms. This technique is commonly referred to as fast Fourier transform. The calculation of a finite Fourier transform is advantageous over the calculation of a normal Fourier transform in that it involves numerical integration over a finite interval instead of an infinite interval. However, in order for this finite Fourier transform to be appropriate, the original function must

---

<sup>1</sup>Fortran listings of the computer programs and subroutines described in this work are available from the laboratory.



be aliased. Aliasing is the objective of the subroutine ALIAS. The theory and details of this technique are discussed by Cooley (64); briefly, aliasing involves the transformation of a general function into a periodic function. FFTS integrates over the aliased function's period. The details of applying ALIAS and FFTS depend upon the data collection techniques. Since these techniques have not yet been standardized, it is not conveniently possible to discuss in detail the application of these subroutines.

In order to check the FFTS subroutine it was applied twice to several functions (gaussian, lorentzian, voigt and linear combinations of these), and the result compared to the original function. The differences, representing errors in the calculations, were small enough in magnitude to be associated with the number of significant digits carried internally by the computer.

#### Brillouin Spectra Simulation

A computer program designated as BRILSPEC was written to simulate a Brillouin spectrum assuming a particular model and a corresponding set of parameters. In addition to the single relaxation model represented by equation (2-29), a double relaxation and a trilorentzian model were incorporated as options in BRILSPEC. A double relaxation model is also defined in the chapter on theoretical basis of Brillouin spectra ( $N=2$ ); the trilorentzian



model is not. The trilorentzian model assumes that the Brillouin spectrum is composed of three partially overlapping lorentzian peaks, one central lorentzian peak and two additional lorentzian peaks shifted symmetrically from this central peak.

The utilization of BRILSPEC first requires the choice of a model and its characteristic parameters. The data input cards related to the possible models are illustrated in Tables 3.1, 3.2 and 3.3. For different models, only the third (and following) data card varies considerably. This card is formatted as 4F20.5 and the sequence of parameters is: amplitude, halfwidths, and shifts from central peak. By amplitude, we do not mean peak height; these amplitudes correspond to A in the following equation for a lorentzian peak:

$$\frac{A}{B^2 + \chi^2}$$

Table 3.3 is for a single relaxation model; the assumption of other models corresponds to the insertion or omission of corresponding  $A_i$  and  $B_i$  values in the sequence indicated in Table 3.3. If one chooses to have the computer plot data, some additional data input cards are required by the subroutine GRAPH. An explanation of these data cards, and this subroutine, may be found in the instruction manual, "Subroutine Graph", by D. L. Knirk (70).

TABLE 3.1.--First Data Card for BRILSPEC.

Parameter	Column	Format	Code	Definition and Comments
JPTYP	5	I5	1	assumption of trilorenzian model
			2	assumption of single relaxation model
			3	assumption of double relaxation model
			blank	exit, no more work

TABLE 3.2.--Second Data Card for BRILSPEC.

Parameter	Column	Format	Code	Definition and Comments
NP	1-5	I5		number of data points from center out
DW	6-20	F15.5		width of each data interval
NKEY	25	I5	0	calculate only half of spectra
			1	calculate entire spectra
NPLT	30	I5	0	no curves
			1	output curves





TABLE 3.3.--Parameter Data Cards for BRISPEC.

Parameter	Column	Format	Definitions and Comments
A1	1-20	F20.5	amplitude of left peak
A2	21-40	"	amplitude of "primary" central peak
A3	41-60	"	amplitude of right peak
A4	61-80	"	amplitude of "secondary" central peak
B1	41-60	"	half width of left peak
B2	61-80	"	half width of "primary" central peak
B3	1-20	"	half width of right peak
B4	21-40	"	half width of "secondary" central peak
WL	41-60	"	shift of left peak
WR	61-80	"	shift of right peak
AL	1-20	"	amplitude of asymmetric component of left peak
AR	21-40	"	amplitude of asymmetric component of right peak



Figures 3.1, 3.2 and 3.3 indicate the use of this computer program in a qualitative sense. The different figures correspond to different choices of the parameters for the trilorentzian model. These calculations were initially undertaken to illustrate the relative effects of relative peak heights, line width and line shifts on the overlap of the side peaks with the central peak. However, the most important application of this computer program is its conversion to a subroutine and subsequent incorporation into a computer program for the estimation of model parameters from an experimental curve.

#### Brillouin Spectra Parameter Estimation

A Brillouin spectrum may be characterized by a set of parameters; the purpose of the computer program BSPEP is to deduce a set of "best estimates" for these model parameters from an experimental spectrum. Furthermore, by comparing the results obtained for a few different models, one may ascertain which model best describes the data. Figures 3.4 and 3.5 represent the initial and final states when a single relaxation model was assumed to describe the data. Figures 3.6 and 3.7 represent the initial and final states for the same data except a trilorentzian model was assumed. One may easily conclude that the single relaxation model describes the data better than the trilorentzian model.



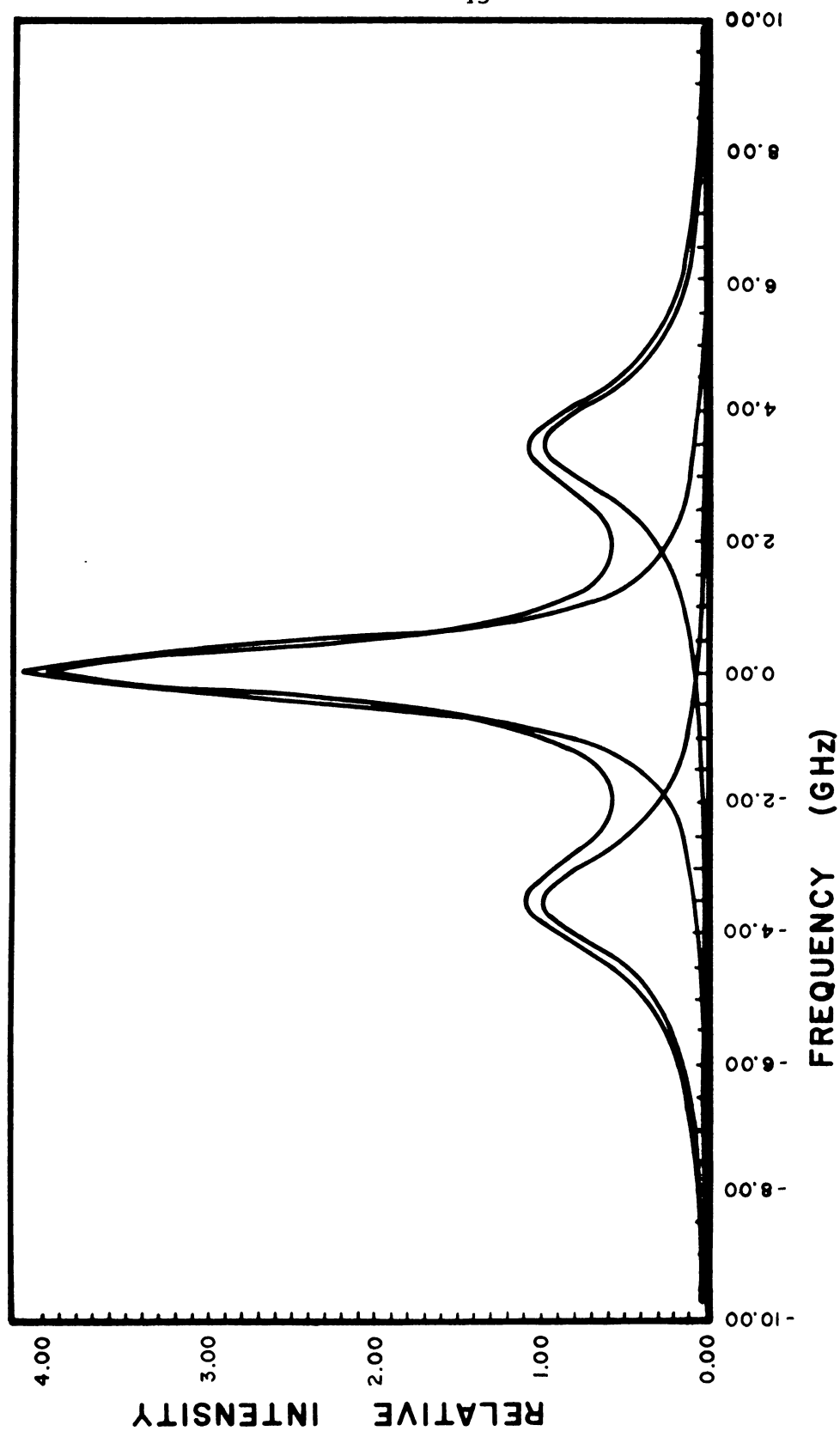


Figure 3.1. Trilorentzian Model with Parameter Set A.



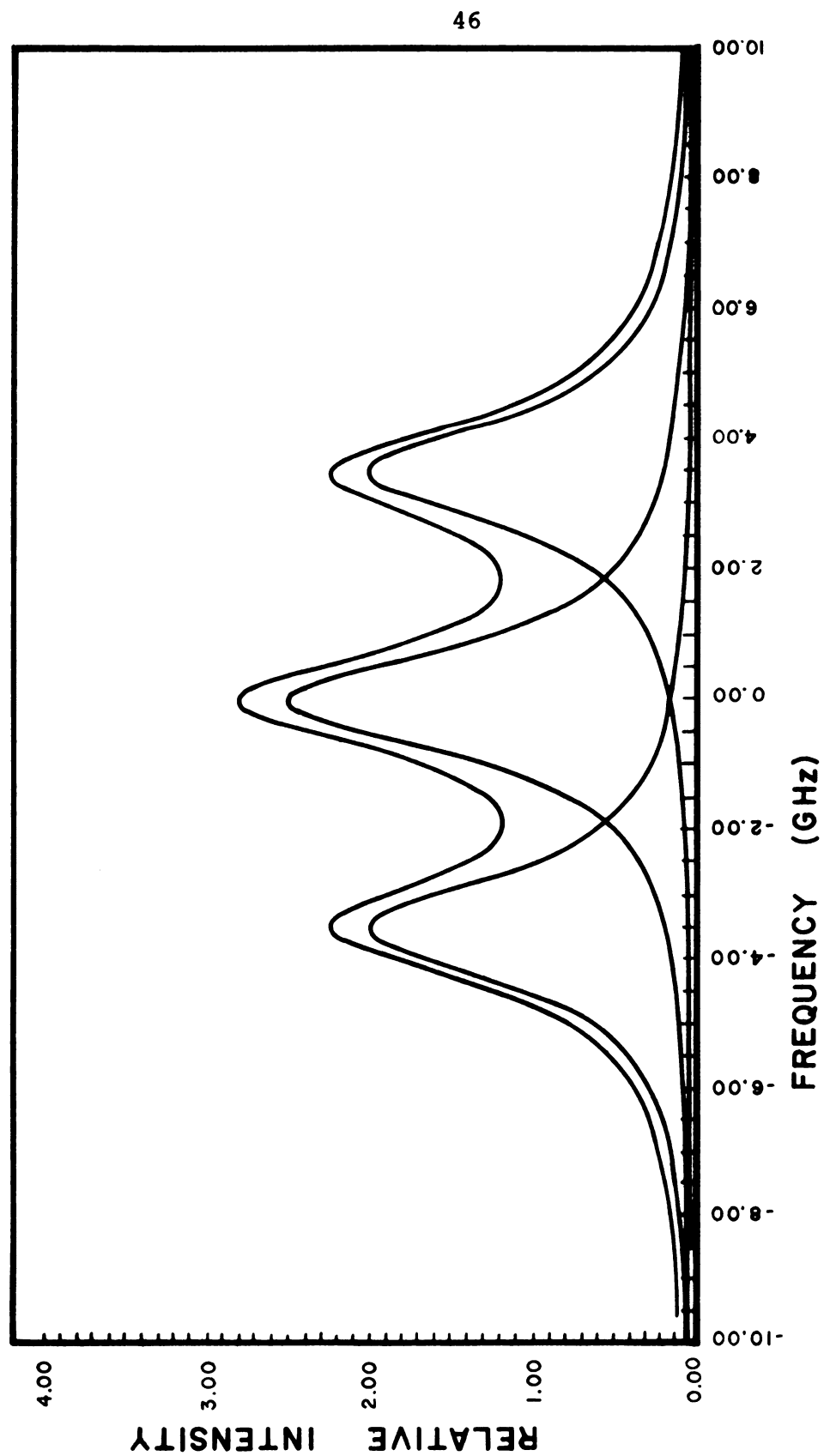


Figure 3.2. Trilorentzian Model with Parameter Set B.





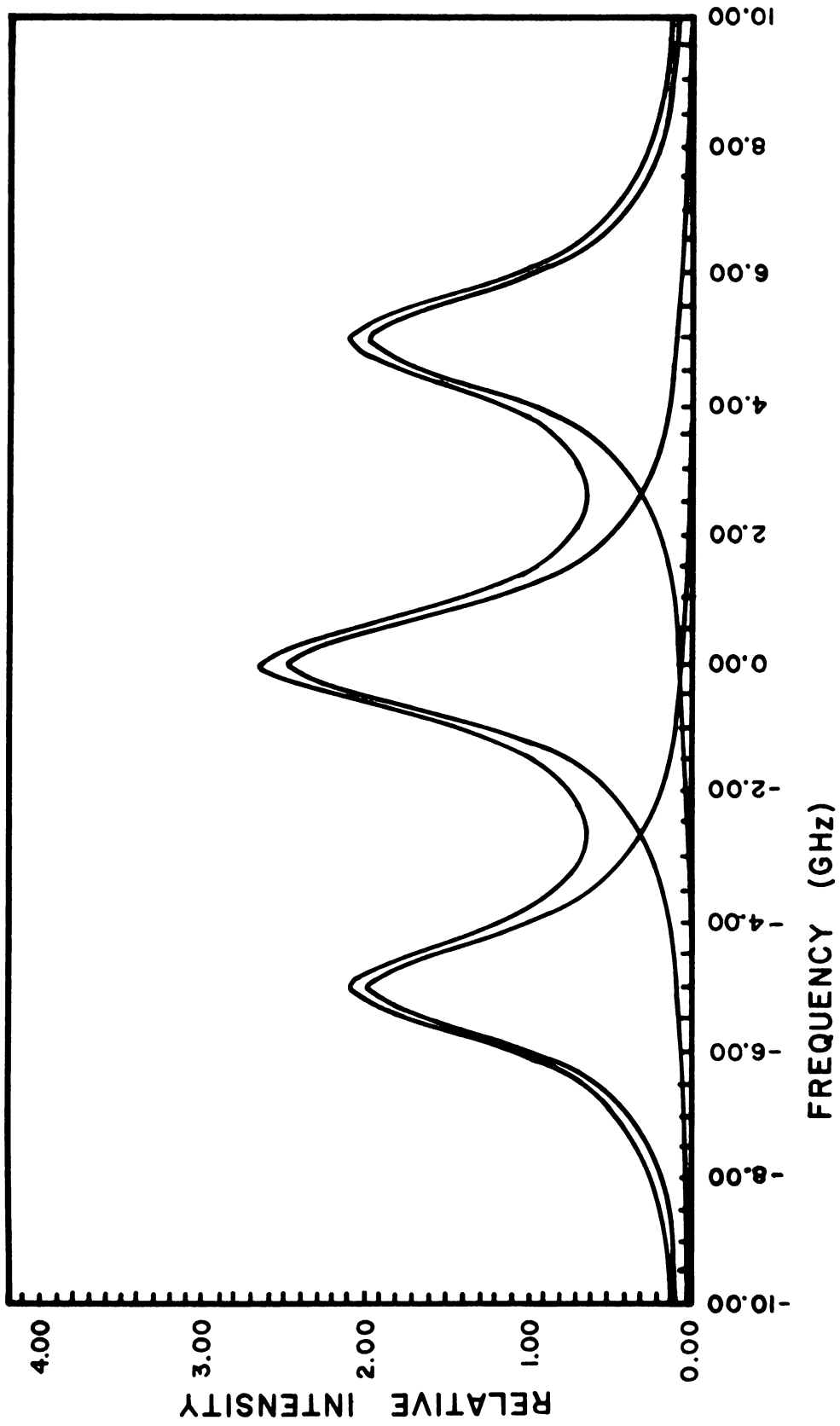


Figure 3.3. Trilorentzian Model with Parameter Set C.



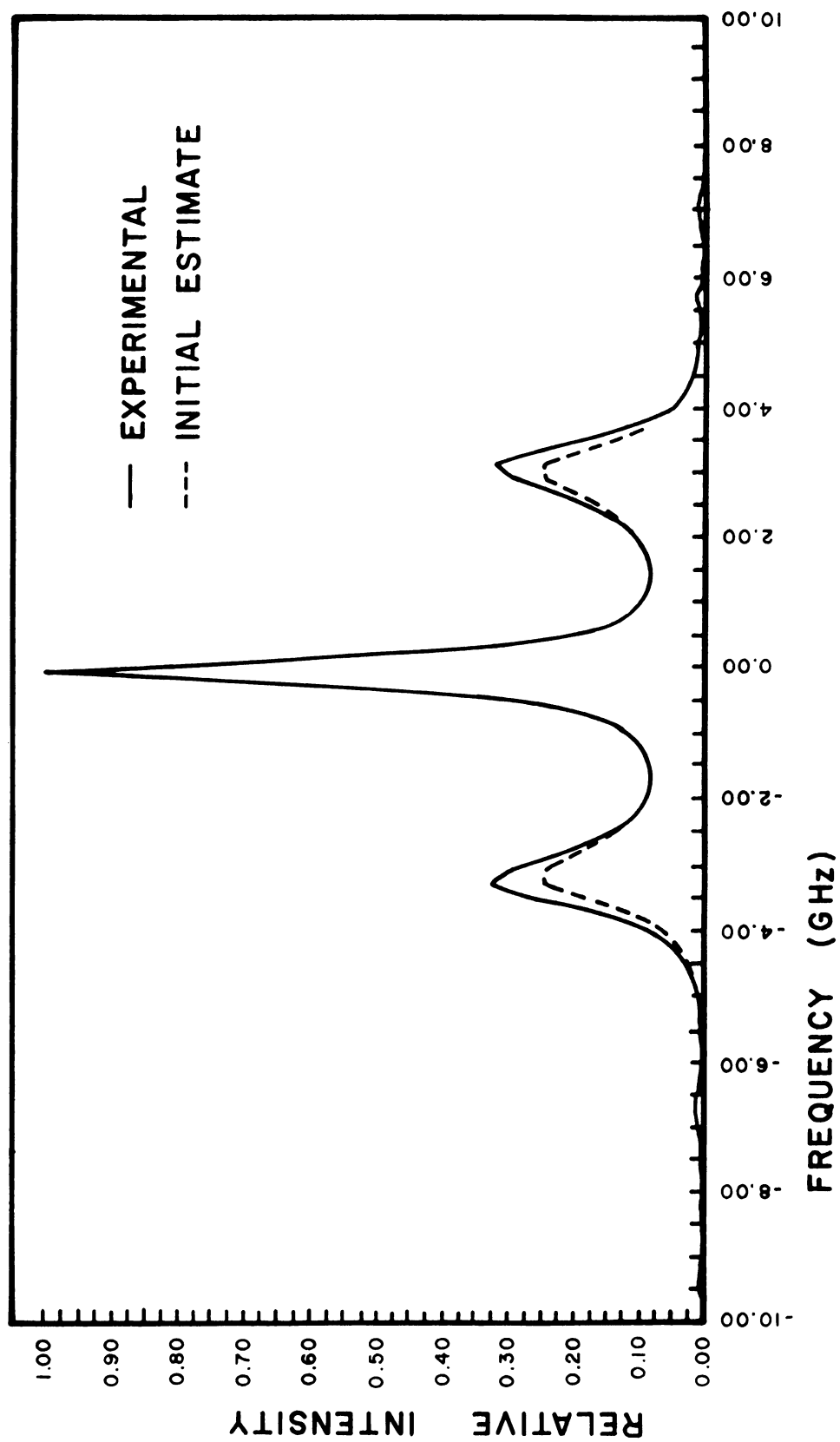


Figure 3.4. Initial Curve Fit for Single Relaxation Model.

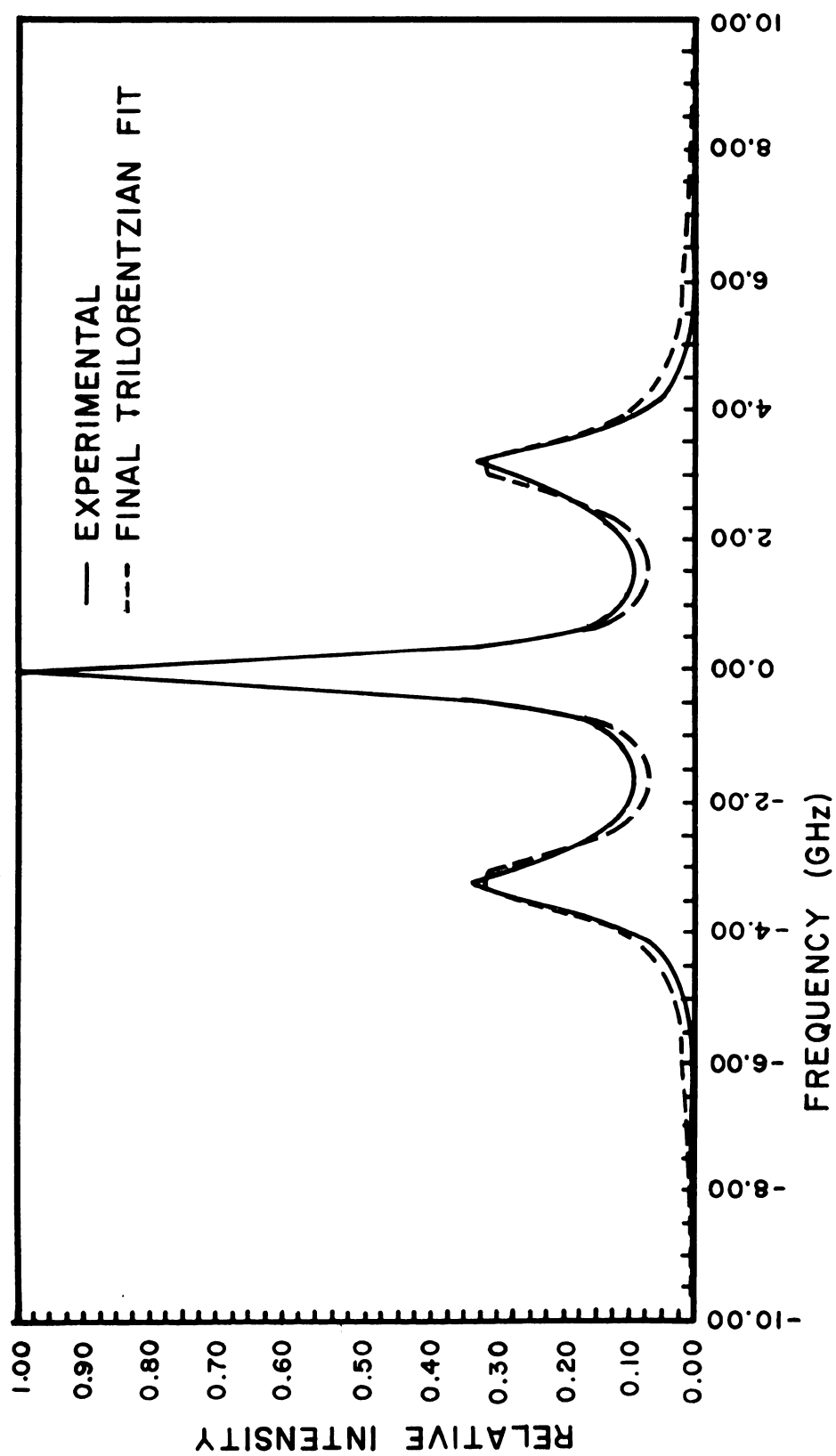


Figure 3.5. Final Curve Fit for Single Relaxation Model.



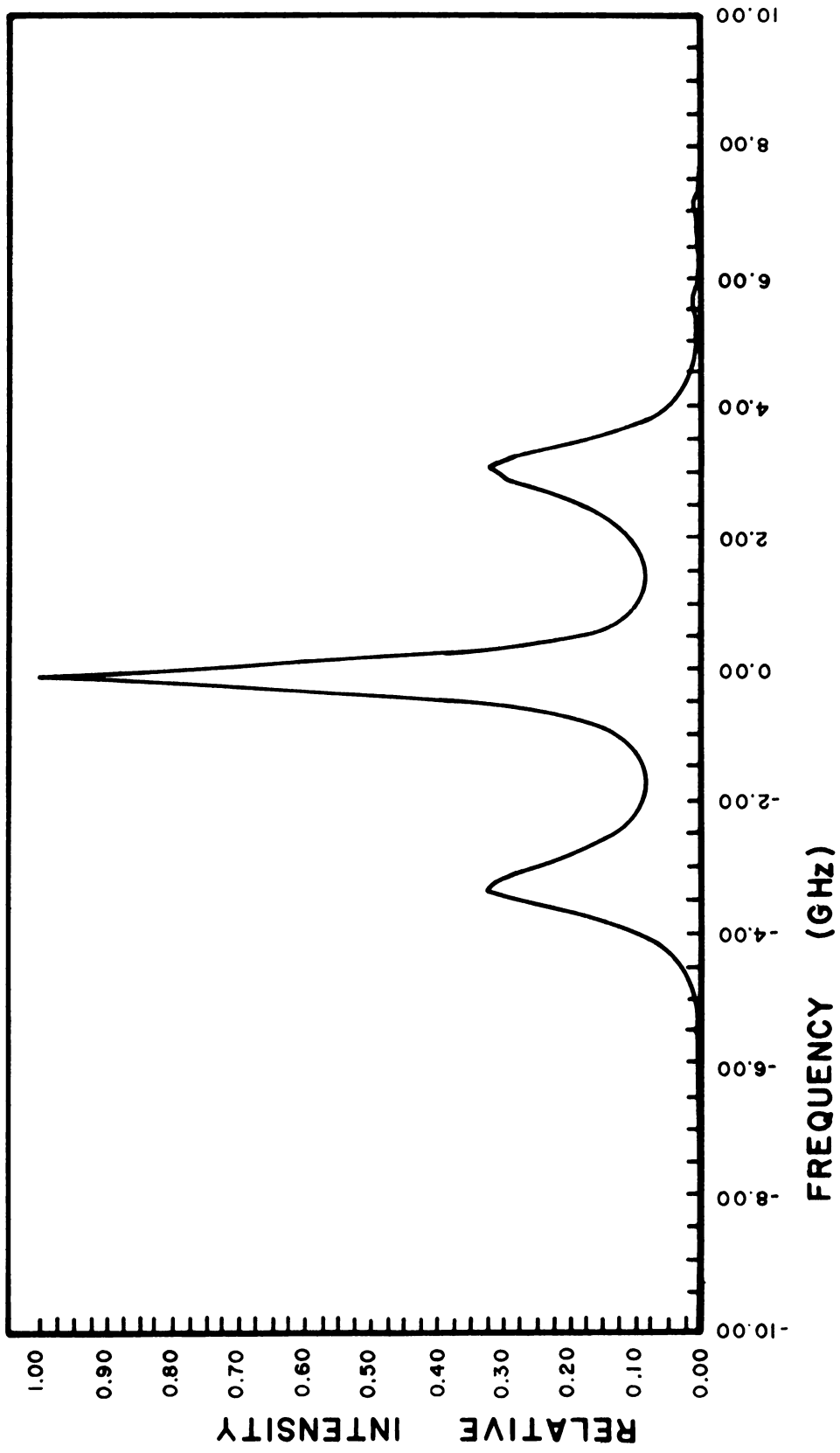


Figure 3.6. Initial Curve Fit for Trilorentzian Model.





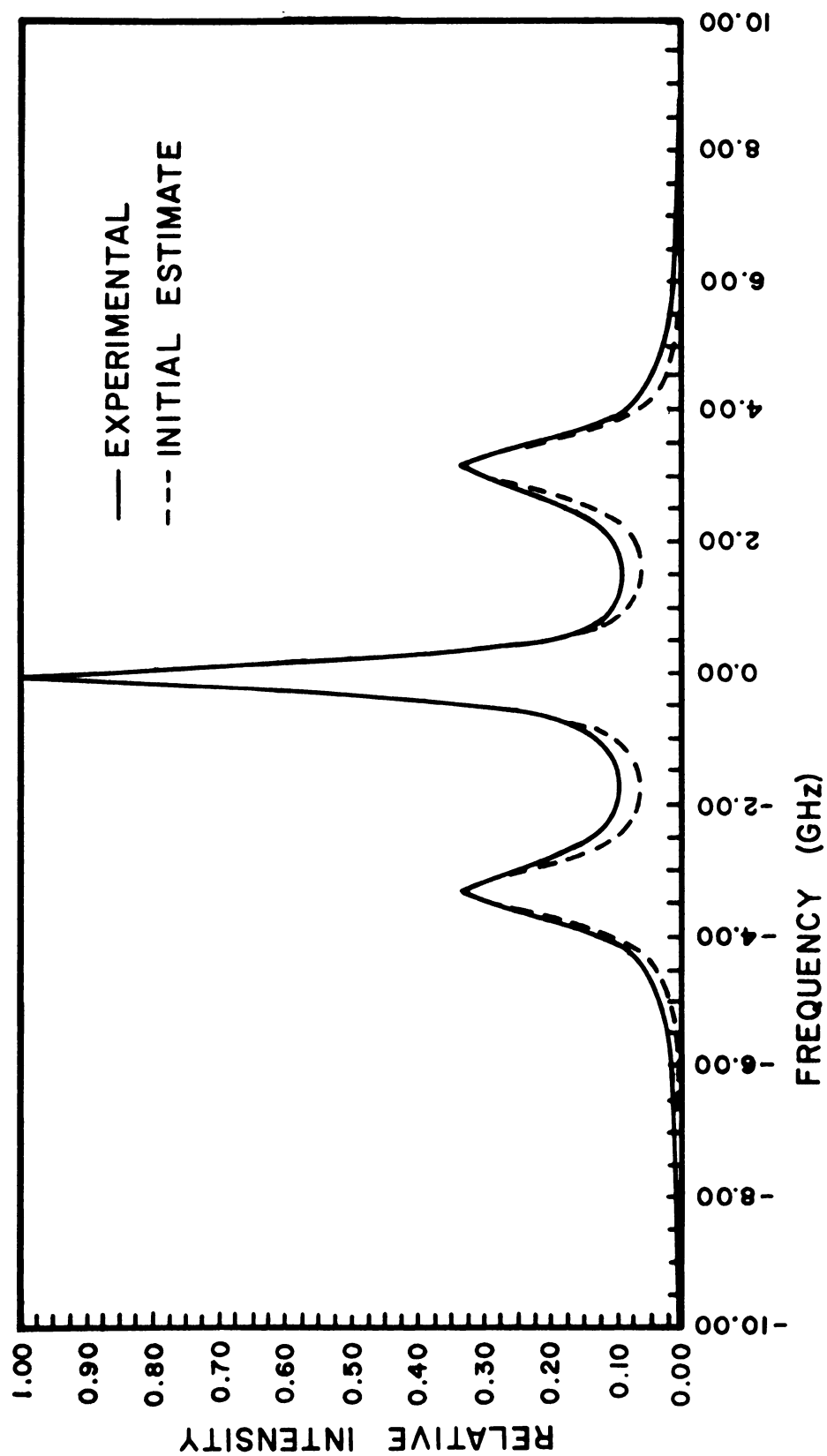
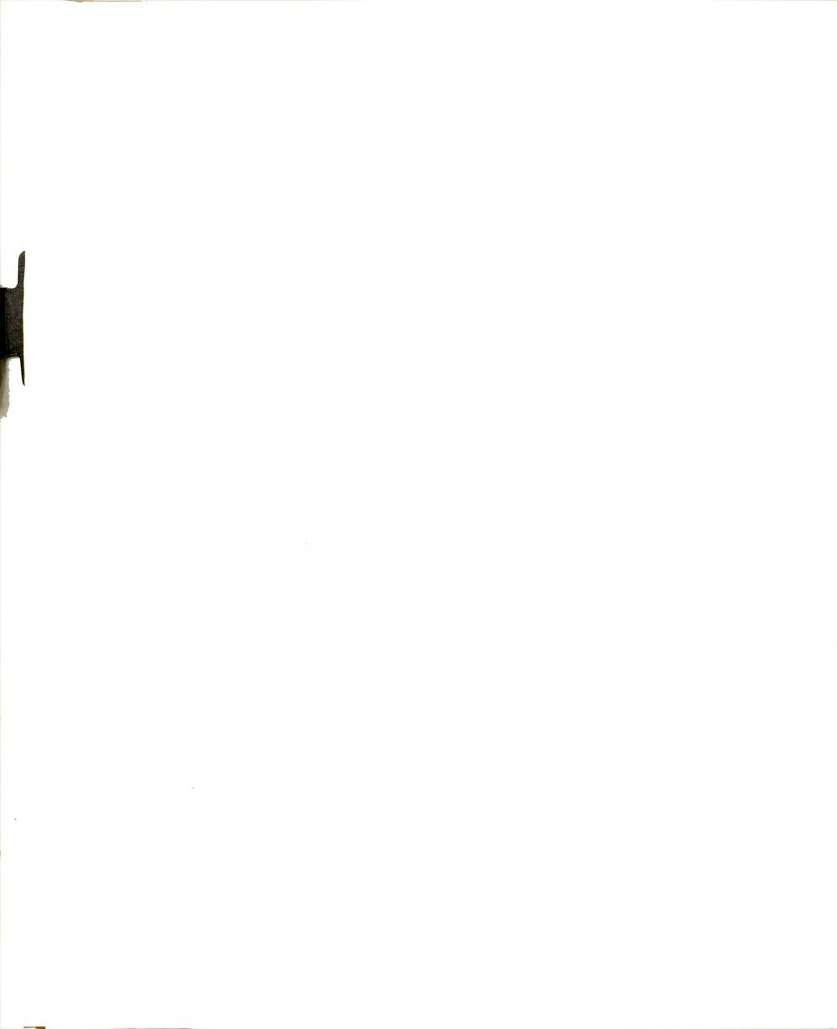


Figure 3.7. Final Curve Fit for Trilorentzian Model.



BSPEP determines the parametric values which minimize the sum of the weighted squares of the residuals. The residuals are the differences between the experimental and theoretical intensities at a given frequency. The weighting factors are inversely proportional to the variance of the observation. Wentworth (71) and Wolberg (72) have discussed the definition, theory and application of these statistical concepts. It should be emphasized that minimization of this functional (sum of weighted residuals) implies an assumption of the data having uncorrelated, normally distributed errors and that the final curve fit is not biased by the residuals being coincidentally small.

Several mathematical techniques for this minimization were investigated; the numerical technique incorporated into BSPEP may be identified as an iterative-linearized-least square technique. BSPEP uses computer time most efficiently because of analytical evaluation of derivatives, a natural evolution of statistics describing the solution, and a lack of versatility, generality incorporated into the other previously available programs. A program using the variable metric technique of Davidon (75) was not adopted. Even though it was efficient in terms of the number of iterations required for convergence to the final solution, it still required more computer time for each iteration and for the evaluation of statistical parameters characterizing

the solution. A curve fitting program (74), in which derivatives are not calculated, and a program in which one uses differencing techniques to estimate the derivatives were not adopted either. The pertinent derivatives can be analytically evaluated fast enough that their increased accuracy reduces the total required computer time.

BSPEP also differs from the other linearized least square type programs in that its normal equations are solved by diagonalizing, with Jacobian rotation, the coefficient matrix rather than using straight forward matrix inversion. This procedure allows one to incorporate diagnostic least square techniques (76) which yields information relative to the linear independence of the parameters being evaluated. Since the coefficient matrix is symmetric, this method of solving these equations is among the fastest and most accurate methods. The numerics are also improved by setting the off diagonal elements of the diagonalized matrix identically to zero before calculating the reciprocals of the diagonal elements and "rotating the matrix back".

Not only does diagnostic least squares allow one to detect linear dependence (rigorous or coincidental for a particular data set), it allows one to identify the corresponding parameters. This mathematical technique also allows one to obtain a solution in spite of linear dependence. Even though these solutions are not rigorously correct, they may have practical value (76).



These computer programs were compared using some actual experimental data and some calculated data sets. The calculated data sets utilize a single relaxation model and parameters taken from a published Brillouin spectrum for carbon tetrachloride (28). Randomly generated errors, with different RMS values were added onto the various data sets.

The detailed theory of the techniques used in BSPEP are discussed by Wentworth (71), Wolberg (72), Deming (73), and Curl (76) and will not be explained here. A flow chart illustrating this program appears in Figure 3.8. The first data card contains computer program codes and parameters; the details of this data card are indicated in Table 3.4. The next card contains initial estimates of the Brillouin spectra parameters; the format for this card is 8F10.5. Then the cards containing the spectral data are read in format 8E10.5. Finally, control information for the subroutine GRAPH is read in if computer plotting is desired. These cards are discussed extensively by Knirk (70).

The output of BSPEP is well labelled. The printed output for a given iteration contains:

1. experimental, theoretical and difference curves
2. weighted and unweighted rms errors
3. coefficient matrix for normal equations

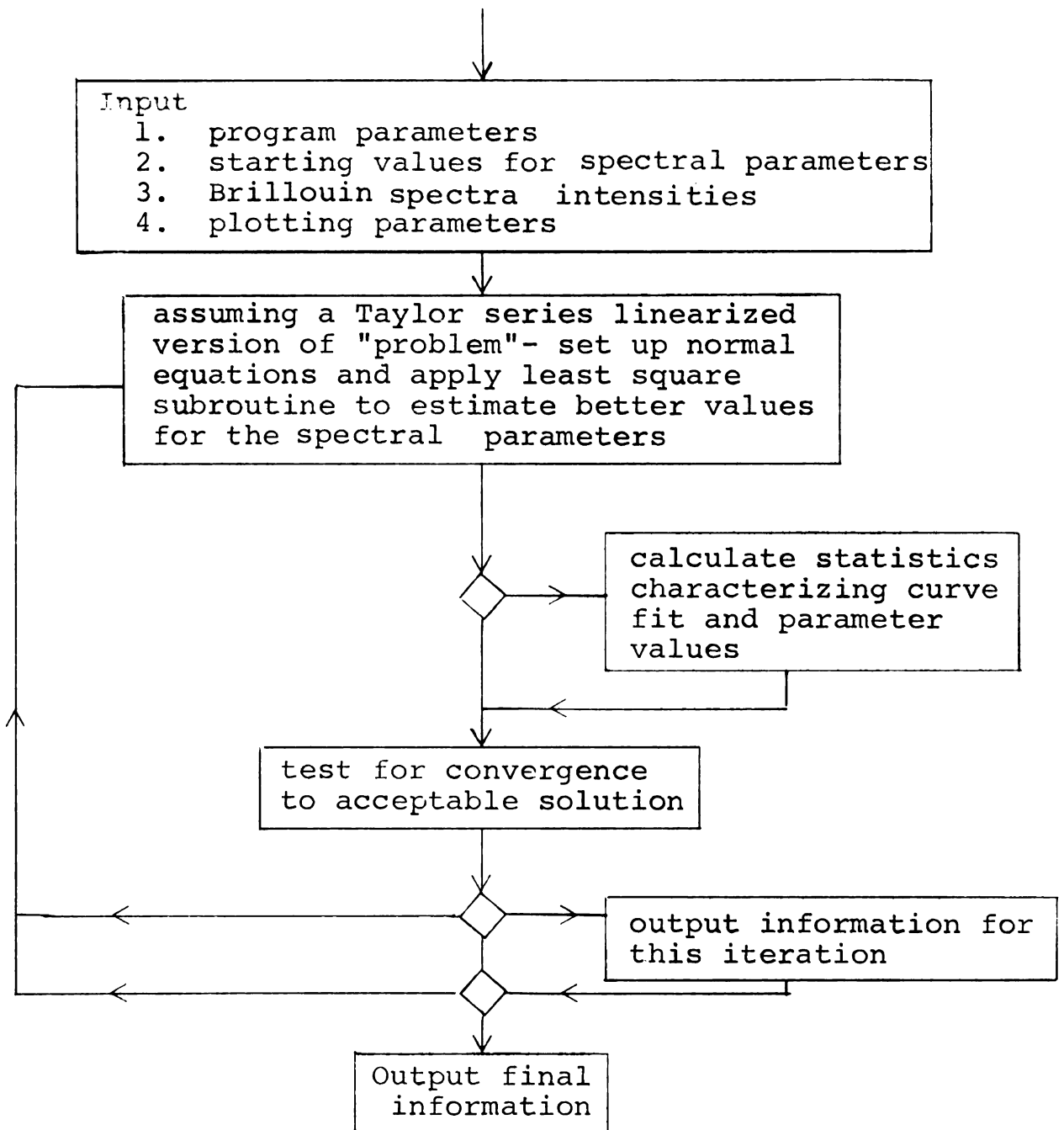


Figure 3.8. Flow Chart for BSPEP.

TABLE 3.4.--Program Parameters for BSPEP.

Parameter	Column	Format	Code	Definition and Comments
ND	1-5	I5		number of data points
DW	6-20	F15.5		value of frequency interval
SC	21-35	F15.5		intensity scale factor
NP	36-40	I5		number of model parameters
NPLT	41-45	I5	0	do not plot
			1	plot
IOIT	46-50	I5	0	do not output iteration information
			1	output curve fit statistics, etc. on each iteration
EPS	51-60	F10.5		criterion for convergence
IMAX	61-70	I10		maximum number of iteration allowed
TBETA	71-80	F10.3		statistical parameter for confidence interval of estimated parameters



4. diagonalized coefficient matrix
5. Jacobi rotation matrix for the diagonalization
6. adjusted-diagonalized coefficient matrix
7. rerotated (inverse of original coefficient matrix) matrix
8. new values for the model parameters

After the final iteration, in addition to the above if it was requested, the printed output contains:

1. variance-covariance matrix
2. final value for model parameters
3. unbiased estimate of parameters' standard error
4. correlation coefficient matrix
5. parameter confidence interval
6. experimental, theoretical and difference curves
7. weighted and unweighted rms errors

In addition to this printed output, one may obtain some plots from a Calcomp plotter. The exact nature of these plots (size, scaling, labelling, etc.), generated by the subroutine GRAPH is controlled by information read into the computer. If plots are requested, two plots are always obtained. The first plot contains an experimental and a theoretical curve using the initial estimates of the spectral parameters, see Figure 3.4. After the computer program has converged to a solution, a similar graph is generated. The final values for the spectral parameters are utilized in the theoretical curve, see Figure 3.5.

The convergence of BSPEP to a solution was studied as a function of the rms experimental error. This study has a practical application in that it indicates what type of experimental precision and accuracy are necessary if one ultimately expects to deduce a liquid's parameters from its Brillouin spectra accurately. The theoretical data sets previously mentioned were used for this purpose. If the rms error was greater than 0.2% to 0.3%, BSPEP would not converge to numerically good solutions. This deficiency was also demonstrated by the evolution of linear dependence between the halfwidth and amplitude of the secondary (smallest contribution) central peak. The 0.2% convergence limit above can be increased if one applies the curve smoothing technique of Savitzky and Golay (77). A subroutine SMUTH was written for this purpose.

## CHAPTER IV

### INSTRUMENTAL SYSTEM

#### General Design Aspects-Introduction

A schematic of the Rayleigh-Brillouin spectrometer which was designed, constructed, optimized, and characterized is illustrated in Figure 4.1. This block diagram divides the spectrometer into its subsystems emphasizing the instrument's high versatility for both photometric and spectral experiments. Briefly, the instrument consists of optical sources suitable for performing scattering experiments on matter in any state, devices for controlling the nature of a sample, optical analyzers and detectors which characterize the scattered radiation.

In order to provide a versatile, precision spectrometer, the following components or subsystems were incorporated: (1) A convenient vibration-free optical table was constructed. (2) Stable, single frequency helium-neon lasers were investigated extensively; however, an argon ion laser (single mode, frequency stabilized) was finally adopted. (3) The incident optics subsystem consists of a rotatable mirror which can be translated along an optical rail. This subsystem controls the direction

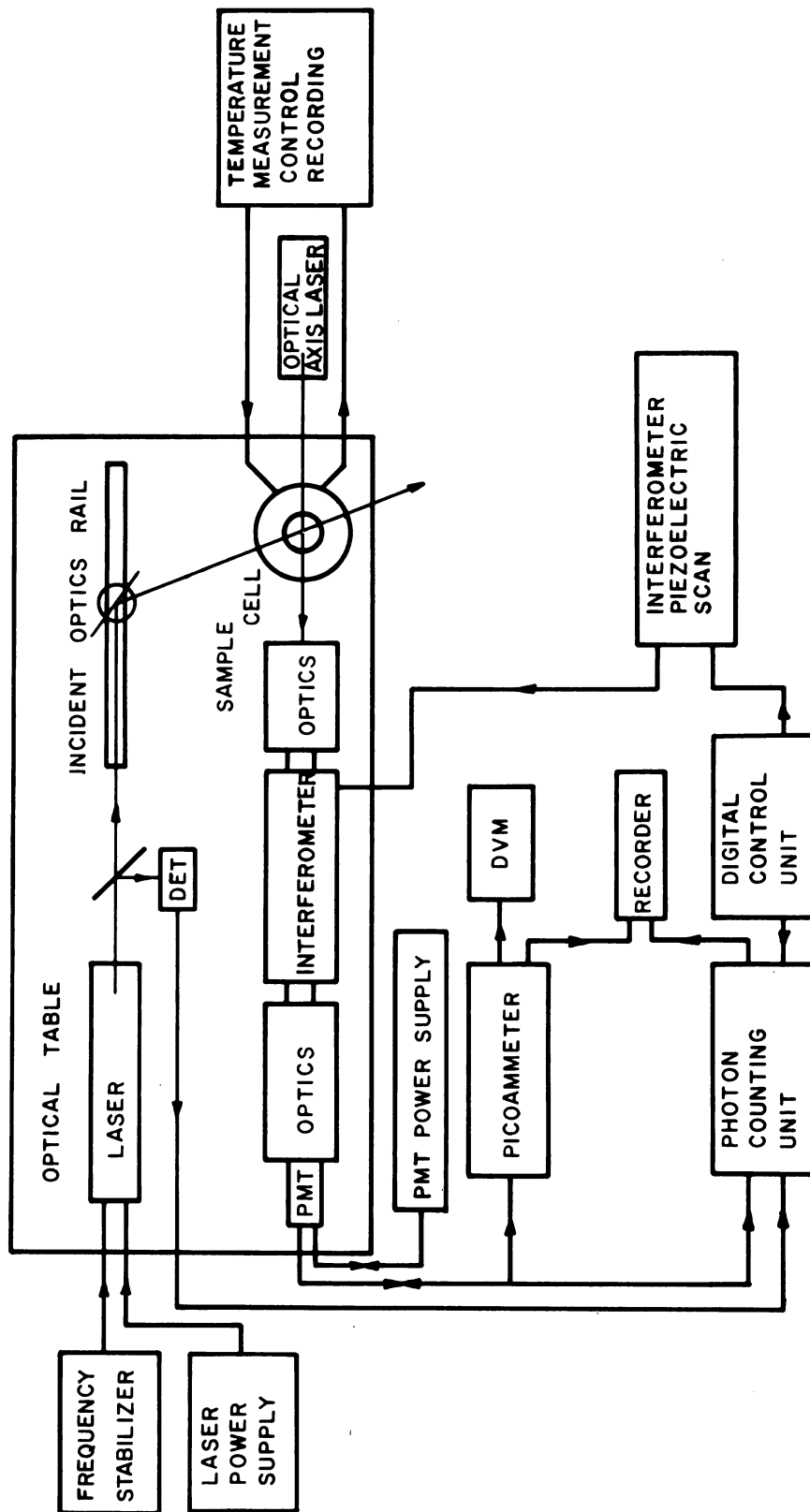


Figure 4.1. Rayleigh-Brillouin Spectrophotometer.

of the incident light beam. Since it is impractical to move the optical source and the optical detection system must remain fixed and rigid, the direction of the incident beam relative to the optical detection axis is varied with the mirror. Lenses, attenuators, filters, quarter wave plates, etc. may also be mounted onto the rail to control the collimation (divergence and convergence), intensity, polarization, etc. of the incident light beam according to the demands of a particular experiment. (4) The sample cell system was designed and constructed to minimize multiple light scattering effects, to permit the use of a variety of samples or sample cells, to facilitate accurate temperature control and measurement, and to allow measurements as a function of the scattering angle about a vertical axis. (5) A temperature measurement-control subsystem which will control the temperature of the sample cell to within  $\pm 0.001^{\circ}\text{C}$  over the range  $0^{\circ}\text{C}$  to  $120^{\circ}\text{C}$  was incorporated. The temperature measuring equipment has been calibrated to give the system an accuracy better than  $\pm 0.01^{\circ}\text{C}$ . (6) The collection optics consists of a lens-aperture combination which collects the diverging scattered light over a small (variable) cone angle and transforms the beam into a parallel beam for Fabry-Perot interferometry. In order to study the character of a scattered light beam relative to a property other than, or in addition to, frequency distribution, optical components

such as a polarization analyzer may be inserted into this parallel beam between the collection lens and interferometer.

(7) The light beam then passes through a piezo-electrically scanned Fabry-Perot interferometer. Different mirrors may be easily mounted, spaced and aligned to emphasize or compromise between resolution and free spectral range.

Also, the mirrors may be excluded in order to eliminate spectral decomposition of the scattered light beam. (8) The emergent light beam is then focused onto a pinhole in front of the photomultiplier tube to facilitate resolution. The photomultiplier tube is housed in a refrigerated chamber to reduce the noise and increase the signal-to-noise ratio.

It is wired in a fashion which allows either analog or digital detection electronics. (9) The detection electronics are extremely versatile because they are modular in nature and are connected in a "bread board" fashion. This arrangement allows one to adopt the best electronic system for a given experiment; that is, it permits the experimenter to compromise between complexity, inconvenience, necessary precision, resolution, etc.

Either classical analog techniques or some of the more modern digital photon counting techniques may be used. The photon counting techniques were incorporated primarily because they increased the convenience of collecting digital data. At low intensity levels, it also tends to improve the signal-to-noise ratio and allows one to

study the statistical character of a light beam. A split beam is available providing a reference beam; hence, intensity fluctuations of a light source may be at least partially compensated by ratio like measurements.

### Optical Table

When this research was initially undertaken, the only vibration free optical tables commercially available were expensive. An optical table utilizing inexpensive and readily available materials was designed and constructed. The design incorporates a compromise between high mass damping of vibrations and an unsafe load on the floor.

The construction of the optical table is illustrated in Figure 4.2. This figure shows only one of the table's six legs. A rubber pad (B. F. Goodrich grade 086 neoprene rubber) 1/4 inch thick lies on the floor. A standard 100 pound grease barrel with a 1/8 inch steel plate spot welded onto the bottom of it, sets on the rubber pad. The barrel is filled with a dry, fine silica sand.

A steel plate, and then another neoprene rubber pad, rest on the top of the sand. A scissor-type axle jack sets on top of these plates and is spot welded to the I-beam.

Two 8 inch, wide flange I-beams traverse along each side of the table; three of the legs described above support each I-beam. The two I-beams are connected





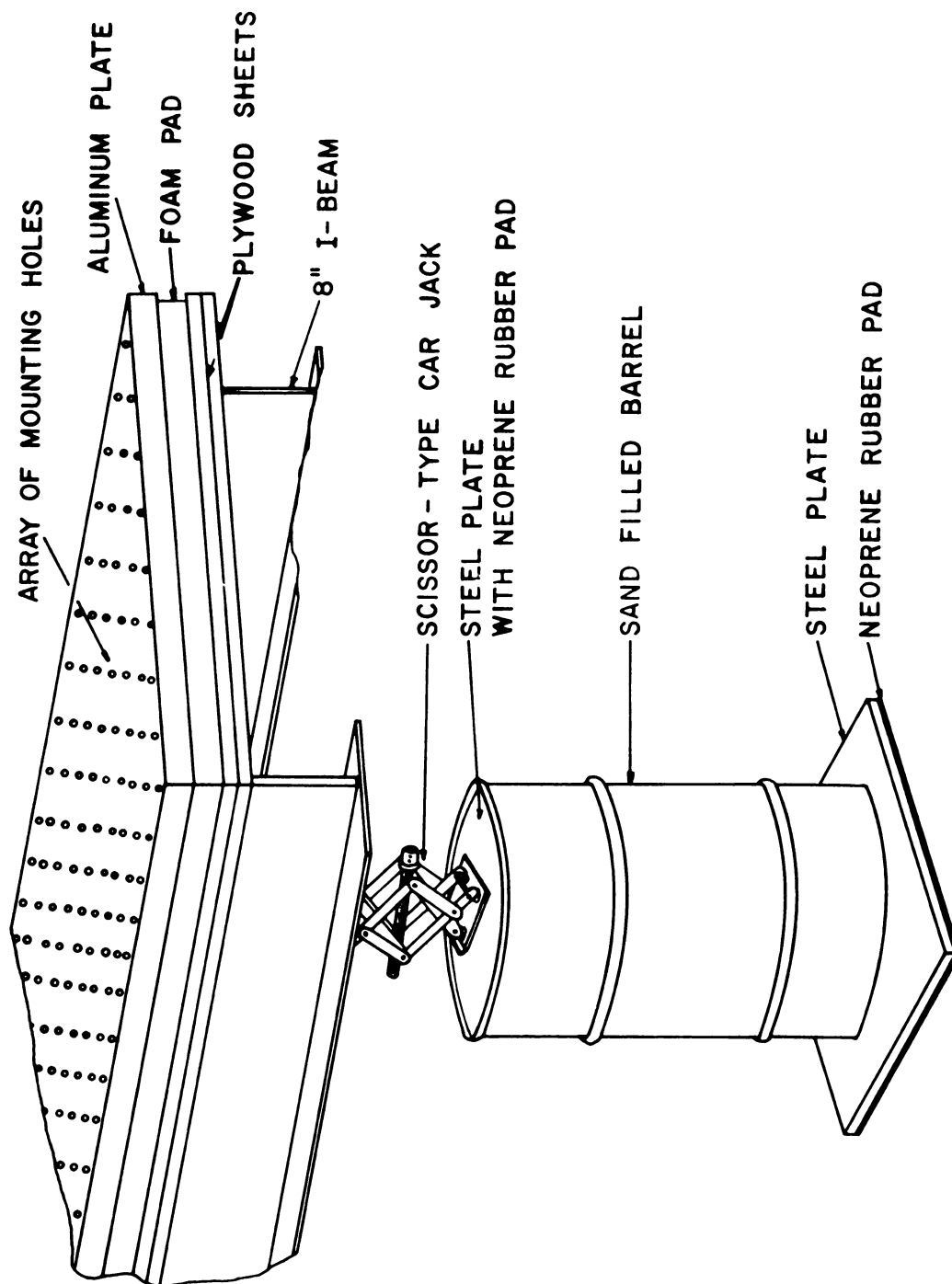


Figure 4.2. Optical Table.

together with 4 inch channel iron beams and two 4 inch channel iron beams rest on these cross members. All of these beams were welded together in a nonsymmetric arrangement to reduce the likelihood of resonant acoustical frequency vibrations.

Two layers of 3/4 inch plywood were bolted on the top of the I-beam structure and a foam pad was laid on top of these red plywood sheets. The foam pad is 2 inches thick and consists of U. S. Rubber type M-Ensolute vinyl sponge material (modified polyvinyl chloride).

A 4 feet by 12 feet, 1 1/2 inch thick, 1200 pound aluminum tool and jig plate floats on the foam pad. The aluminum plate was drilled and tapped in a 6 inch by 6 inch array to facilitate rigid mounting of the optical subsystems. Stainless steel helices were inserted into the holes in order to avert the thread stripping problems common with tapped aluminum holes; the threads receive 1/4-20 bolts. The top of the table is 46 inches above the floor; this height can be adjusted over a small range by the supporting axle jacks.

After construction was completed, the vibrational nature of the table top was studied qualitatively by placing piezo-electric transducers onto it and onto the floor which, in turn, were interfaced into an oscilloscope display. All of the high frequency vibrations were damped beyond the sensitivity of these vibration detectors. The only

significant low frequency vibration corresponded to the entire table moving up and down as a unit and hence did not affect the optical experiments. Pulses originating from a slammed door or a heavy item dropped onto the floor were evident; however, they were greatly attenuated and damped quickly. The most serious disadvantage of the optical table is its sensitivity to a bumping of the floating table top. However, this is not very serious if one does not disturb the system while aligning optical components or when collecting data. The mounting of the detection electronics into relay racks or placement onto a nearby desk also reduces this disadvantage.

### Light Sources

#### Traditional Light Sources

Because of its inherent properties, a laser is usually the best optical source for light scattering experiments; however, this instrumental system is not limited to the use of lasers. A traditional light source may easily be substituted for a laser. In the early phases of this project, a grating monochromator with a tungsten and a deuterium lamp was found advantageous when a wide, continuous wavelength range was desired. Sodium vapor, mercury arc, and some Osram high pressure lamps were useful when monochromaticity was not extremely important and an intense light source of wavelengths not available from lasers was desired.



## Lasers

The fundamental theory of lasers will not be presented; Bloom (78), Garrett (79), Heard (80) and Tomiyasu (81) have provided proficient texts and a bibliography of the extensive laser literature. However, it should be emphasized that lasers are the most important optical sources for this instrumental system because they are inherently very monochromatic, well collimated, polarized and coherent without compensating their relatively high intensity. Furthermore, the frequency stabilization of laser outputs has been accomplished.

At the onset of this project, an ion laser acceptable for Brillouin spectroscopy was not available. Moreover, this laboratory possessed the technology to construct rf excited He-Ne lasers (82); hence, the design and construction of rf excited lasers was undertaken. Two difficulties were quickly encountered: (1) The rf excitation interfered with the detection electronics. (2) The lifetimes of these plasma tubes were short compared to dc excited tubes. Meanwhile, laser plasma tubes with dc electrode systems became available commercially. The design and construction of two stable, single mode helium-neon lasers incorporating such plasma tubes was pursued (see Appendix); unfortunately, the two lasers do not yet perform satisfactorily for Brillouin spectroscopy. During this laser research, several general purpose helium-neon lasers were acquired

or became temporarily available from colleagues: A Siemens model LG-64, Quantum Physics model LS-32, Spectra Physics model 120 Stabilite with a model 256 Exciter, and a Spectra Physics model 132-01. Even though these lasers are useful for optical alignment and some experiments, they are inappropriate for Brillouin spectroscopy because of their relatively low output intensities (less than 10 milliwatt), thermal instability (frequency drift), and multimode (broad) frequency distribution. Deficiencies are manifested primarily in two manners: (1) Brillouin/Rayleigh line resolution is poor and line shape analysis is impossible for the broad instrumental profiles. (2) It is difficult to visually inspect a scattered light beam at various points along the detection optics train because of low intensity scattering. The latter factor is especially evident when the sample is a pure liquid. In principle, this difficulty can be circumvented if a laser beam scattered from a pinpoint, Ludox, polymer or soap solution is used for optical alignment but this technique does not completely eliminate the difficulties. The interferometer may lose its alignment (thermal instability) while the alignment media and sample cell are exchanged.

A powerful (80 milliwatt) Spectra Physics model 125 helium-neon laser was very helpful in detecting and specifically defining some of the Brillouin spectrometer's problems in addition to performing some early experiments.

However, it is a multimode laser and is not the most suitable light source for Brillouin spectroscopy.<sup>1</sup> Finally, a Coherent Radiation model 52 argon ion laser and a Spectra Physics model 165 argon ion laser (both with single mode frequency stabilizing adaptors) were experimentally considered and the Spectra Physics argon ion laser was incorporated.

#### Argon Ion Laser

An argon ion laser, stabilized with an internally placed, tilted, solid Fabry-Perot etalon (83,84,85), was incorporated because: (1) The argon ion laser can provide stable, single mode intensities up to 500 milliwatts whereas the helium-neon lasers, presently, can only provide stable, single mode output powers up to about 75 milliwatts. (2) Six different, useful wavelengths are inherently available. (3) Scattered light is two to four times as intense for these argon ion laser wavelengths compared to the helium-neon laser wavelength because of the Rayleigh  $\lambda^{-4}$  factor. (4) Photomultiplier tubes are generally more sensitive to the argon ion laser's wavelengths.

The Spectra-Physics argon ion laser, model 165-03, if appropriately aligned, provides single mode outputs at 5145 Å and 4880 Å up to about 500 milliwatts. The

---

<sup>1</sup>Now Spectra Physics will provide an attachment which will convert the multimode unit into a stable single frequency unit of low output power.

internal etalon is made of titanium silicate and has a temperature coefficient of  $\pm 3 \times 10^{-8}$  per  $^{\circ}\text{C}$ , providing thermal stability. The instantaneous bandwidth of the output power was measured to be less than 5 MHz (limit of the oscilloscope measurement) and the central frequency drifted less than 10 MHz over a ten hour period. Frequency stability is specified as 18 MHz/ $^{\circ}\text{C}$ . The beam diameter is between 1.3 and 1.5 mm depending upon the operating wavelength. A long radius optical cavity configuration maintains the beam's divergence at 0.5 milliradians. A beryllium oxide plasma tube insures long life times; they are excited (with feedback control) in a manner which maintains the output power to within 0.5% over 10 hour periods. The mirrors are external, thus the plasma tube's Brewster windows provide a linearly polarized light beam. Initially the tube is oriented to provide a vertical polarization vector; if not vertical enough, a polarization rotator accessory, a rotatable half wave plate, may be mounted directly onto the laser and the polarization vector made vertical or any other orientation desired.

#### Incident Optics

The incident optics subsystem is composed of a rotatable, tiltable mirror mounted onto an optical rail. The mirror is slid along the optical rail and rotated in order to send the incident light beam into the sample from



different angles in the plane of the table. The length of the rail (1 meter) limits the range of angles obtainable with the rail in a single position on the table; however, the rail can be relocated relative to the sample cell system and angles within the range 0 to 175 degrees are obtainable. Front surface mirrors were used to alleviate beam alignment problems.

The optical rail also serves as a mount for other optical components such as: (1) lenses to improve the collimation of an incident beam or focus it to a point at the sample's center, (2) bandpass filters and polarizers, (3) neutral density filters or a rotated polarizer to change the incident beam's intensity, (4)  $\lambda/2$  wave plates to rotate the polarization vector of an incident beam.

### Sample Cell System

#### Variable Scattering Angle Mechanism

Many light scattering experiments require the measurement of the scattered light as a function of the scattering angle. Many other experiments are performed at a fixed scattering angle but it is important to know this angle to a rather high accuracy. This latter point is well discussed in the depolarization ratio studies of Anderson (82) and the Landau-Placzek ratio studies of Cummins (32). The problem of varying the scattering angle with good accuracy is complicated by the weight of the

laser and rigidity requirements of the detection optics which includes an interferometer for frequency analysis. Therefore classical experimental arrangements are not acceptable. An acceptable arrangement for angular measurements was published by Chiao (86) and our system utilizes this concept.

The sample cell which is placed inside its thermostating jacket, is mounted at the center of a rotating table. Two adjustable pinholes are mounted along the diameter of this rotating table which can be set to define the direction the incident light beam must travel for a given scattering angle. A Bridgeport model RT-15 (15 inch diameter) rotary table used by machinists on milling machines was used as the sample table. This rotary table is mounted on two (highly parallel surfaces) aluminum plates. The top plate (11" X 17" X 1") is bolted to the rotary table and the lower plate (15½" X 18½" X 1½") is clamped to the optical table. This lower plate is grooved around its perimeter to collect any oil leaking from the rotary mechanism. It also has a key bolted to it which fits into a groove in the bottom of the upper plate. The bottom plate also has a vertical bracket through which a bolt pushes against the upper aluminum plate. This arrangement allows the center of the rotating table to be aligned with the optical axis of the detection optics train. The thickness of these two plates was made

just large enough to allow convenient rotation of the handle which is used to rotate the table. The Bridgeport table top is 7 inches above the optical table. The optical axis is 10 inches above the optical table.

A 6 inch wide plate is mounted onto the rotary table. At the center of the plate is a 1 inch diameter rod which fits into the table's centering hole. Coaxial with this rod, a 1/4 inch diameter pin extends upwards onto which the sample cell housing is centered. Two x-y microscope stages at the ends of the plate are used as mounts for the pinholes. The plate also contains centering pins so that the sample cell housing or pinhole assemblies may be taken off and later replaced into the same position on the rotary table.

With the rotatary table set at zero angle, the plate is fixed so the pinholes are close to the detection optics axis defined by an alignment laser beam. The microscope stages are then adjusted so that the pinholes are centered onto this beam. Now if the table is rotated by an angle  $\theta$  and the direction of the incident light beam is adjusted so that the beam goes through these pinholes, the scattering angle (viewing angle) is  $\theta$ .

The accuracy of the Bridgeport rotating table is specified to be within 30 seconds of arc through a complete rotation (vernier readings to within 5 seconds). However, this uncertainty is not the limiting factor in

determining the scattering angle. The alignment pinholes are 0.74 mm in diameter and are located approximately 15 cm from the center of the table. Assuming the incident beam is adjusted so that its center coincides with the pinhole's center to within one-half of the pinhole's diameter, the error angle is 2.5 milliradians or 8.6 minutes of arc. This uncertainty is large compared to the uncertainty above, however it is not a serious experimental limitation. Reference to Cummin's article (32) indicates that uncertainties of this value (8.6 min.) or less, insures that a Brillouin shift may be measured to within 0.1% for scattering angles greater than 15 degrees.

#### Sample Cell and Thermostatting Jacket

A simplified diagram of the thermostatted sample cell subsystem appears in Figure 4.3. This subsystem is composed of a hollow copper cylinder thermostat insulated on the outside and with a sample cell inside. The cylinder is 4-3/4 inches long and 3-1/4 inch diameter. The inside cavity, which houses the sample cell, is 3 inches long and 2 inches in diameter. The copper base plate is 1/4 inch thick and is bolted to the insulating base plate. A recession is machined, into which a cooling coil is soldered, into the outside of the copper cylinder. The cooling coil is bihelically wound and its ends extend through the top of the assembly for connection to an



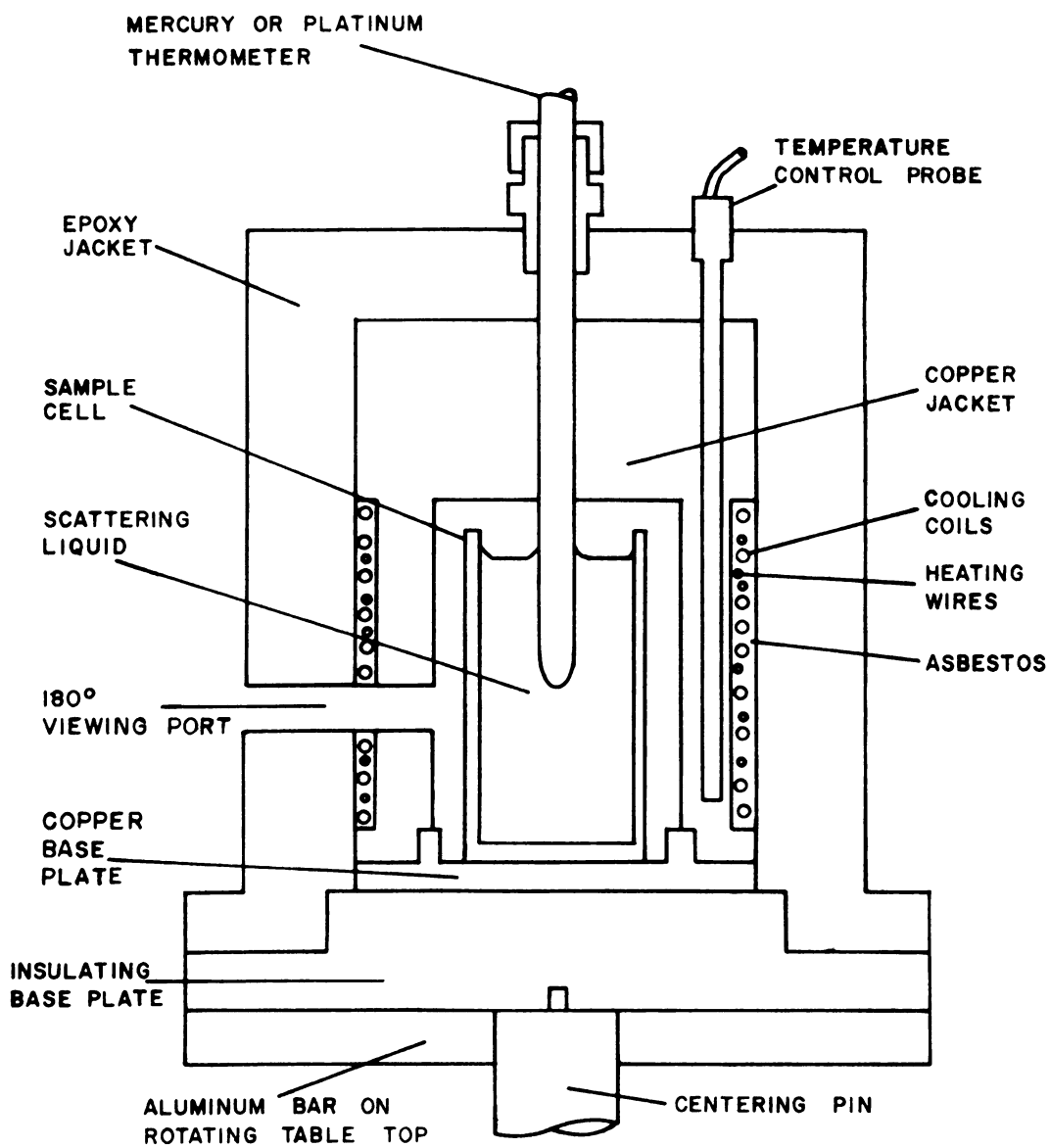


Figure 4.3. Thermostatted Sample Cell.



external coolant supply. Asbestos tape was wound in between the tubing windings. Over the asbestos tape a nichrome wire heating element was wound bihelically, yielding a 13.5 ohm heating element. The rest of the copper cylinder recession was filled with an asbestos paste (aqueous slurry) and dried. The nichrome wire was connected to binding posts on top of the housing. The copper cylinder also had a 3/8 inch high viewing port machined 180° around its circumference.

A 7/8 inch thick epoxy resin shell was machined to fit over the copper cylinder and is bolted to the copper cylinder, on top, so that the entire jacketing system can conveniently be lifted on and off with the sample cell setting in place. The epoxy jacket has a corresponding 180 degree viewing port. Teflon thermometer connectors usually used with tapered glass joints were remachined, threaded and screwed into the epoxy jacket on top. One connector was located so that a thermometer would protrude into the center of the liquid sample and the other connector was located off axis so that a thermometer would protrude into the copper cylinder. A hole through the epoxy shell into the copper cylinder provides a well for the controller's probe. Two other 4 mm diameter wells were drilled for the thermistor probes of the temperature monitor. One protrudes, off axis, into the liquid sample and the other into the copper cylinder.



The insulating base plate is one inch thick and six inches in diameter. It is constructed of transite.

Only two types of sample cells were used. The first is a Brice-Phoenix, model T-101, standard square turbidity cell 30 X 30 X 60 mm. The second type of cell is a standard cylindrical light scattering cell (89) with flat entrance and exit windows; its height was reduced to 7 cm so that it would fit inside the sample cell housing. These sample cells and the dimensions of this sample cell system were chosen because: (1) They were immediately available. (2) They are easily replaced since they are standard light scattering cells. (3) They represent a reasonable compromise between large diameter cells for which optical imperfections of the cell have less effect on the scattered light and a large amount of sample is required to fill the cell.

A thin film of Wakefield (No. 128) thermal conducting compound is inserted between the sample cell's base and the copper base plate upon which the cell rested. In addition to providing a good thermal connection to the copper base plate, the thermal compound holds the sample cell in place while it is being centered and then while the copper cylinder-epoxy shell assembly is dropped down over the cell into position. The thermal conducting compound is also used to insure a good thermal connection between the cylindrical copper shell and the copper base plate.

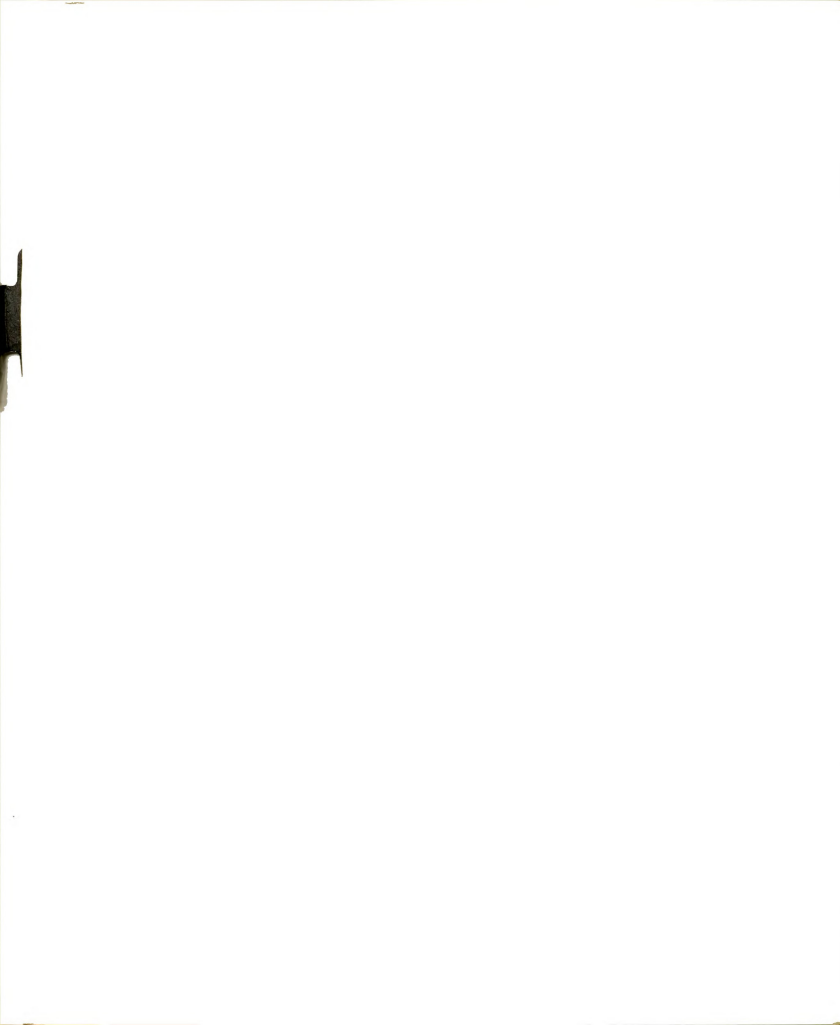
The temperature of the sample is controlled by directly controlling the temperature of the copper block, providing good thermal conductivity between the copper block and the sample cell, and allowing enough time for the sample to come to thermal equilibrium with the copper block. With this technique, the copper block provides a thermal mass larger than a sample by itself and enhances the ease of obtaining good thermal stability of the sample. Since the accuracy of the temperature controller's setting is only  $\pm 0.5^{\circ}\text{C}$ , the temperature of the copper block and sample were measured directly with a mercury thermometer unless very accurate measurements were desired. For the high precision case, an Electro Science Inc. model 300 PVB potentiometer/bridge and platinum resistance thermometer accessory was used. In order to facilitate knowing when a sample has reached thermal equilibrium, and to examine the sample's thermal stability, a temperature monitoring unit was provided.

When the temperature control parameters were appropriately set and the sample was allowed to reach equilibrium (less than 2 hours for temperatures up to  $100^{\circ}\text{C}$ ), no thermal gradients were detectable by temperature measurements made vertically along the central axis or the off center probe. The only temperature differences seen could be attributed to the  $\pm 0.001^{\circ}\text{C}$  temperature instability of the sample.

Even though this sample cell thermostat system was designed specifically for liquid samples, the instrument is not limited to experiments on liquids. Colleagues have successfully designed systems for handling over types of samples (87,88).

#### Temperature Controller

The temperature of the copper block is controlled with a Yellow Springs Instrument Company model 72 proportional controller. A proportional controller was utilized to reduce the temperature cycling associated with on-off type controllers. A model 409 temperature probe was incorporated and the control point, within the range 0 to 120° C, can be reset to within  $\pm 0.005^\circ$  C. A variac transformer was placed between the controller's output and the nichrome wire heating element with a 2000 ohm, 140 watt bleeder resistor across the variac's input to prevent fuse overloads. The variac was adjusted so that, at the control point, the conduction angle of the controller's SCR's was close to 90° with a bandwidth setting of 0.1° C. This increased the controller's sensitivity and hence the temperature stability. The temperature stability was increased from the manufacturer's specification of  $\pm 0.005^\circ$  C to  $\pm 0.001^\circ$  C as measured with the temperature monitor described below. As the manufacturer indicates, the actual control point temperature may deviate from the temperature setting by  $\pm 0.5^\circ$  C.

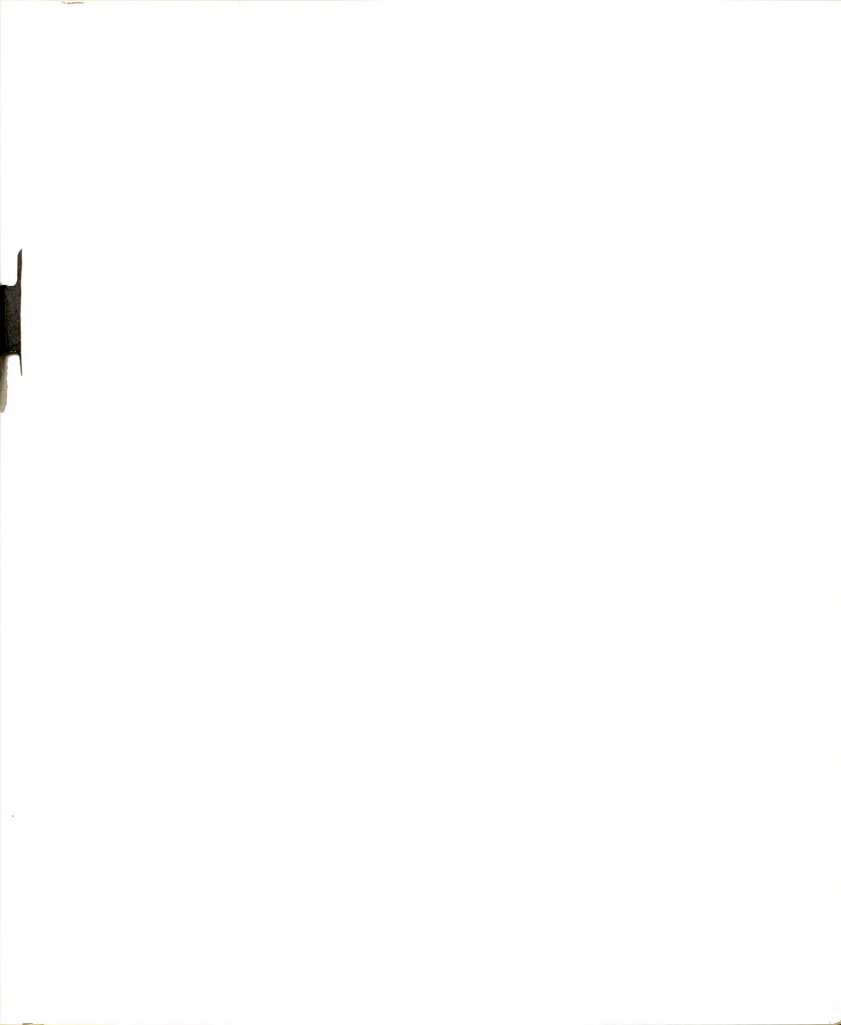


To facilitate a more accurate temperature setting, a measurement of the liquid's actual temperature versus the temperature setting was performed and the results are presented in Figure 4.4. Glycerin was used for this study and a platinum resistance thermometer, with an accuracy of  $\pm 0.003^{\circ}\text{C}$ , was used to measure the liquid's temperature.

#### Temperature Monitor

The block diagram in Figure 4.5 depicts the temperature monitoring subsystem. Two thermistor type probes were used to provide good temperature sensitivity. Yellow Springs model 44201 thermilinear thermistor components were used because they also provide a linear response. The temperature monitoring subsystem has two associated electronic recording systems: One system has a fixed 0 to  $100^{\circ}\text{C}$  temperature range for a one volt full scale recorder; the other electronic system has five ranges from  $0.01^{\circ}\text{C}$  to  $100^{\circ}\text{C}$  (on a 1 millivolt full scale recorder) and a baseline which may be changed from 0 to  $100^{\circ}\text{C}$ . This sensitive, zero shifted recording greatly enhances monitoring the sample temperature. A six pole-double throw switch is used to invert the probes relative to these two different recording systems.

The  $\pm 15$  volt power supply (for the operational amplifiers) is a full wave rectifier, filter network with 15 volt zener diodes across its output for regulation.



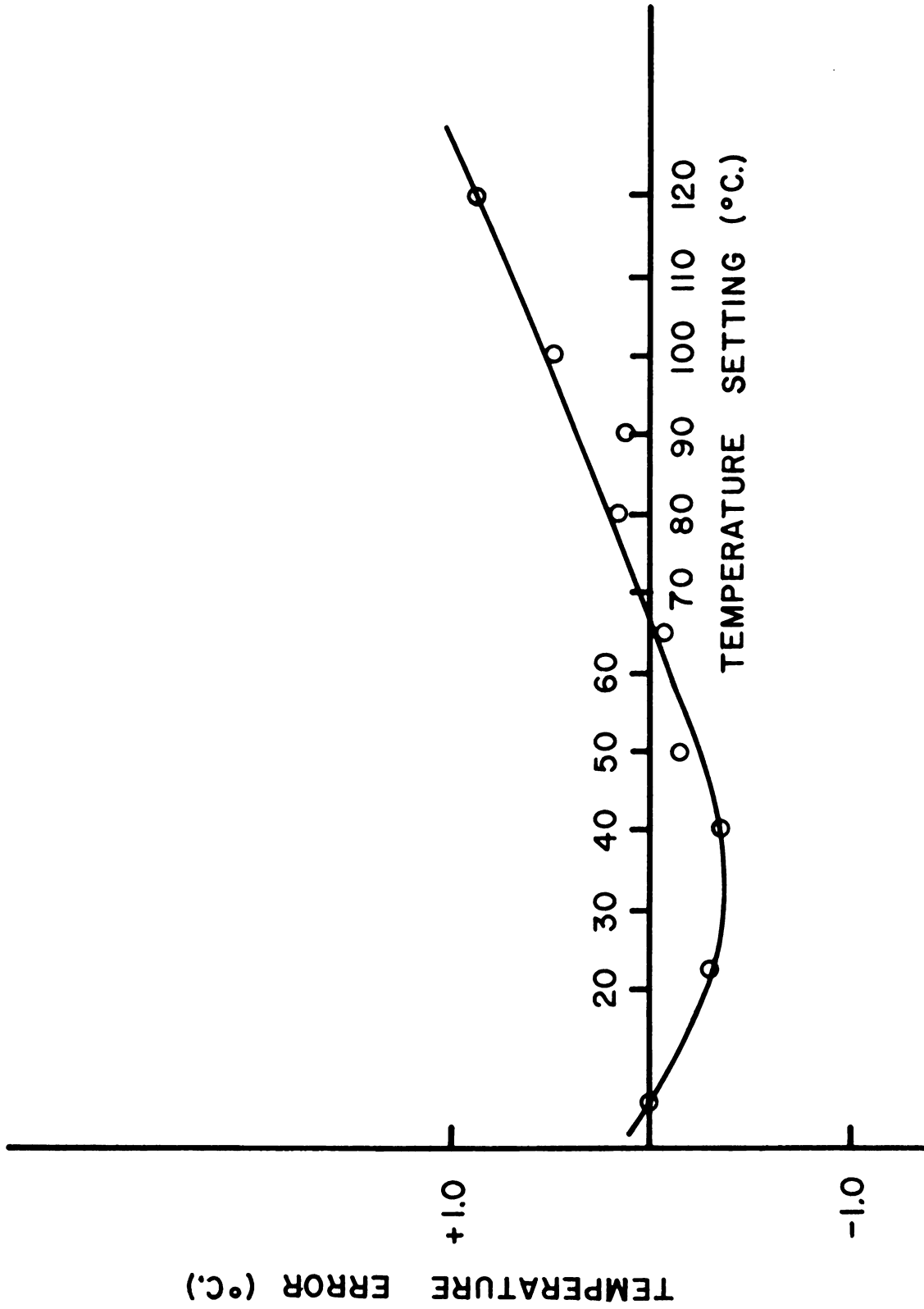


Figure 4.4. Corrections for Temperature Controller Settings.

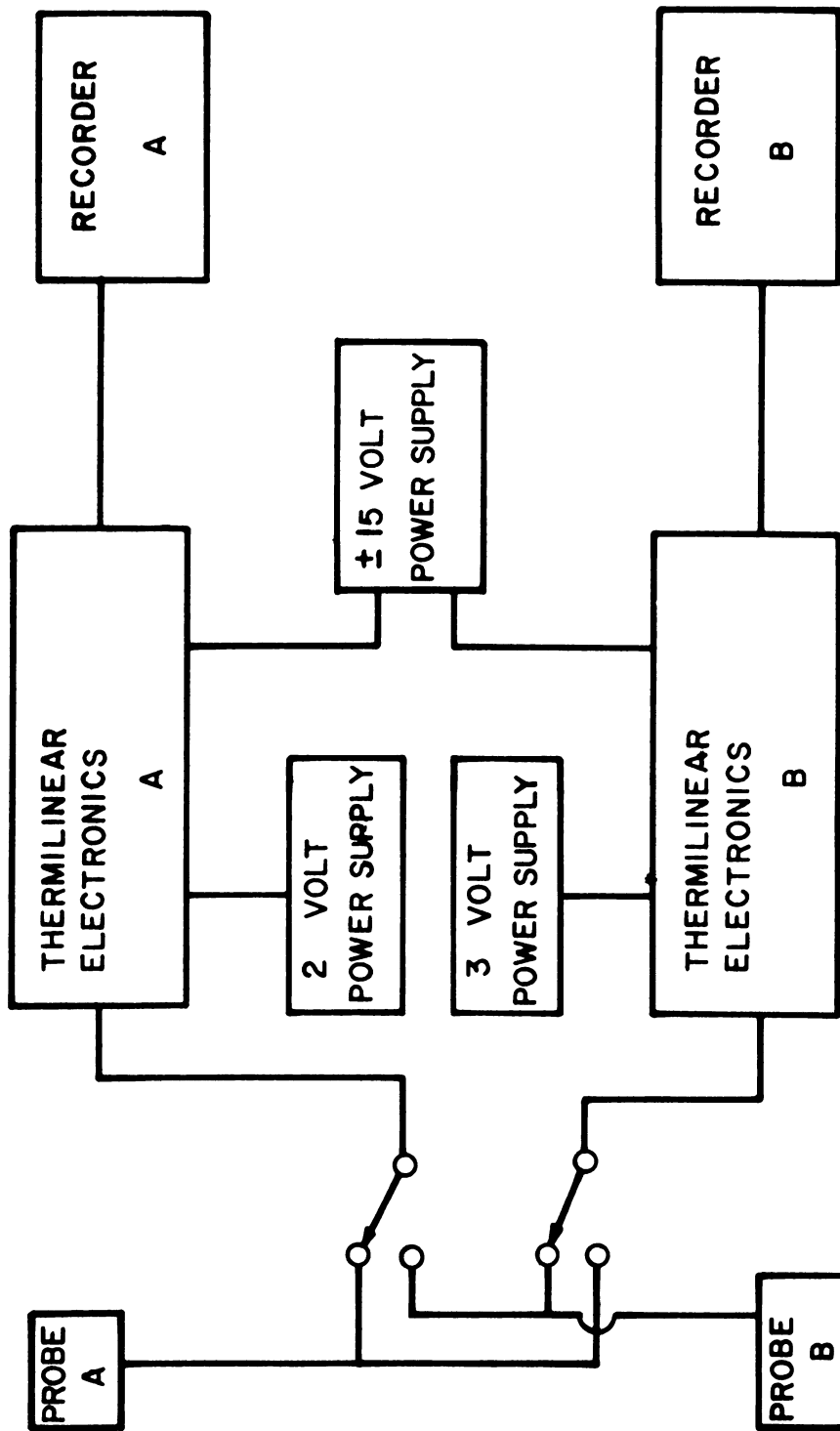


Figure 4.5. Block Diagram of Temperature Monitor.



The 2 volt and 3 volt power supplies are "battery eliminator" units which utilize a National Semiconductor model LM 304 precision voltage regulator (integrated circuitry) to supply an output voltage adjustable from 35 mv to 15 volt with 1 mv load regulation, 0.1% long term stability and 0.2 mv/v ripple rejection. In this application, the "battery eliminators" were adjusted with a potentiometer to yield 2.000 volt and 3.000 volt respectively.

The thermilinear electronics are illustrated in Figures 4.6 and 4.7. The thermilinear probe and resistor network (3200 and 6250 resistors) provide an output voltage (between A and G) given by

$$E_{out} = (-0.0053483T + 0.86507)E_{in}$$

where  $E_{in}$  is the voltage between points A and B. This equation is specified by the manufacturer. In thermilinear electronic system A,  $E_{in}$  was adjusted to yield a temperature coefficient of 10mv/°C; the voltage divider between A and D was adjusted to 1.869<sup>8</sup> volt. For a 0 to 1 volt recorder (and no signal simplification), the recorder scale corresponds to 0 to 100° C. With this input voltage,  $E_{in}$ , the voltage divider between A and E was adjusted to

$$(0.86507) (1.869^8) = 1.617^5$$

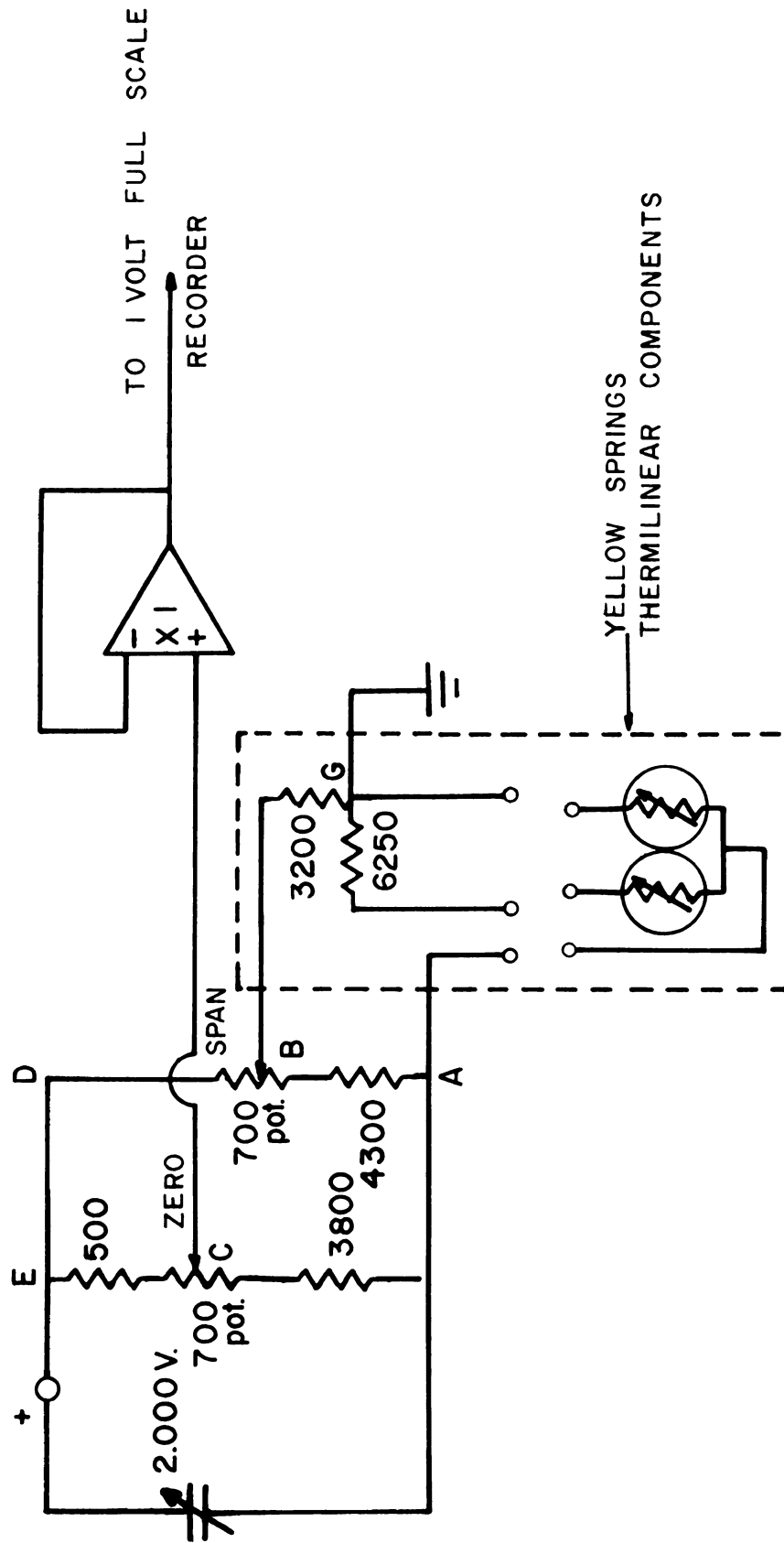


Figure 4.6. Thermilinear Electronics A.

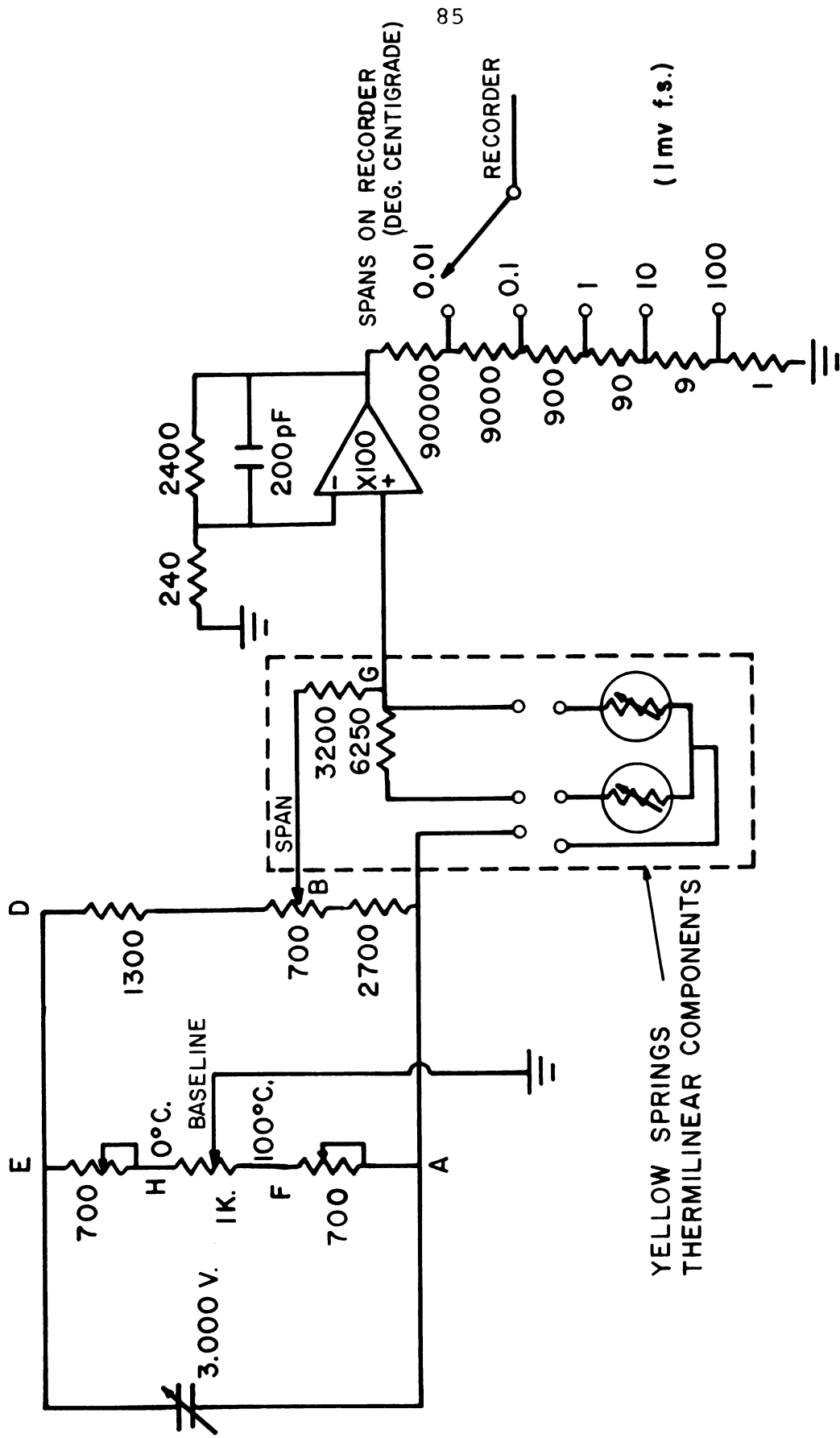


Figure 4.7. Thermilinear Electronics B.

volts so that the input voltage to the cathode follower is zero volts with the temperature probe at zero degrees centigrade and still has a  $10 \text{ mv}/^{\circ} \text{C}$  temperature coefficient.

The input circuitry is floating above ground and is well shielded to reduce noise pick-up. The cathode follower (an Analog Devices 142B solid state operational amplifier) is used to: (1) prevent loading of the voltage dividers, (2) to impedance match to any recording or measuring device and (3) to change the floating, temperature sensitive signal to a groundable signal.

The only significant differences between thermilinear electronic systems A and B are: (1) Because a Philbrick model P25A differential amplifier was used in an amplifying mode, the input signal was reversed in polarity to obtain an increasing output for an increasing temperature. (2) The signal is amplified by 100 and, via an attenuator, this unit provides five temperature ranges, from  $0.01^{\circ} \text{C}$  to  $100^{\circ} \text{C}$  full scale, to a one millivolt recorder. (3) The voltage divider AE is quite different. The two 700 ohm pots are set ("upper" one to about  $617.4^7$  ohms and the "lower" one to about  $382.5^3$  ohms) so that the voltages  $V_{AF}$  and  $V_{AH}$  are  $0.617^5$  and  $1.617^5$  volts respectively. The 1K ohm pot is a 0.1% accurate, 0.1% linear Helipot with a digital (0.0 to 100.0) readout dial. The baseline of the temperature recording may be changed from  $0^{\circ} \text{C}$  to  $100^{\circ} \text{C}$  and its temperature value can be read from the Helipot dial.

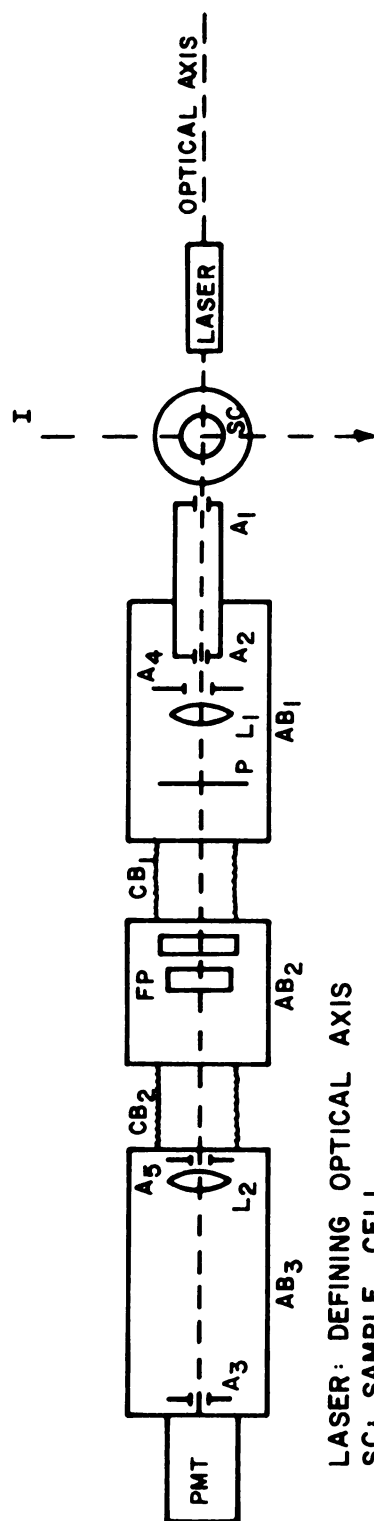
The temperature monitors were calibrated by setting:

(1) the two volt power supply, (2) the three volt power supply, (3)  $E_{in}$  voltages and (4) zero reference voltages with a potentiometer, after the trimmer pot etc. on the operational amplifiers were appropriately adjusted. The accuracy of these systems is relatively unimportant since they were used primarily to study temperature variations qualitatively. However, the temperature of a constant temperature bath was measured simultaneously with this device and a platinum resistance thermometer and the differences were of a random nature with  $\pm 0.3^\circ \text{C}$  rms deviations. This observation is in accord with the manufacturer's specifications of  $\pm 0.15^\circ \text{C}$  thermilinear accuracy and interchangeability of probes, and a  $\pm 0.216^\circ \text{C}$  linearity deviation for these model 44201 probes.

#### Collection Optics and Beam Analyzer

The collection optics collect some of the light scattered by the sample and transform it into a form appropriate for interferometric analysis; these optics are illustrated in Figure 4.8. For the aperture diameters and positions adapted, the first aperture,  $A_1$ , determines the acceptance angle of the light beam into the interferometer. Aperture  $A_2$  determines the cone angle over which scattered light is collected. The lens  $L_1$  transforms the diverging scattered light beam into a nearly parallel beam incident normally onto the interferometer etalon.

# OPTICAL DETECTION TRAIN



LASER: DEFINING OPTICAL AXIS

SC: SAMPLE CELL

A<sub>1</sub>: VARIABLE APERTURE

A<sub>2</sub>: VARIABLE APERTURE

L<sub>1</sub>: COLLECTION LENS

FP: FABRY PEROT INTERFEROMETER MIRRORS

L<sub>2</sub>: IMAGING LENS

A<sub>3</sub>: PIN HOLE

PMT: PHOTOMULTIPLIER TUBE

I: INCIDENT BEAM FOR SCATTERING EXPERIMENT

P: POLARIZER/ANALYZER OR OTHER APPROPRIATE COMPONENTS

AB<sub>1</sub>: ALUMINUM BOX

AB<sub>2</sub>: INTEROMETER HOUSING

AB<sub>3</sub>: ALUMINUM BOX

CB<sub>1</sub>, CB<sub>2</sub>: CAMERA BELLOWS

A<sub>4</sub>: APERTURE

A<sub>5</sub>: VARIABLE APERTURE

Figure 4.8. Optical Detection Train.

In many experiments (especially Brillouin spectroscopy and depolarization ratio), the nature of the transmitted light beam was altered using various components, identified as P in Figure 4.8, placed into the collimated beam. For example, in a depolarization study, a polarization analyzer was placed here and, of course, the interferometer mirrors were not mounted.

AB<sub>1</sub> is an aluminum box 21-1/4 inches long, 14 inches high and 8-3/8 inches wide. All pieces were 1/2 inch thick except the side walls which were 5/16 inch thick. A 1/2 meter Ealing triangular rail is bolted to the bottom of this box. The bottom plate of the box has wide flanges extending outward allowing it to be bolted into position on the optical table.

Initially, both of the apertures were Ealing precision pinholes mounted onto Ealing microscope objective holders, with centering and focusing. A<sub>1</sub> had a tubular extension placing it closer to the sample. To provide greater mechanical stability an aluminum tube fastened to the aluminum box and extending out close to the sample cell as well as inwards was constructed. On both ends of this tube is a centering mechanism, similar to the Ealing microscope objective holders, holding Edmund variable apertures. The maximum aperture is 15/32 inch and the minimum aperture is 3/64 inch. In addition to mechanical stability, this device greatly improved the convenience of alignment.

Obviously, these two apertures should be placed as far apart as possible.  $A_1$  was 7 cm from the center of the scattering cell and  $A_2$  was placed at 40 cm. With aperture  $A_1$  closed to its minimum, the interferometer's acceptance angle (full cone angle) is about 2 milliradians. As will be discussed later, this is one of the most significant factors limiting the "overall instrumental finesse". With  $A_2$  set near its minimum, the full cone angle of scattered light collected is below 7 milliradians which is very acceptable in terms of scattering angle resolution and is not the limiting factor in minimizing the bandwidth of the instrumental profile.

Lens  $L_1$  is a 50 cm focal length, 6 cm diameter achromat lens. It is mounted in an Ealing lens holder which in turn is mounted on Ealing calibrated carriers for precise transverse motion, both vertical and horizontal. A focusing carrier was not found necessary. This lens was placed 50 cm from the scattering center. The accuracy of this adjustment is not critical; however, the lens' angular orientation relative to the optical axis has significant effects on the instrumental profile. The lens needs to be oriented so that the axis of the transmitted beam is normally incident onto the interferometer.

In a discussion of the collimation of traditional light sources, Coumou (90) implied the need for aperture  $A_4$ . This aperture eliminates edge, diffraction effects





of the first two apertures, especially if the apertures are of the variable type. The size of  $A_4$  is chosen (2 mm dia. when  $A_1$  and  $A_2$  are closed to about 1 mm dia.) so that  $A_4$  does not intercept or significantly diffract the light beam being transmitted but does intercept the spurious beams generated by  $A_1$  and  $A_2$ . This improvement was most significant in some experiments when the sample and sample cell also spuriously scattered light which entered the aperture tube (87).

$CB_1$  is a 3-1/2 by 5-1/2 inch box camera bellow. It is cemented to a metal plate so that it can be bolted to the aluminum box and to the interferometer housing. This enclosure was utilized to prevent the entrance of extraneous light.

### Interferometer Subsystem

#### Interferometer

When this research was initiated, a Lansing Research Corp. model 30.205 resonant cavity interferometer was readily available and it was incorporated into the spectrometer. Plane-parallel mirrors were installed so that this interferometer functioned as a piezoelectrically scanned Fabry-Perot interferometer. The mirror separation is adjustable from 30 cm to 1mm, permitting the choice of an optimal free spectral range for a given experiment. The instrument accepts two inch diameter mirrors and can

easily be adapted for mirrors of small diameter; however, the maximum free aperture is 1.5 inches. The maximum piezoelectric scanning range is 1.2 micron for the application of 0 to -1600 volt allowing three or four complete Brillouin spectra (corresponding to adjacent interferometer modes) to be continuously recorded.

The entire interferometer assembly can be rotated about a horizontal and a vertical axis to align the interferometer perpendicular to the incident light beam. Precise angular orientation of one mirror relative to the other is accomplished via a massive gimbal mount and differential screw translators. This mechanism allows the interferometer's mirrors to be adjusted parallel with an effective resolution of 0.01 seconds of arc. The other mirror is mounted via a piezoelectric transducer to a dovetail rail so that the inter-mirror spacing may be adjusted. The interferometer can be positioned on the spectrometer's optical axis with the aid of adjustable feet. The original teflon feet were replaced with brass feet which also have a lock nut. A pedestal for the interferometer was constructed from two pieces of six-inch aluminum I-beam welded side-by-side. The pedestal was bolted to the optical table and its top surface had kinematic mounting grooves receiving the interferometer's adjustable feet. Tubular extensions were mounted onto the ends of the interferometer housing to provide a more

convenient position (away from the differential screws)  
for a connections to the camera bellows.

### High Voltage Scanner

The pizeoelectric transducer is driven by a Lansing Research Corp. model 80.010 programmable high-voltage power supply. The instruction manual discusses this unit and only its features essential to Brillouin spectroscopy will be outlined here.

The output voltage is a linear ramp (0 to -1.5 kv) with adjustable slopes from 1 to 300 volt/sec. In addition, OSCP, a repetitive, fast sweep mode (20 kv/sec) is available when oscilloscope displays are desired. Oscilloscope displays permit the optimization of experimental parameters while spectra are continuously observerable. The selection of an operating mode is made by means of four push buttons: The SINGLE SWEEP button initiates a single sweep of the high voltage ramp where as the RUN button provides repetitive sweeps. A PAUSE button causes the output voltage to be held constant at whatever value it was at when the button was pushed. The STOP button deactivates the sweep circuits causing the voltage to return to the LOWER LIMIT setting. The portion of the entire ramp voltage which is actually swept over is selected by the adjustment of LOWER LIMIT and UPPER LIMIT controls. These adjustments allow the selection of a portion of the interferometer's frequency span and corresponding recordings of the Brillouin spectra.

A Gate output and TRIGGER input are available for controlling or synchronizing, that is, correlating other experimental functions with the swept high voltage. This is particularly useful for oscilloscopic display of Brillouin spectra during alignment and maintenance. The ramp generator is controlled by logic circuitry (interfaced with the push buttons) and an EXTERNAL PROGRAMMING connection is available for an external signal which may be used to program the high voltage output. However, an external program voltage is added to an internal low voltage sweep to control the high output voltage; a more convenient external control method is discussed in the digital control section. The new external control technique, as well as remote manual control, is made possible by a 7-pin socket which allows remotely located switches to be connected in parallel with the push button controls.

Because of the capacitive load, the first part of the ramp voltage is nonlinear; this nonlinearity may be compensated for by ignoring the initial parts of a recording, or functioning at low sweep rates. The manufacturer specifies the ramp linearity as  $\leq 1\%$  "integral linearity" which corresponds to a recording frequency linearity of  $\leq 15$  MHz when the mirrors are 1 cm apart.

### Mirrors

The performance of a Fabry-Perot interferometer is measured by its finesse. Finesse is related to mirror

parameters by equations (2-32) to (2-37); furthermore, the selection of an optimal set of mirrors is discussed extensively in the literature (48-59).

When helium-neon lasers were being used, the light scattered and collected from samples was relatively low in intensity; therefore, the most severe problem was to simultaneously obtain large  $F_R$ ,  $F_f$  and maximum transmission (58). When the argon ion laser was acquired, intensity disappeared as a dominant factor and it became evident that the acceptance angle, determined by the collection optics, was the factor limiting the instrumental finesse.

The mirrors are of 1-inch diameter and have a  $\lambda/100$  figure of merit. They have a Coherent Optics (catalog number 5.0) broadband coating for which the reflection and absorption are 98.5% and 0.1% respectively for the various wavelengths of the argon ion laser. Ignoring the finesse factors due to mirror alignment and acceptance angle, the mirror specifications indicate a finesse of about 39.8 which is limited by the figure of merit finesse,  $F_f = 50$ . However, experimentally, finesses between 70 and 80 were obtained when a laser beam (low divergence angle and small diameter) was directly incident onto the interferometer. Then, when scattered light was directed onto the interferometer, the maximum obtainable finesse was 40 to 50. This reduction in finesse and acceptance angle considerations for the collection optics indicates that the overall finesse

is limited by the acceptance angle rather than the mirrors. In order to improve the instrument's finesse, the collection optics must first be redesigned as considered in the concluding chapter.

Since the angular resolution of the interferometer alignment mechanism is  $\leq 0.01$  seconds of arc, the mirror tilt is not a serious limiting factor for mirror separations of about 1 cm or less. However, even though the mirrors may be instantaneously aligned sufficiently parallel, an experiment discussed in the next section indicates that the mirrors do not necessarily remain parallel enough for long periods of time. It should be noted that if the mirrors become lossy (dirty),  $F_L$  is reduced and limits the overall finesse.

### Stability

If one considers the equation (2-35) for  $F_\phi$ , it is quite obvious that the adjustment of interferometer mirrors parallel to one another is extremely important relative to the instrument's finesse. Not only is it important to obtain this alignment, in order to be practical, the interferometer's mechanism must maintain it for significant periods of time. During the diagnosis of this instrumental system, the interferometer's stability (or lack of stability) was a frustrating problem. Sometimes the interferometer maintained its alignment over a long work day; sometimes it lost its alignment, significantly

destroying the overall finesse, in a few hours. An experiment illustrating this imperfection and its correlation with room temperature is illustrated in Figure 4.9.

The experiment is related to the alignment technique of the entire instrument. After the interferometer was aligned onto the laser beam defining the spectrometer's detection system's optical axis, the laser beam was attenuated and the photomultiplier output displayed on an oscilloscope. The differential screws were periodically adjusted to maximize the finesse, that is they were adjusted to minimize the width of the peaks displayed on the oscilloscope. The differential screw readings and room temperature were recorded and plotted as a function of time in Figure 4.9. By viewing this graphical representation, it is quite obvious that the alignment instability is correlated with temperature. The manufacturer confirmed the observation that aluminum is used in the construction of this interferometer and some estimations (using thermal coefficient of aluminum) indicate the expansion of several parts may account for this instability.

#### Post-Interferometer Optics

The post-interferometer optics are mounted on an Ealing 1 meter triangular rail inside an aluminum box similar to the AB<sub>1</sub> housing for the collection optics. The



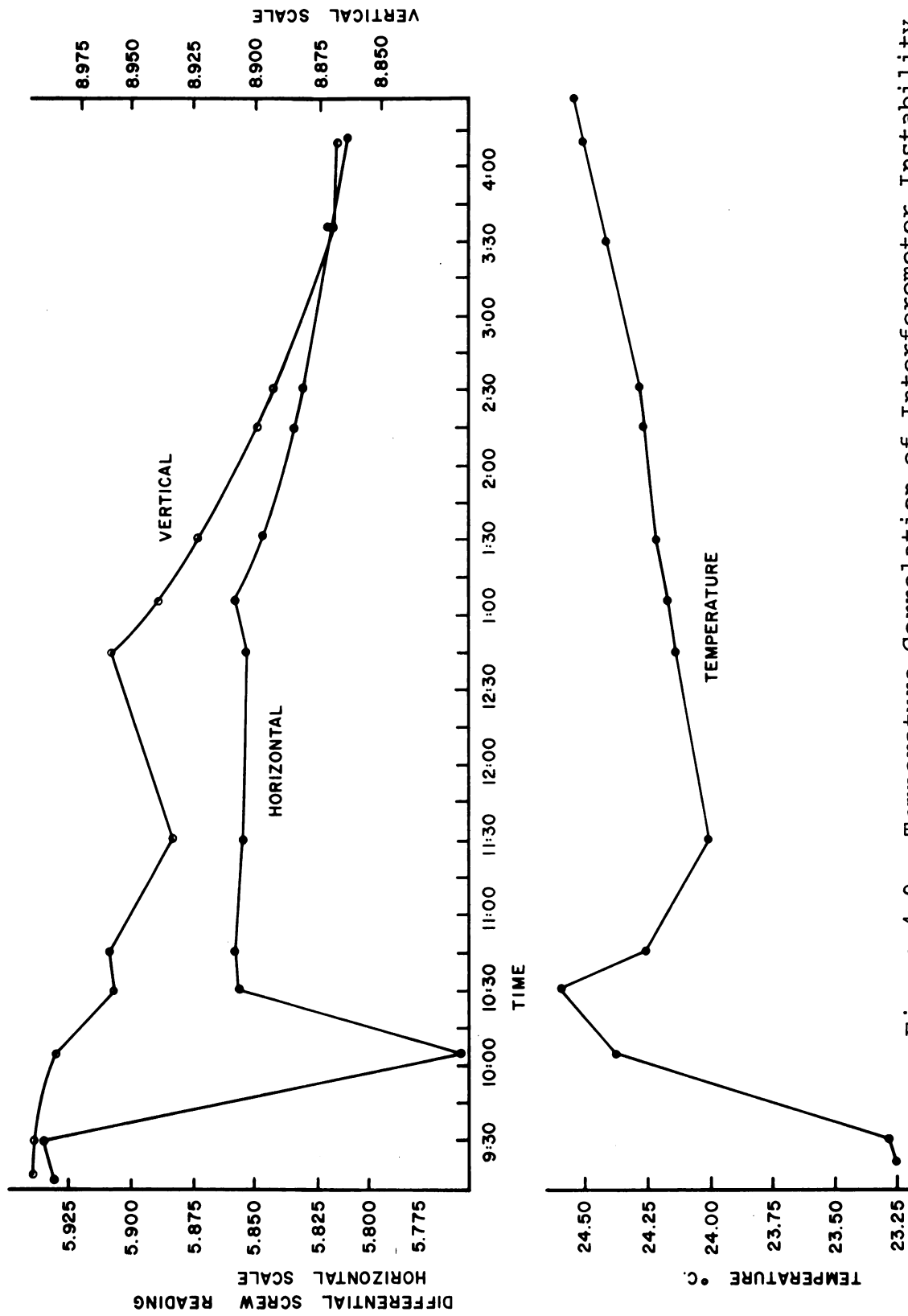


Figure 4.9. Temperature Correlation of Interferometer Instability.

aluminum box  $AB_2$  is 41 inches long, 14 inches high, and 8-3/8 inches wide. Lens  $L_2$  collects the collimated beam exiting from the interferometer and focuses it onto the pinhole  $A_3$ , forming a visible Fabry-Perot ring pattern on the pinhole face or a screen which is often placed there.

Reference to equation (2-40) indicates that, in order to maximize  $\rho_\alpha$  for a given acceptance angle, we need to select the largest feasible  $f_L$ . Hence,  $L_2$  is a 100 cm focal length, 7.1 cm diameter, achromatic lens; with an acceptance angle of 2 milliradians, the pinhole diameter may be increased to 4 mm without diminishing the effective finesse. The pinhole is necessary to block some of the secondary ring patterns due to the wedge shape of the interferometer mirrors; it also reduces the effects of scattering by the interferometer mirrors. Aperature  $A_5$  was found to enhance these two improvements (87). Also, as Met (56) illustrates, when maximum transmission is not required (when scattering is excited with an argon ion laser),  $A_5$  greatly improves the finesse by reducing mirror misalignment effects.  $A_5$  was reduced in diameter until it seriously limited the transmitted intensity. Typically, the diameter is about one centimeter.

Lens  $L_2$  was held by an Ealing self-centering lens holder and was coarsely adjusted in the vertical direction to approximately center the Fabry-Perot ring pattern onto the photomultiplier tube. The photomultiplier pinhole was

mounted in an Ealing centering microscope objective holder so that it could be carefully centered onto the ring pattern.  $A_5$  is a Cenco variable aperture and is only mounted via its rod mount since, having a relatively large diameter, its alignment is not critical.

Similar to  $CB_1$ ,  $CB_2$  is a 3-1/2 X 5-1/2 inch box camera bellows. It is cemented to metal plates, with large axial holes, and bolted to the aluminum box  $AB_2$  and the interferometer housing, reducing the entrance of extraneous light.

### Detection Electronics

#### Introduction

Even though it is broadened by the electron impacts along the dynode chain, the output signal of a photomultiplier tube is a single pulse for each photon incident on the photocathode. (The photomultiplier tube used in this research yields a pulse of 16 nsec duration, 2 mv high across a 50 ohm load resistor.) An output pulse may also arise from thermionic emission of an electron from one of the downstream dynodes; however it will yield a less intense pulse at the anode compared to a pulse of photon initiation. These pulses represent a background or noise signal.

The traditional photometric electronics are characterized by a time constant long compared to the duration of these output pulses; hence, the pulses are

averaged into a dc signal. As an alternative, the intensity of a photon beam may be measured by counting pulses over a fixed period of time with digital equipment. The advantages, disadvantages, and limitations of these direct current and photon counting techniques are being debated in the literature (91-94). One of the more important aspects of photon counting is the improvement in signal-to-noise ratio for low intensity light beams. In photon counting techniques, the noise pulses are of smaller peak height and may be discriminated, i.e. not counted. For these low intensity light beams, direct current measurements average the photon and noise pulses together and the photon component is not easily extracted. When the light beam intensity is increased, the photon counting techniques lose this signal-to-noise ratio advantage because: (1) The noise component becomes insignificant in the direct current measurements. (2) The signal pulses occur much more frequently and overlap each other making it difficult to examine and count individual pulses.

Anticipation of low light intensities for some of the light scattering experiments of interest (especially Brillouin spectroscopy) indicated that photon counting should be incorporated into the instrumental system. However, photon counting was added to the direct current capabilities of this instrumental system primarily for convenience in collecting data digitally and ultimately automating this

instrumental system; the data is naturally of a digital form. Furthermore, it is anticipated that recent and future advances in photomultiplier tube technology and solid state electronics will greatly increase the advantages of photon counting relative to direct current measurements.

#### Photomultiplier Tube, Housing, and Power Supply

The photomultiplier tube is an EMI 9558B tube. It was chosen primarily for two reasons: First, it is often recommended in the spectroscopy literature relative to photon counting as well as analog detection electronics. This literature indicates the tube represents a good compromise between expense and parametric values desired for photon counting. Also, this published data produces a basis for engineering the optimal instrument for a given experiment, using either detection scheme. Second, the red response (S-20 type cathode), coupled with very low dark currents and a  $2 \times 10^6$  gain, make this an extremely useful tube for use with He-Ne lasers without seriously compromising with sensitivities at other wavelengths down to the near ultra-violet wavelengths. The cathode sensitivity is 134  $\mu\text{amp/lumen}$  and the dark currents are diagrammatically presented in Figure 4.10. From these dark current measurements, it is evident that very little is gained by lowering the cathode temperature below  $-20^\circ \text{C}$ ,

a compromise with the manufacturer's specifications:

"extensive investigation reveals that dry ice temperature (ca -60 degrees C) is optimum for best signal to background ratio."

The photomultiplier tube is excited by a power supply in the Lansing Research scanner. This voltage is variable between 0 and -1.8 Kv with  $\pm 0.02$  per cent per hour drift. It is controlled by a ten-turn potentiometer with a clock-type, turns counting dial ensuring easy readability, resolution and resetability. With this continuously variable voltage supply, one may easily find the optimum voltage for a given experiment: a compromise between dark current and sensitivity.

The photomultiplier tube was mounted inside a Products for Research, Inc. model TE-104 TS refrigerated chamber reducing thermionic emissions and corresponding dark currents. Under normal lab conditions, with a coolant water flow rate greater than 10 gph and less than 24° C, this refrigeration unit can maintain the photomultiplier tube's cathode at temperatures down to -20° C (control point continuously variable from -20° C to temperature of coolant water) with a stability of  $\pm 0.5^\circ$  C. The chamber has a mu-metal shield to reduce external magnetic field effects. The tube socket is wired and then potted to prevent water condensation on the dynode resistor chain (220K resistors with a 1N3043B, 150 volt zener diode



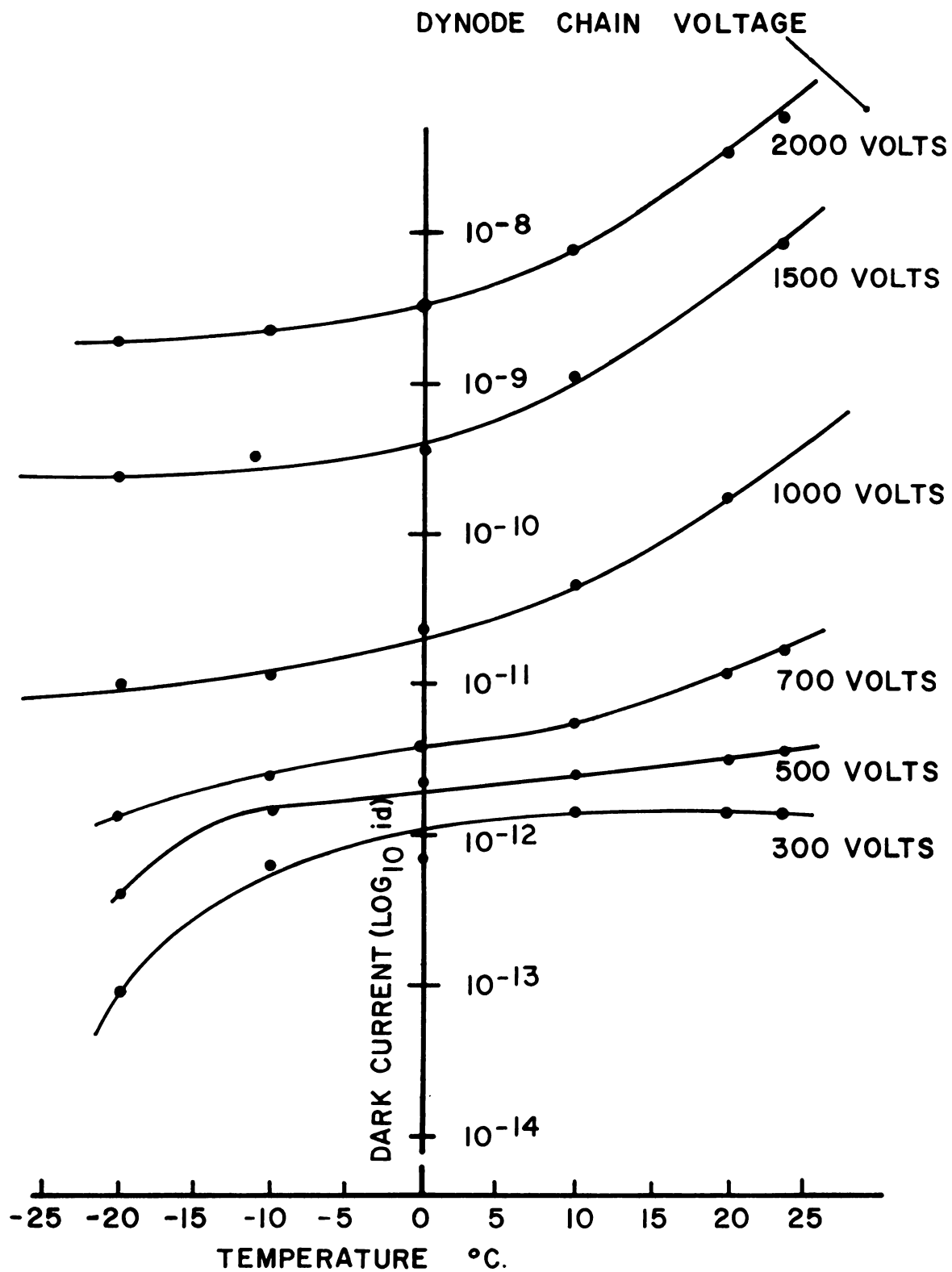


Figure 4.10. Photomultiplier Dark Currents.



between the cathode and first dynode) and the associated leak current problems. The anode is directly connected to its BNC connector without capacitive coupling, making this photomultiplier suitable for photon counting as well as analog detection.

The refrigeration unit was bolted onto the end of box AB<sub>2</sub> with the bolts extending inward so that a disc could be used to cover the photomultiplier tube while alignment was pursued. The room lights were turned off and laser beams blocked while the side of box AB<sub>2</sub> was removed, allowing this disc to be bolted in place to protect the photomultiplier tube. This was quite inconvenient and the instrumental system was modified by inserting a sliding light mask mechanism between the refrigeration unit and box AB<sub>2</sub>. This unit is functionally analogous to, and utilizes a mask from a sheet film holder.

#### Picoammeter

The output current of the photomultiplier is simultaneously fed into a Keithley model 417 picoammeter and the photon counting circuit. The picoammeter has eighteen full scale ranges from  $10^{-13}$  to  $3 \times 10^{-5}$  ampere, well bracketing the range of photomultiplier currents of interest. Normally the rise time is limited by external capacitance (cable capacitance) to 5 millisecc and may be increased to 3 sec with a dampening control. The fast rise time allows oscilloscope display of Brillouin

spectra; slower response times permit "averaging out of noise" for strip chart recordings.

Calibrated suppression currents up to 1000 times the full scale setting are available at the input. In addition to the suppression of a steady background signal, this permits a full scale display of 0.1% variations of the total signal; thus, a weak Brillouin signal is extractable from a relatively large dark current.

The electrometer input tube and solid state amplifier are completely contained within an "input head" unit which may be located remotely; when placed close to the photomultiplier tube, the cable capacitance limitation on the rise time is reduced as well as pick up noise.

### Recorders

The output of the Keithley picoammeter is fed into a strip chart recorder, a digital voltmeter, and an oscilloscope individually or simultaneously. A Sargent model SRG solid state potentiometric strip chart recorder was utilized. The digital voltmeter is a Heath model EU-805A Universal Digital Instrument operating in its digital voltmeter mode and the oscilloscope is a Tektronix, type 564B, model 121N storage oscilloscope. The oscilloscope's horizontal plug-in unit is a type 3B4 time base unit; the vertical plug-in unit is a type 2A63 differential amplifier unit. A Spectra Physics model 420 optical spectrum analyzer



plug-in unit was also employed, particularly for the study of laser beams. The oscilloscope is more useful than the strip chart recorder for aligning the optics for Brillouin spectroscopy and the digital voltmeter is advantageous for the collection of quantitative information in experiments other than Brillouin spectroscopy, especially for measuring the ratio of two very different light intensities.

### Photon Counting

A block diagram of the adopted photon counting system is in Figure 4.11. Malmstadt and Enke (95) provide a good introduction to this subsystem and a bibliography of articles discussing circuitry details is available from Zatzick (96). The principle limitation of digital equipment, that is, the frequency response which increases with increasing expense, is partially alleviated because the amplifier and discriminator units have higher frequency capabilities than the counter. The amplifier and discriminator must deal with the signal and noise pulses whereas the counter only deals with the signal pulses, a significant difference at low light intensities.

The photomultiplier output is fed into an EG&G model AN201/N quad amplifier module via a 50 ohm load resistor. After amplification, the pulses are fed into the EG&G model TD101 differential discriminator module. Both of these digital units have a 100 MHz frequency limit. The

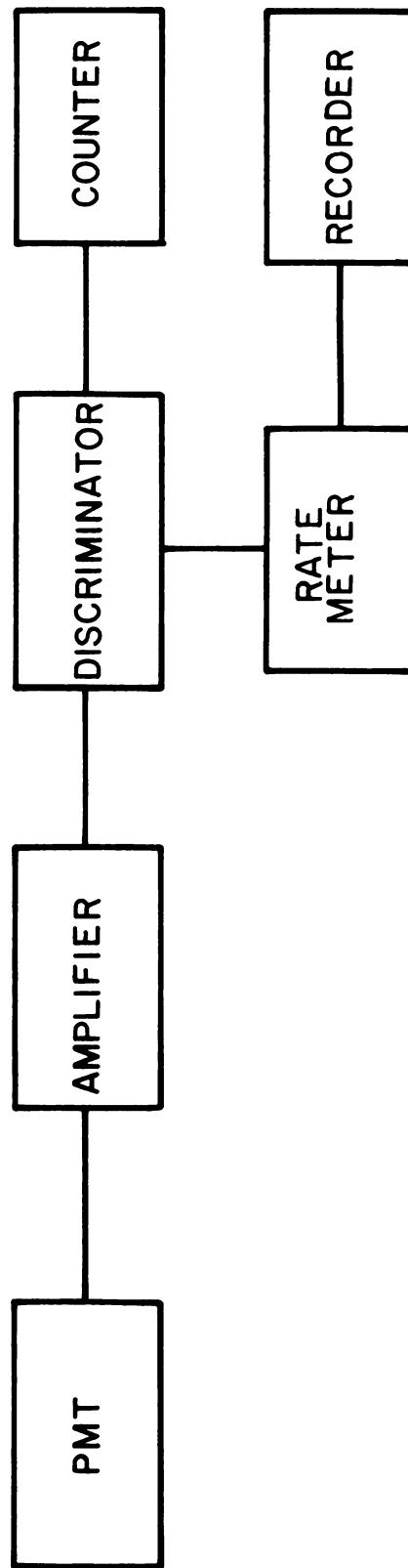


Figure 4.11. Photon Counter.

discriminator output is fed into a Heath universal digital instrument (functioning as a frequency meter or events counter) as well as a count rate meter which provides an analog recorder signal. The count rate meter is the circuit in Figure E7-18, of reference (95), breadboarded on a Heath modular digital system. The counter's frequency limit is 18 MHz.

The behavior of this photon counting subsystem was studied qualitatively by observing the signal at different points with an oscilloscope. The influences of the discriminator level settings, photomultiplier voltage and temperature, etc. on the subsystem's behavior were of the nature expected. However, no quantitative evaluation (especially the determination of the discriminator level setting for an optimal signal-to-noise ratio) was performed. The adoption of the argon ion laser light source and corresponding higher intensities of scattered light which are easily measured by the direct current technique, lessened the importance of the digital technique when low intensity helium neon lasers were employed.

#### Digital Control Unit

One of the ultimate goals of this research was to provide an automated digital system for Brillouin spectroscopy. In order to correlate the intensity measurements (DVM or photon counting) with the interferometer's piezoelectric scan, several different schemes

could be invoked; obviously, a step ramp generator could be employed to control the piezoelectric scanner's output voltage and simultaneously trigger an intensity measurement while the interferometer mirror remains stationary, in a reproducible position. A similar technique, utilizing inexpensive equipment already on hand, which is easily incorporated without compromising the versatility of the piezoelectric scanner became evident and was adopted. It is analogous to cyclically pushing the SINGLE SWEEP button, waiting a constant period of time to push the PAUSE button and taking an intensity measurement.

The serious potential sources of error in manual and adopted digital techniques are: (1) the linearity of the sweep voltage, (2) the constancy of the sweep time period, and (3) a residual drift in the scanner's output voltage during the pause period. (The linearity and scale factor of a spectrum's frequency scale are upset.) The first and third error sources, also present in the normal linear ramp sweep technique, are not significant if the scanner unit is functioning according to its specifications. In the digital technique adopted, the second source of error is avoided by providing an automated button pushing scheme.

The interferometer scanner has a connector providing the opportunity to parallel the RUN, SINGLE SWEEP, PAUSE, and STOP switches at a remote location. Even though the

connector was intended for manual operations, inspection of the switches' circuitry reveals: (1) A positive transition is generated when a switch is closed. (2) A switch's function may be stimulated by the application of an externally generated, positive pulse at this external connector.

The circuit illustrated schematically in Figure 4.12 was "breadboarded" on a Heath model EU-801 modular digital system. The logic of this circuit is illustrated in Figure 4.13. Assuming the interferometer scanner to be in its STOP condition, when the spring return switch PBl is held down long enough, the OR gate provides a logic 1 signal to one side of the AND gate so that when a synchronizing pulse is received from the clock and monostable multivibrator at the other AND gate input, the AND gate outputs a pulse starting the interferometer to scan. Simultaneously the OR gate output pulse causes relay RYI to actuate and connect the operational amplifier output to the other side of the OR gate. When the interferometer sweep begins, a 15 volt gate signal is internally generated in the Lansing Research scanner. This Gate signal, after attenuation and impedance matching, is applied through the relay to the other OR gate input, providing a logic 1 signal to the AND gate as long as the scanner's Gate signal lasts. The Gate signal returns to zero after the interferometer sweep voltage reaches



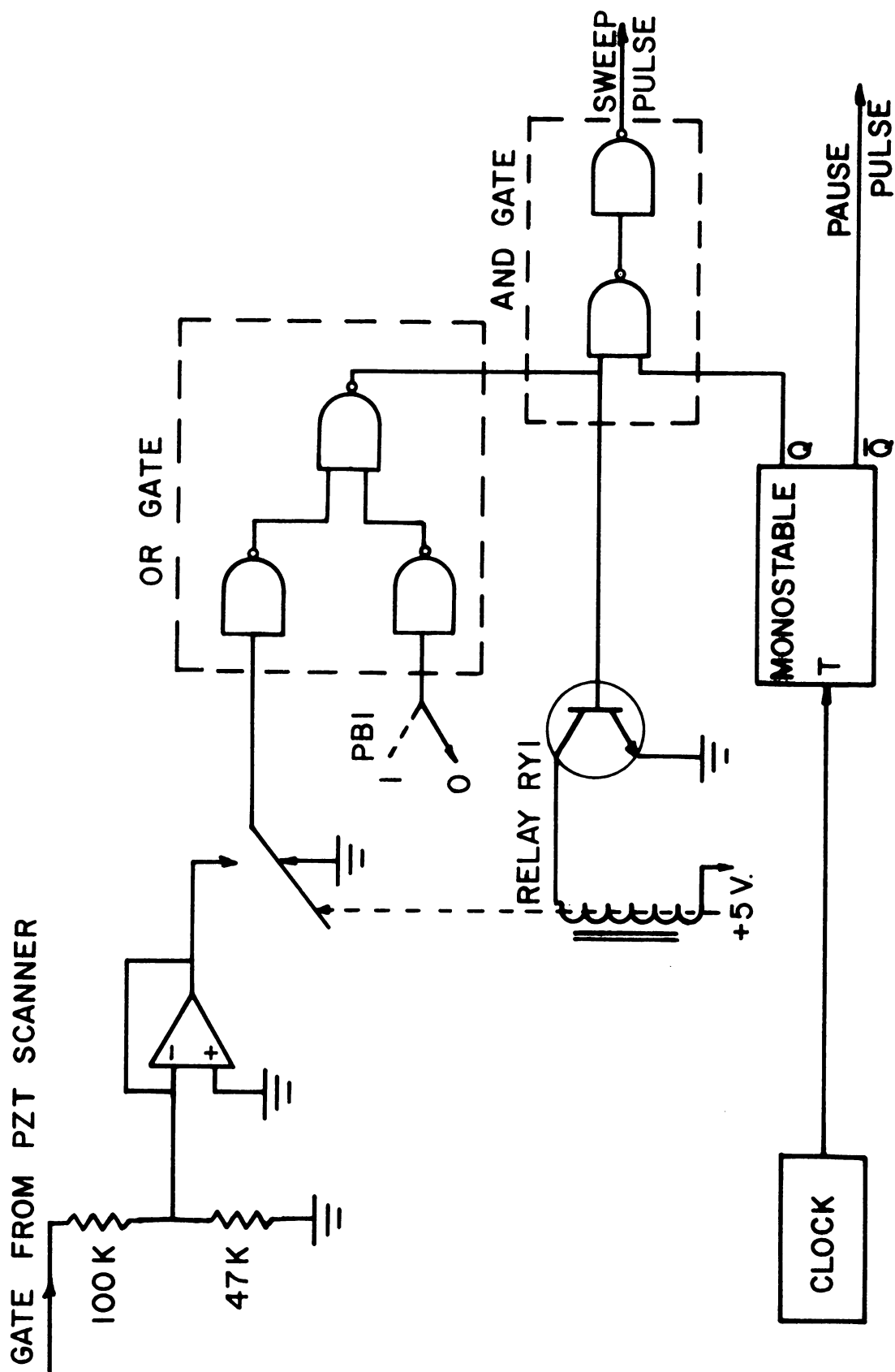


Figure 4.12. Digital Control Unit Circuitry.



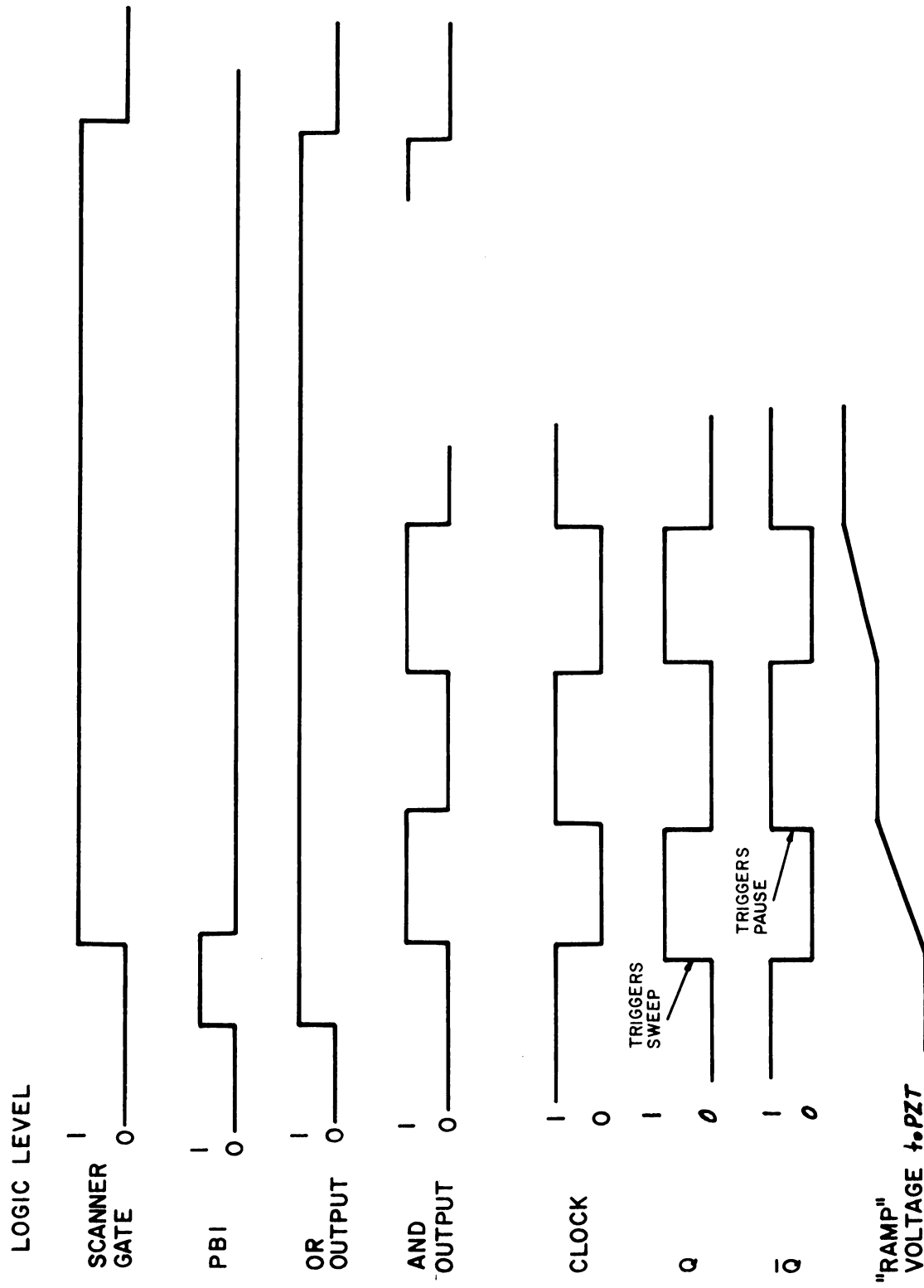


Figure 4.13. Logic of Digital Control Unit.

-1.5 KV, ultimately preventing the AND gate to supply a SWEEP pulse signal to the interferometer scanner until the scanning voltage returns to zero and the PB1 switch is used to restart the system.

After a period of time, adjustable in the monostable multivibrator, the Q pulse being applied to the AND Gate returns to zero. Complementarily, a positive going pulse is generated at  $\bar{Q}$  and is applied to the interferometer's PAUSE switch causing the piezoelectric element to stop scanning. The mirror remains stationary until the clock module generates another negative transition causing Q to go positive and the AND gate to apply a positive transition to the SWEEP switch.

The clock module's output frequency is adjustable from 0.1 Hz to 100 Hz, controlling the frequency of the sweep pulses applied to the interferometer scanner. The monostable multivibrator module may be adjusted so that the duration of the Q (SWEEP) pulse (before  $\bar{Q}$  or PAUSE pulse is applied) is 10  $\mu$ sec to 1 sec. The slope, set on the interferometer scanner, will control the distance which the mirror actually moves for a given Q pulse duration.

If the monostable pulse duration is set to be longer than the input (clock) signal period, the monostable also functions as a frequency divider. This is useful in extending the sweep period beyond the one second limit of

the monostable pulse widths when the input (clock) signal period is longer than the monostable pulse duration.

To summarize, these two pulse width adjustments provide extreme versatility in choosing: (1) the number of pauses (number of data points) during an entire interferometer sweep, (2) the time period of each pause (period of time over which an intensity measurement may be made), and (3) coupled with the slope setting on the interferometer scanner, the distance the mirror moves between pauses.

The voltage applied to the piezoelectric element (after attenuation) was recorded for many different settings of the clock frequency, the monostable pulse widths, and the slope of the interferometer scanner. A portion of one of these recordings is in Figure 4.14. This record corresponds to 10 seconds between SWEEP pulses; the sweep lasts for 4 seconds leaving a 6 second pause period. At these longer pause periods, the light intensity may be measured with a digital voltmeter across the picoammeter's recorder output instead of utilizing photon counting techniques.

The only quantitative check performed on this digital control unit was a measure of the reproducibility of the piezoelectric transducer voltages at the different pause points. The standard deviation of these measurements (made with a DVM) is 0.03% or less, for a slow 3 volt/sec ramp setting and a clock frequency of 10 sec.

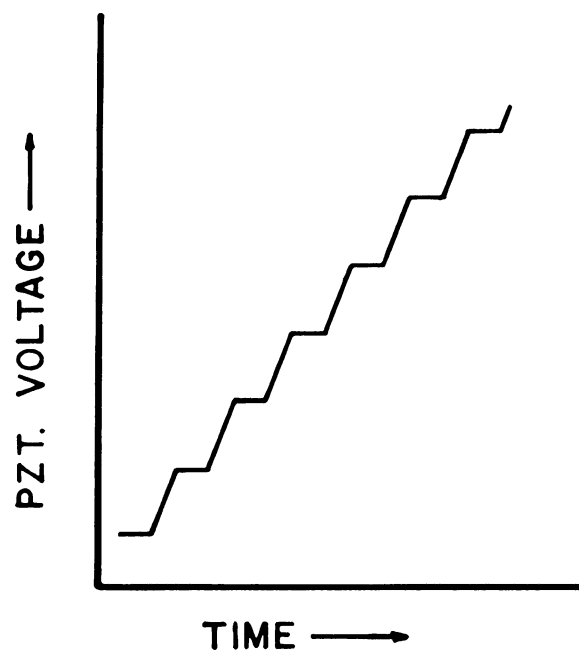


Figure 4.4. Piezoelectric Transducer Voltage when Controlled by Digital Control Unit.

The digital control circuit discussed above corresponds to the interferometer's single sweep mode; however, the circuit is easily extended to include a free run mode and to provide synchronization pulses for photon counting (or DVM) and data "print out".

## CHAPTER V

### ALIGNMENT AND CALIBRATION TECHNIQUES

#### Introduction

In this chapter, the alignment and calibration of the instrumental system from initial assembly to a situation appropriate for Brillouin spectroscopy will be discussed. Brillouin spectroscopy is the most sensitive and illustrative of all these techniques and it is not necessary to repeat them in full for all types of experiments. The exceptions to this extensive routine, for experiments other than Brillouin spectroscopy and repetitive Brillouin spectroscopy experiments, will be self evident.

#### Optical Table Leveling

Three of the axle jacks were lowered slightly, allowing the plane of the table top to be determined by the other three. These latter three jacks were adjusted until the table top was level in both of its horizontal directions as detected by a four foot carpenter level. Then, the levelness was checked by filling a piece of 1/4 inch tygon tubing with water until the water level matched the table top. The tubing went down to the floor, along the floor and up near another corner of the table. When



the table was level, the water level in the tubing at both corners matched the table top.

After leveling was accomplished with these three axle jacks, the other three axle jacks were adjusted to assume a load equal to the three leveling jacks. This equal load was accomplished by using a torque wrench to adjust the latter three axle jacks.

#### Initial Assembly

Before any of the detection optics subsystems were placed onto the optical table, two posts with pinholes 10 inches above the optical table top were mounted at opposite ends of the table. The laser, defining the detection optics axis, was mounted and adjusted so that its beam was centered onto these two pinholes. This insured the optical axis to be horizontal to the optical table top and traveling in a direction (parallel to the optical table's edge) which would allow one to conveniently bolt the subsystem assemblies into place.

The aluminum boxes, with the optical rails inside, were lifted into place and carefully positioned so that when a pinhole (centered on a vertical post) was slid along the triangular rail it remained centered on the laser axis beam. This adjustment insures that translations along the rail will be the same as translations along the detection optics axis, facilitating alignment of the individual components mounted on the rail. The aluminum boxes were then bolted into place.

The interferometer housing, resting on its I-beam pedestal, was set into place. The interferometer's differential screws and axis adjustors were set at their midpoint. Two adaptors were inserted into the interferometer housing's two-inch entrance and exit holes providing axial, 2 mm dia centering apertures. The interferometer's pedestal and legs were adjusted so that the optical axis laser beam was centered onto these two apertures. Then the interferometer's position was checked, and readjusted so that when a mounted mirror was slid along the interferometer's dovetail rail, the incident beam was always reflected back onto itself. This makes the dovetail rail parallel to the system's optical axis and insures the interferometer will always be adjustable, regardless of its mirror spacing. The I-beam pedestal was then bolted into place, and the interferometer's leg lock nuts were set.

The rotating table assembly was lifted into place and adjusted (see the section on the variable scattering angle mechanism) so that its rotating axis intersected the optical axis. To facilitate this alignment, a vertical pin point adaptor was mounted onto the rotary table. Assuming a cylindrical sample cell, this insures that the collection optics, when aligned appropriately, will always view the same scattering volume element, irrespective of the table's rotatory position, (angle of incidence or scattering angle).

Next, the rotatory table was set at its zero angle position and the pinhole mechanisms were adjusted so that the pinholes were centered on the laser beam. This adjustment insures the pinholes to be on a diameter of the rotatory table and at a height corresponding to the volume element viewed by the detection optics. Now, when the table is rotated through an angle, readable from the table's mechanism, and the incident laser beam (whose scattering is to be studied) is directed through these two pinholes, the scattering angle is known and the scattering volume element is centered appropriately.

#### Collection Optics Alignment

The apertures  $A_1$  and  $A_2$ , set at their minimum diameters were centered onto the laser beam which defines the optical axis. Lens  $L_1$  was placed 50 cm from the center of the rotating table and positioned so that the transmitted beam was undeviated relative to the incident optical axis beam when viewed on a screen near the photomultiplier tube. An additional criterion for the positioning of  $L_1$  was the beam reflected from its first surface. The lens was adjusted until the incident beam was reflected back onto itself. The backside of apertures  $A_1$  and  $A_2$  as well as the laser's exit port are convenient viewing points for this criterion.

It is not necessary, but the 50 cm (lens focal length) distance can be checked by focusing the laser beam

to a point at the rotary table's center and examining the light beam transmitted through  $L_1$  for collimation, i.e., constant diameter.

The alignment of aperture  $A_4$  is not critical. Its diameter is larger than the diameter of the laser beam coming through  $A_1$  and  $A_2$ . It is only important that  $A_4$  is adjusted so that it does not block part of this beam.

#### Interferometer Alignment

The interferometer mirrors are mounted into their holders; the mirror closest to the photomultiplier tube is slid along the dovetail rail and locked into place at the desired mirror spacing. Several scratches have been made on this rail to facilitate approximate setting of the mirror spacing. The accurate measurement of the mirror spacing will be discussed in the interferometer calibration section. It should be recalled that the mirrors, for ultimate frequency resolution, are spaced as close together as possible without serious overlapping of the spectra associated with adjacent interferometer modes. The interferometer's fringe pattern may be viewed on a screen anywhere on the axis behind the interferometer or, as the author prefers, on the ceiling after reflection by a mirror propped up by the back of the interferometer housing.

Initially, one observes a train of bright spots corresponding to multiple reflections of the laser beam.

This train of spots is collapsed into one spot, or a ring pattern, by adjusting the gimbal mount's differential screws. The upper differential screw rotates the gimbal mount about a horizontal axis and the lower differential screw rotates the gimbal mount about a vertical axis. Now, if the interferometer is scanned, the various rings will sequentially collapse to a bright spot. Another dim spot, corresponding to the direct passage of the incident beam through the interferometer mirrors, is visible. These two spots are not coincident because the wedge shape of the first mirror perturbs the normal incidence of the laser beam. The adjustments on the interferometer's housing are varied until the ring pattern collapses onto the leakage spot. The differential screws are adjusted to give a sharp, well defined set of fringes.

These two sets of adjustments are not independent, or orthogonal, because of the interferometer's mechanical design and the mirror's wedge shape. Thus, one must systematically repeat these adjustments until the sharpest ring pattern which collapses onto the leakage spot is obtained. The differential screws primarily control the parallelness of the reflecting surfaces and hence, the definition of the ring pattern. The housing adjustments primarily control the angle of incidence, hence the relative position of the leakage spot and the center of the fringe pattern.

The final alignment of the interferometer is obtained, after lens  $L_2$  and the photomultiplier pinhole are aligned, by viewing an oscilloscope display of the photomultiplier, picoammeter output. The criteria are: (1) narrowest linewidth, and (2) symmetry of the peak; these factors are primarily related to, (1) the mirror parallelness, and (2) normal incidence onto the reflecting surfaces. The axis of the cone of incident radiation is also affected by the alignment of the collection optics and their alignment should now be rechecked.

Finally, it is noted that no serious problem arises from the fact that the alignment laser is usually a helium-neon laser and the laser for Brillouin scattering experiments is usually an argon ion laser. The interferometer mirrors are broad band and have sufficient reflectivity at  $6328 \text{ \AA}$  to yield a finesse adequate for alignment.

#### Post-Interferometer Optics Alignment

The placement of lens  $L_2$  is not critical.  $L_2$  is adjusted to cast the center of the fringe pattern within the range of adjustability of the photomultiplier pinhole. The photomultiplier pinhole was set at a 1 mm diameter while its mounting mechanism was adjusted to center it onto the fringe pattern. Then this pinhole was enlarged to a 4 mm diameter. When set at smaller diameters, the

symmetry of the spectra peaks are strongly dependent upon this pinhole's alignment. However, this is relieved (also increasing transmitted intensity) at larger pinhole diameters; and, we may do so without reducing the instrumental finesse (see the section discussing the post-interferometer optics).

Aperture  $A_5$  is minimized and aligned onto the leakage beam or center of the fringe pattern.  $A_5$  is opened to a diameter of about 1 cm; hence, its alignment is not critical. The optimum diameter is normally associated with a compromise in instrumental finesse and transmitted intensity (56). However, in this instrumental system, with high sensitivity of the detection electronics and inherent properties of the collection optics and interferometer, this compromise is not a strong function of either of these two factors.

#### Incident Laser Beam Alignment

The mechanism for aligning the incident laser beam has already been discussed. The Bridgeport rotary table is rotated to the desired scattering angle and the incident laser beam's direction is adjusted by translating, rotating, and tilting the mirror in the incident optics until the laser beam is centered onto the two (sample cell) alignment pinholes. Two things will facilitate these scattering angle adjustments: (1) The laser's mounts, presently lab jacks, are adjusted in order that the laser beam is parallel

to the optical table, 10 inches above it. (2) The laser is positioned so that its beam is also parallel to the rail in the incident optics system. The alignment or calibration of the laser's polarization is very important and is discussed in a following section.

#### Sample Cell Positioning

The glass cell containing the sample of interest is set onto the copper base plate and pressed hard enough to squeeze out excessive amounts of the thermal compound. Then the cell is slid (rotated, etc.) on this base until the cell's surface reflections cause both the optical axis laser and the incident light beams (for the scattering studies) to traverse back upon themselves. For a square cell, this criterion is sufficient; however, a further check may be performed by rotating the table in  $90^\circ$  intervals and observing the surface reflections. When cylindrical sample cells are used, and measurements are made as a function of the scattering angle, it is important that the sample cell be coaxial with the rotating table. This may be investigated by examining the reflected and transmitted light beams for constancy of their character as the table is rotated. A cylindrical cell's position, etc. can also be checked by an experiment discussed in the section, "Angular Dependence of Light Scattering".

The vertical position of the scattering volume can be checked visually; if the sample is illuminated by both



light beams, they should intersect. Also, when the high intensity argon ion laser is used to excite the scattering, the scattering volume element may be visually inspected at any point along the detection optics axis. This technique is especially useful if a Ludox solution is used to examine the incident beam's alignment and is replaced later by the sample of interest. However, an ultimate criterion for the directional adjustments of the incident laser beam is the narrowness and symmetry of the Rayleigh peak as displayed on an oscilloscope, or ultimately on a recording of the scattered light spectra.

Finally, for optimum performance, all of the aperture, lens, and especially, the interferometer adjustments should be optimized again by viewing a spectra displayed on the oscilloscope. After the thermostating unit is lowered into place and thermal equilibrium is obtained, these adjustments should be optimized again before a spectrum is recorded.

#### Interferometer Calibration

Many different, complex calibration techniques have been devised for Fabry-Perot interferometers (see Fabelinskii (97) for a summary); however, they are based on the need for an absolute frequency calibration. In Brillouin spectroscopy, we are only interested in frequency differences and only need to know the interferometer's free

spectral range. When a Brillouin spectrum is recorded, at least two adjacent mode spectra are recorded. The distance between corresponding peaks is equal to the interferometer's free spectral range. Thus, since the scanning is linear, one only needs to know the free spectral range in order to determine the frequency scale of a recording.

The free spectral range of the interferometer is determined by its mirror spacing, Table 2.1; hence, we only need to measure the mirror separation accurately in order to calibrate our frequency scale. This may be accomplished by using telescoping gauges, set to match mirror spacing and measuring the gauge's length with a micrometer. If done in the reverse order, the mirrors may be set at a known, convenient separation. These micrometer measurements may conveniently be made with  $\pm 0.1$  mil accuracy and precision; this corresponds to a 3.8 MHz uncertainty in the free spectral range (15 GHz) for a mirror spacing of 1 cm. If the spectrum is recorded with a slow interferometer scan, fast recorder speed, the uncertainty in the spectrum's frequency parameters is reduced to an insignificant value.

At this point it is convenient to state that no calibration of the intensity scale was undertaken. For Brillouin spectroscopy, or any of the photometric type of experiments done herein, only relative intensity measurements are necessary.

### Temperature Calibration

A rather convenient method of temperature calibration was investigated as a project tangential to this thesis work. As a natural consequence of that project a more rigorous fixed point cell calibration of a platinum resistance thermometer is available.

This fixed point method of calibration is well documented, for example see Shoemaker and Garland (98). The fixed point cells for the phenol freezing point, naphthalene freezing point and phthalic anhydride freezing point were used for additional data points in the temperature range of interest. These cells are discussed by Enagonio, et al. (99).

An Electro Science Inc. portable potentiometer-bridge and platinum resistance thermometry accessories were used to measure the relative resistance of a platinum resistance thermometer at these fixed temperatures. The method is discussed in the instruction manual and was modified only to the extent of externally using a Keithley model 155 null detector meter. This meter made the meter interpolation for additional digits in the data easier and more precise.

The data was analyzed with least square mathematics and the results are in Table 5.1. A chart of  $R_t/R_0$  versus temperature is retained in the laboratory.

TABLE 5.1.--Platinum Resistance Thermometer Calibration.

Fixed Point	R' (exptl.)	t (std, °C)	t(calc.)
Mercury Freezing Point	0.84690±0.00028	-38.862	-38.884
Water Freezing Point	1.00000±0.00003	0.000	0.001
Sodium Sulfate Transition	1.12595±0.00021	32.382	32.390
Phenol Freezing Point	1.15859±0.00006	40.849	40.844
Naphthalene Freezing Point	1.30943±0.00013	80.239	80.247
Corrected Water Boiling Point	1.38430±0.00042	100.000	100.013
Benzoic Acid Freezing Point	1.46836±0.00003	122.375	122.375
Pthalic Anhydride Freezing Point	1.50075±0.00026	131.059	131.041

Equation:  $R' = R_0 + \alpha t + \beta t^2$

Least Square

Parameters:  $R_0 = 0.99999661 \pm 8.005 \times 10^{-6}$

$$\alpha = 3.91077781 \times 10^{-3} \pm 5.522 \times 10^{-7}$$

$$\beta = -6.82273637 \times 10^{-7} \pm 4.318 \times 10^{-9}$$

RMS Error in t:  $3.147 \times 10^{-3}$

## Polarization Alignment and Calibration

### Introduction

Light scattering experiments are sensitive to the polarization alignment of the incident light beam (assuming a polarized beam as is common in lasers) and the calibration of polarization filters or analyzers in the viewing optics relative to the incident beam's polarization. In principle, one may initiate polarization alignment and calibration with a light source of known polarization vector or an optical device whose optical axis or polarizing effects are known. In many of the classical optical experiments, for example polarimetry, only changes in polarization are measured and most of the polarization calibration devices are of the latter type, defining a relative system. However, in many light scattering experiments this relative technique is not sufficient. This is especially evident when one considers studying the character of a scattered light beam as a function of viewing angle with a polarized incident beam. Furthermore, in this versatile experimental system, it is convenient to align or calibrate in a polarization coordinate system synonymous with the laboratory coordinate system. Thus, the other subsystems, such as the sample cell, are independently aligned in the same coordinate system.

In his depolarization studies, Anderson (82) aligned the laser's polarization vector relative to the laboratory

coordinate system and then aligned or calibrated other parts using this light beam of known polarization. His technique was based on the reflections from the Brewster window of the laser's plasma tube. It was convenient to open the laser, allowing the reflections to cast onto the ceiling. It was also convenient to rotate the plasma tube. Neither of these procedures are possible with most lasers. Even though one could rotate the entire laser unit, the polarization alignment and calibration of this instrumental system was accomplished by rotating the laser beam's polarization vector until it was vertical or horizontal using a half wave plate. Polarization analyzers, etc. were orientated for maxima or minima transmission of this polarization aligned beam. The criterion for the laser beam's polarization being vertical or horizontal is based on Brewster angle reflection from a glass plate external to the laser.

### Theoretical Discussion

Consider a laser beam whose polarization vector is rotated  $\alpha$  radians counterclockwise from the vertical  $x$  axis, is traveling in the  $z$  direction (Figure 5.1), and is incident upon a glass plate whose plane of incidence is coincident with the  $xz$  plane. The reflectivities of the two polarization components are different and a function of the angle of incidence. For example, the component parallel to the incident plane has zero reflectivity for

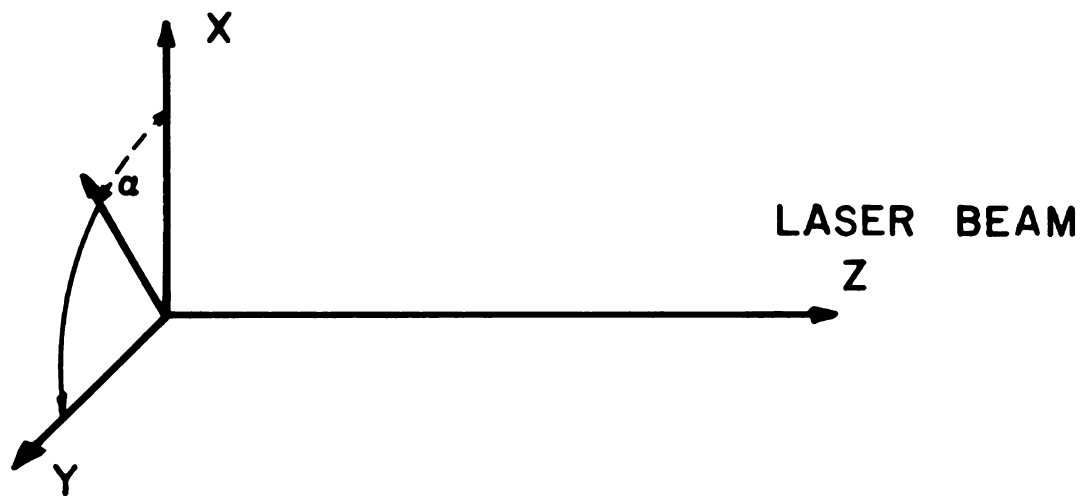


Figure 5.1. Coordinate System for Discussion of Polarization Alignment Technique.

the Brewster incidence angle whereas the component perpendicular to this plane is finite. Thus, when the polarization vector is rotated until it is parallel with the incident plane, or equivalently, until it becomes vertical, the intensity of the reflected light goes through a minimum.

Qualitatively, the incidence angle dependence of these two reflectivities are illustrated in Figure 5.2. At most angles, such as  $\theta_1$ , the reflectivity of the parallel component is less than that of the perpendicular component. The polarization vector of any incident light beam may be decomposed into parallel and perpendicular components. Since the reflectivity of the perpendicular component is favored as  $\alpha$  approaches zero, the total reflected intensity should go through a minimum at  $\alpha$  equal to zero. Similarly, the total reflected intensity passes through a maximum value when  $\alpha$  equals 90 degrees.

The beam incident onto the glass plate may be given by:

$$I_{in} = R_0 I_s \quad (5-1)$$

where  $I_s$  is the Stokes vector for a laser beam propagating in the  $z$  direction of the coordinate system in Figure 5.1.  $R_0$  is a rotation matrix;  $I_{in}$  is the stokes vector for the incident beam whose polarization vector is rotated by  $\alpha$  from the vertical.  $R_0$  is given by:



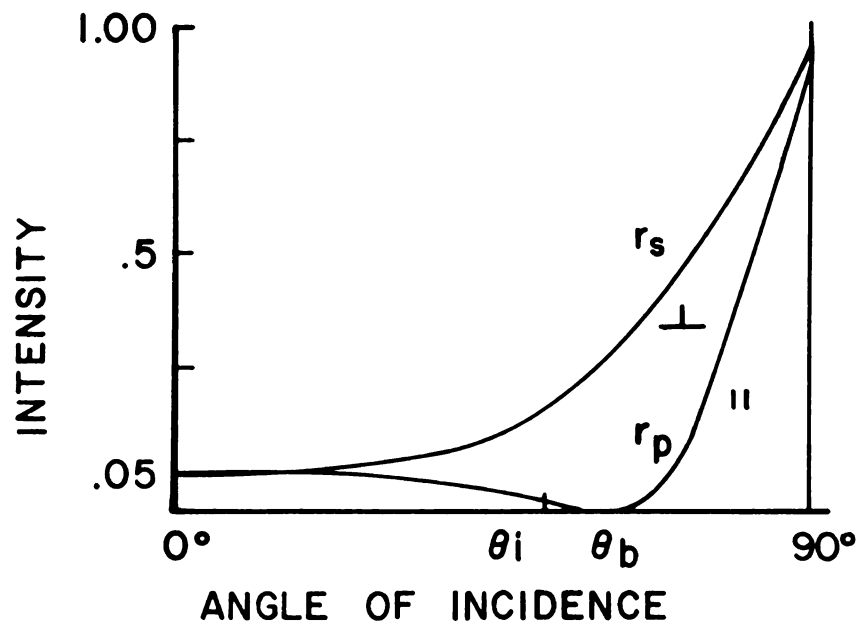


Figure 5.2. Reflectances of a Dielectric.

$$R_o = \begin{bmatrix} 1 & 0 & 0 & 0 \\ 0 & \cos 2\alpha & -\sin 2\alpha & 0 \\ 0 & \sin 2\alpha & \cos 2\alpha & 0 \\ 0 & 0 & 0 & 1 \end{bmatrix} \quad (5-2)$$

If  $I_s$  is given by:

$$I_s = \begin{bmatrix} 1 \\ 1 \\ 0 \\ 0 \end{bmatrix} \quad (5-3)$$

then

$$I_{in} = \begin{bmatrix} 1 \\ \cos 2\alpha \\ \sin 2\alpha \\ 0 \end{bmatrix} \quad (5-4)$$

In the Mueller Jones system, reflection may be represented, via Fresnel's law, by:

$$R'_F = \begin{bmatrix} t & 0 \\ 0 & s \end{bmatrix} \quad (5-5)$$

wherein:

$$s \equiv \frac{\sin (\theta - \theta')}{\sin (\theta + \theta')} \quad (5-6)$$

$$t \equiv \frac{\tan (\theta - \theta')}{\tan (\theta + \theta')} \quad (5-7)$$

The incidence angle,  $\theta$ , is related to the refraction angle,  $\theta'$ , by Snell's law:

$$\sin \theta = n \sin \theta' \quad (5-8)$$

$n$  being the refractive index of the glass plate. In order to convert  $\mathbf{R}'_F$  into the Stokes system one uses:

$$\mathbf{R}_F = \Pi (\mathbf{R}'_F \times \mathbf{R}'_F^*) \Pi^{-1} \quad (5-9)$$

and the unitary matrix  $\Pi$  is given by:

$$\Pi = \frac{1}{\sqrt{2}} \begin{bmatrix} 1 & 0 & 0 & 1 \\ 1 & 0 & 0 & -1 \\ 0 & 1 & 1 & 0 \\ 0 & -i & i & 0 \end{bmatrix} \quad (5-10)$$

The result is

$$\mathbf{R}_F = \frac{1}{2} \begin{bmatrix} s^2+t^2 & t^2-s^2 & 0 & 0 \\ t^2-s^2 & s^2+t^2 & 0 & 0 \\ 0 & 0 & 2st & 0 \\ 0 & 0 & 0 & 2st \end{bmatrix} \quad (5-11)$$

$$\text{Now, if} \quad S \equiv s^2 \quad (5-12)$$

$$\text{and} \quad Q \equiv t/s = \frac{\cos (\theta + \theta')}{\cos (\theta - \theta')} \quad (5-13)$$

then

$$\mathbf{R}_F = S \begin{bmatrix} \frac{1+Q^2}{2} & \frac{Q^2-1}{2} & 0 & 0 \\ \frac{Q^2-1}{2} & \frac{1+Q^2}{2} & 0 & 0 \\ 0 & 0 & Q & 0 \\ 0 & 0 & 0 & Q \end{bmatrix} \quad (5-14)$$

If the reflected beam is represented by a Stokes vector,  $\mathbf{l}_{out}$ , then:

$$\mathbf{l}_{out} = \mathbf{R}_F \mathbf{l}_{in} \quad (5-15)$$

and

$$\mathbf{l}_{out} = \frac{S}{2} \begin{bmatrix} (1 - \cos 2\alpha) + Q^2(1 + \cos 2\alpha) \\ (1 - \cos 2\alpha) + Q^2(1 + \cos 2\alpha) \\ 2Q \sin 2\alpha \\ 0 \end{bmatrix} \quad (5-16)$$

The total reflected intensity, the first element in the Stokes vector, is:

$$I = \frac{S}{2} \left[ (1 - \cos 2\alpha) + Q^2(1 + \cos 2\alpha) \right] \quad (5-17)$$

thus,

$$\frac{\partial I}{\partial \alpha} = -S(Q^2 - 1) \sin 2\alpha \quad (5-18)$$

In order that a minimax point occur,  $S$ ,  $Q^2-1$ , and/or  $\sin 2\alpha$  must be zero. First,

$$\sin 2\alpha = 0 \quad (5-19)$$

implies:

$$\alpha = 0, \pi, \dots \quad \text{for minima}$$

and  $\alpha = \frac{\pi}{2}, \frac{3\pi}{2}, \dots$  for maxima

Using back substitution and the physical restriction,

$$-\frac{\pi}{2} \leq \alpha \leq \frac{\pi}{2}, \text{ we see that } I \text{ is a minimum only when } \alpha=0.$$

The requirement on S:

$$S = \left[ \frac{\sin (\theta - \theta')}{\sin (\theta + \theta')} \right]^2 = 0 \quad (5-20)$$

leads to

$$\sin (\theta - \theta') = 0 \quad (5-21)$$

provided  $\sin (\theta + \theta') \neq 0$ . Equation (5-21) implies:

$$\theta - \theta' = 0, \pi, 2\pi, \dots$$

However, since  $\theta'$  is given by  $\sin \theta = n \sin \theta'$ , only

$\theta = \theta' = 0$  (normal incidence) is possible. Finally, for

the  $Q^2-1$  factor, we obtain:

$$\left[ \frac{\cos (\theta + \theta')}{\cos (\theta - \theta')} \right]^2 = 1 \quad (5-22)$$

or

$$\cos (\theta + \theta') = \pm \cos (\theta - \theta') \quad (5-23)$$

Using trigonometry, this equation rearranges to:

$$\cos \theta \cos \theta' - \sin \theta \sin \theta' = \pm (\cos \theta \cos \theta' + \sin \theta \sin \theta')$$

For the plus and minus signs, this expression converts into the two expressions,

$$\sin \theta \sin \theta' = 0 \quad (5-25)$$

$$\cos \theta \cos \theta' = 0 \quad (5-26)$$

requiring  $\theta=0$  (normal incidence) or  $\theta=\frac{\pi}{2}$  (glazing incidence). However, for these values of  $\theta$ , the reflectances are the same for the parallel and perpendicular components; that is, the total intensity will remain constant (at  $\left(\frac{n-1}{n+1}\right)^2$  and 1 for  $\theta=0$  and  $\pm \frac{\pi}{2}$  respectively) as  $\alpha$  is changed. Therefore, after considering all three factors of equation (5-18), we see that the only case for a minimum in the intensity of the reflected beam is  $\alpha=0$ , a vertically polarized beam.

Setting the partial derivative of  $I$  with respect to  $\theta$  equal to zero leads to  $\theta=0$  and  $\pm \frac{\pi}{2}$ . These cases have already been disregarded in the arguments above. The existence of a minimum reflected intensity, with respect to variations in  $\alpha$ , is independent of  $\theta$ , but, perhaps the minimum's quality or sharpness is dependent upon  $\theta$ . In



order to examine the quality aspect of these minima, we only need to consider small values of  $\alpha$ . For these small values of  $\alpha$ , we may use the truncated series expression:

$$\cos 2\alpha \approx 1 - \frac{1}{2} (2\alpha)^2 + . . .$$

and transform equation (5-17) into a quadratic function of  $\alpha$ :

$$I = SQ^2 - B\alpha^2 \quad (5-27)$$

wherein

$$B \equiv S(1-Q^2) \quad (5-28)$$

It is not easy to analytically determine the value of  $\theta$  which maximizes the sensitivity of  $I$  to  $\alpha$ . However, it is easy to see that  $B = s^2 - t^2$  and that  $I$  will be most sensitive to  $\alpha$  when  $s^2 - t^2$  is maximum. Furthermore,  $s^2 = r_s$  and  $t^2 = r_p$ , so that (1) acknowledging  $r_s$  and  $r_p$  are the perpendicular and parallel reflectivities and that (2)  $I$  is a linear combination of these reflectances, it is qualitatively reasonable that  $I$  would be most sensitive to  $\alpha$  when their difference is maximum.

The values of  $\theta$  maximizing  $r_s - r_p$  were determined numerically by the computer program POLCAL and are plotted in Figure 5.3 as a function of the refractive index of the glass plate. Figure 5.4 illustrates  $r_s - r_p$  versus angle of incidence for a given refractive index,  $n = 1.50$ . Figure 5.5 illustrates the Brewster angle as a function of refractive index. Following the definitions for these



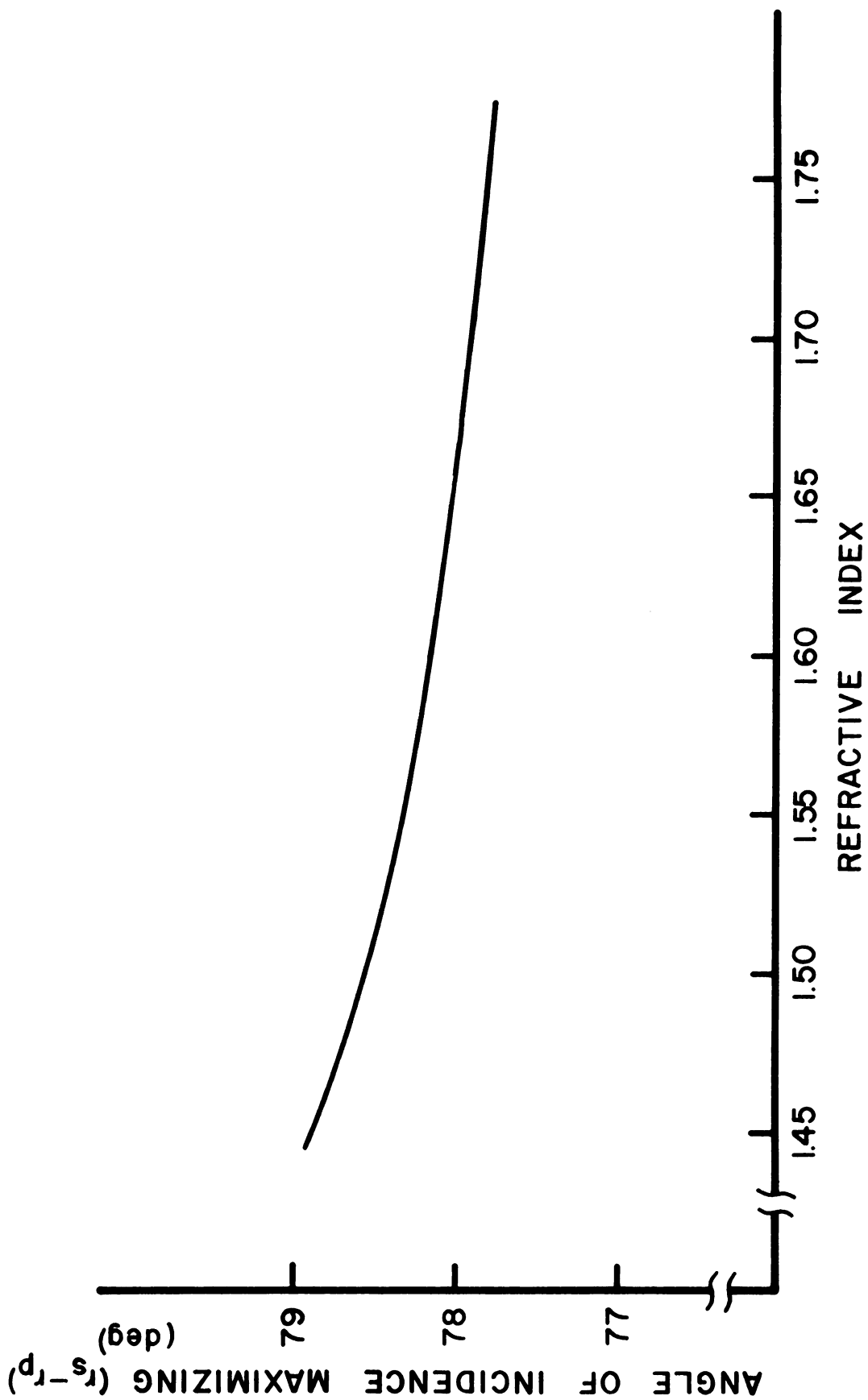


Figure 5.3. Refractive Index Dependence of Incidence Angle Maximizing  $r_s - r_p$ .



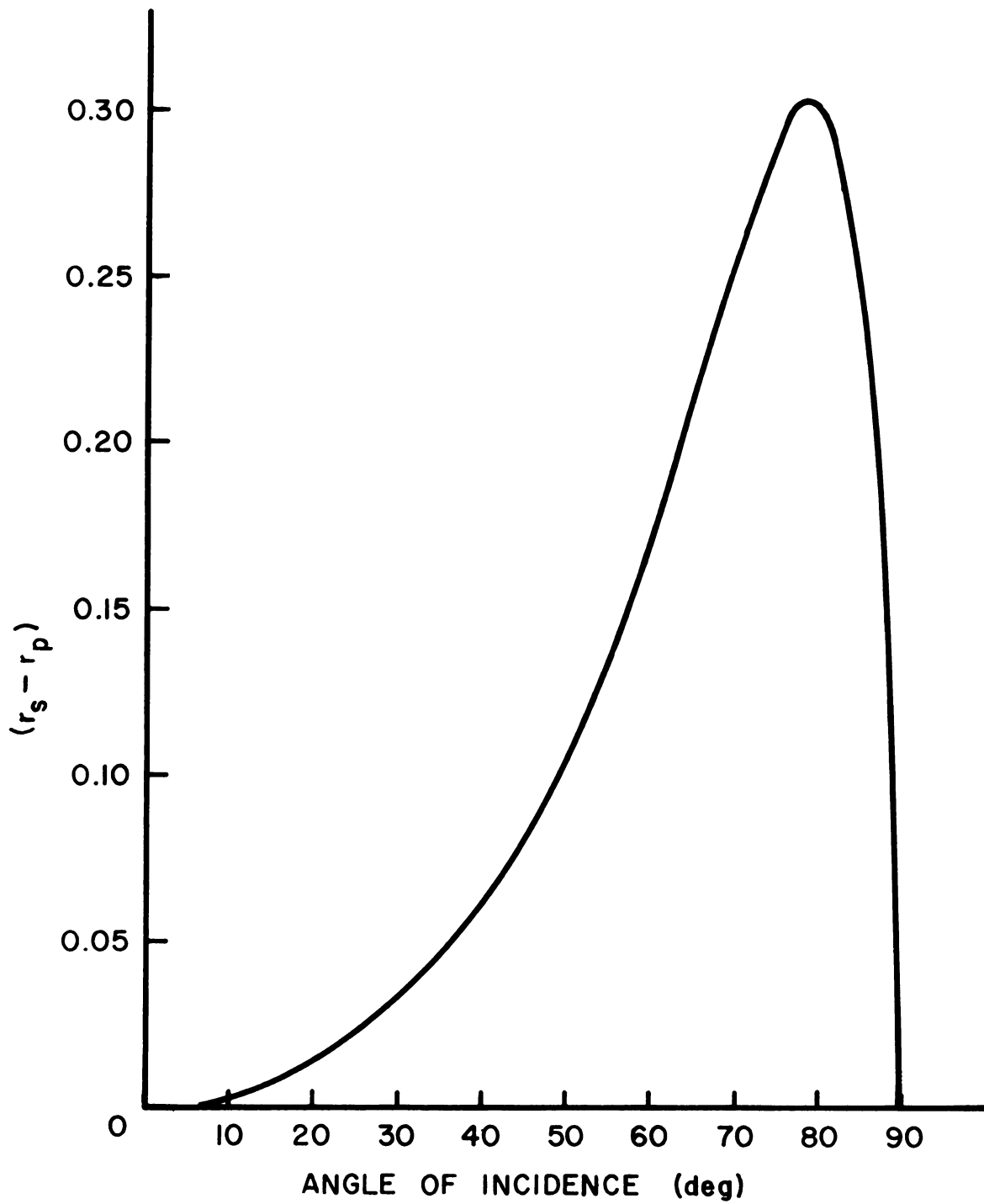


Figure 5.4.  $r_s - r_p$  Dependence on Angle of Incidence for a Refractive Index of 1.50.



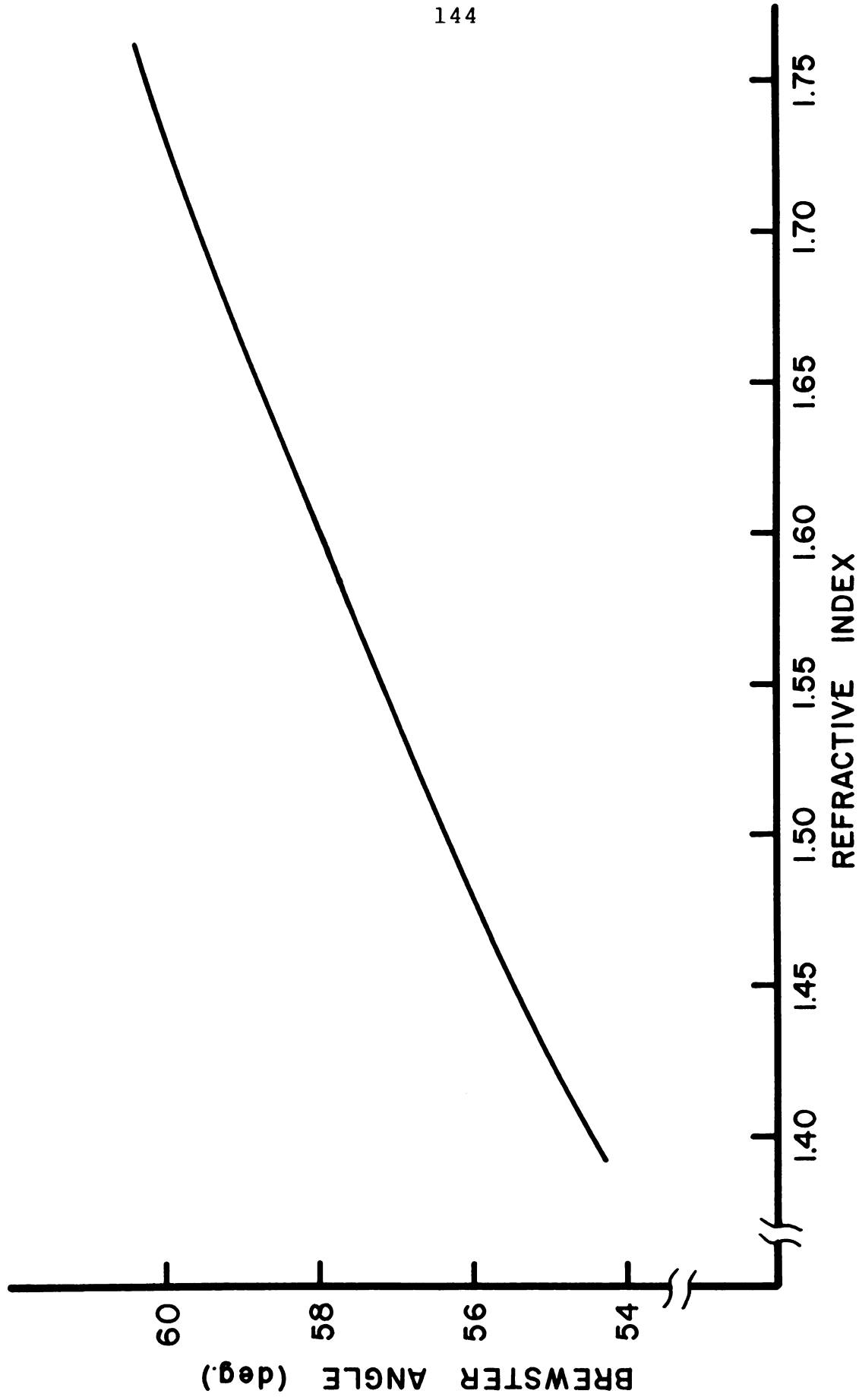


Figure 5.5. Refractive Index Dependence of Brewster Angle.

quantities and realizing that  $\theta + \theta' = \frac{\pi}{2}$  if  $\theta$  is the Brewster angle  $\theta_b$ ,  $r_s - r_p$  can easily be calculated:

$$(r_s - r_p)_{\theta_b} = \left( \frac{n^2 - 1}{n^2 + 1} \right)^2 \quad (5-29)$$

This function is plotted in Figure 5.6, with the values of  $r_s - r_p$  at the  $\theta$  angle which maximizes  $r_s - r_p$ , as a function of the refractive index.

To summarize this analysis, with reference to these plots, it is quite obvious that: (1) the angle of incidence which maximizes  $r_s - r_p$ , hence the sensitivity of our calibration, is not a strong function of the refractive index and is less dependent on refractive index than the Brewster angle is; (2) the  $r_s - r_p$  values for this maximum sensitivity angle is only about 1.5 to 2.5 times as large as those for the Brewster angle of incidence, for a given refractive index.

From this analysis, one is tempted to begin using this maximum sensitivity angle. This is consistent with practical considerations if one uses an appropriate photometer which can be conveniently manipulated. However, for the Brewster angle of incidence,  $r_s - r_p$  approaches zero and the minimum in  $I$  is easier to detect. A quick experiment proved that it could be detected by visual inspection of the reflection spot on the ceiling to an accuracy and precision within the precision of the polarization rotator.

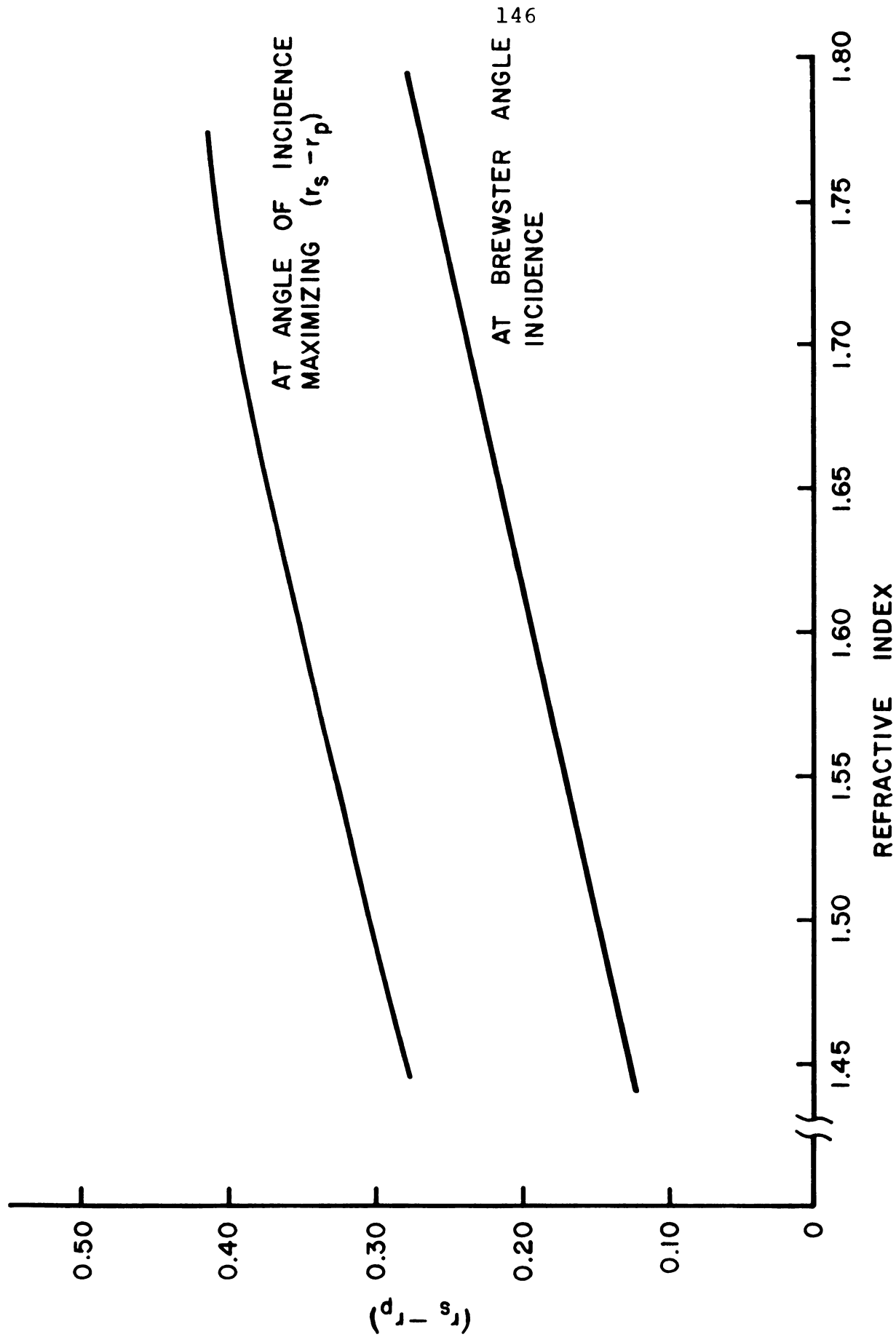


Figure 5.6. Refractive Index Dependence of  $r_s - r_p$ .

In addition to this minimization of intensity by comparison to zero, for the Brewster angle of incidence, we do not experience internal, or multiple reflection complications.

Before detailing the polarization alignment procedure, it should be emphasized that a similar analysis with the glass plate's incidence plane coinciding with the horizontal yz plane, shows that the beam's polarization vector is vertical when the reflected beam is maximum. Also, note that for any given incidence plane, vertical polarization and horizontal polarization are related to one another by minimum rather than maximum reflections or vice versa.

### Experimental Technique

After adjusting the laser so that its beam is traveling in a true horizontal direction relative to the optical table, we need to project this direction (z axis) onto the ceiling. Vertical projection is easily accomplished by using a plumb bob; the plumb bob tip touches the laser beam and the string top touches the ceiling. This needs to be done at only two points, well separated points, along the laser beam. A string drawn between thumb tracks or a line drawn on the ceiling between these two points represents the laser beam projection onto the ceiling. Then a glass plate of known refractive index is inserted into the beam and adjusted until its reflection spot falls onto the ceiling projection line at a point along the line



corresponding to a Brewster angle of incidence. The determination of this position corresponds to measuring a distance,  $d$ , along the ceiling projection from another point directly above the spot where the laser beam intersects the glass plate. This latter point is also determined by plumb bobbing. Referring to Figure 5.7, we see that  $d$  is given by:

$$d = h \tan \left( 2\theta_b - \frac{\pi}{2} \right)$$

After this point is established, the polarization rotator is rotated to give zero intensity (approximately) for this spot on the ceiling in a darkened room. The polarization rotator's index was then adjusted to read zero.

Having obtained a light beam whose polarization vector is vertical in the laboratory coordinate system, polarization analyzers are inserted into this laser beam. After rotating the analyzers until a maximum (or minimum) intensity is transmitted, their index is adjusted to give desired readings or, simply, the device's reading associated with vertical orientation is recorded.

Typically, the distance from the ceiling to the laser beam is greater than 5 feet; plumb bobbing is sensitive to within 5 mm on the ceiling; and, the laser's beam diameter is 5 mm or less. For these dimensions, the angular error



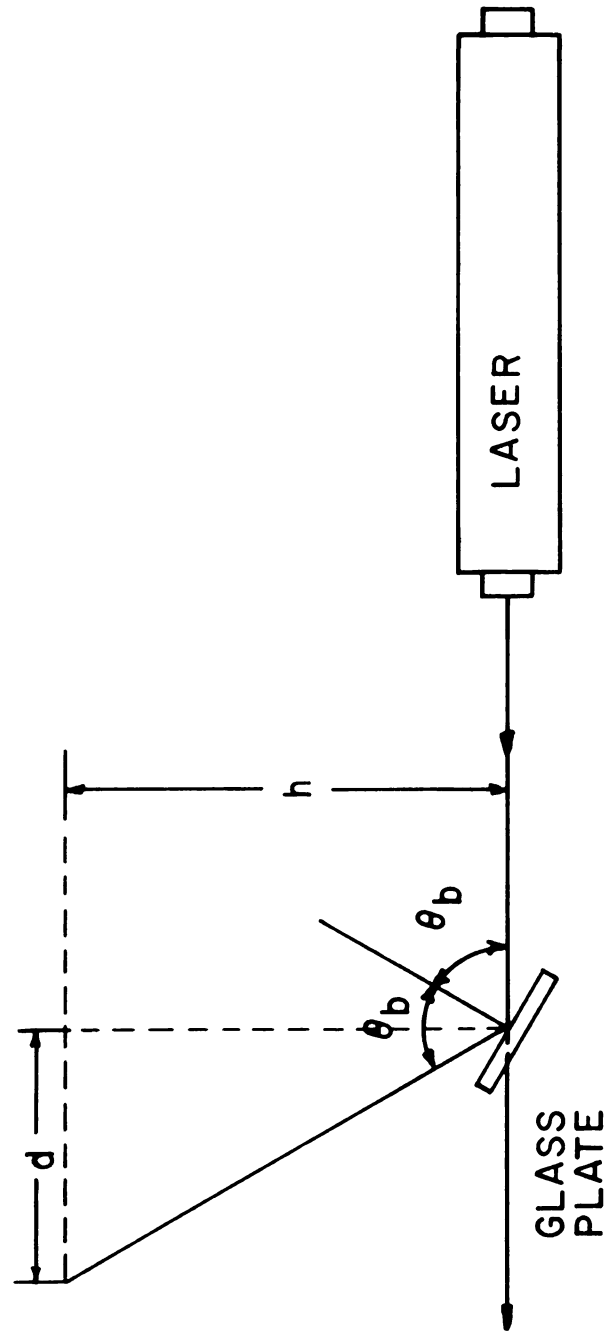


Figure 5.7. Polarization Alignment.

of the polarization vector will be about 3 milliradians or less. In later sections on vertical depolarization ratio measurements, the comparison of results from this apparatus to those of Anderson and Dosser ascertain an accuracy of this magnitude.

## CHAPTER VI

### SAMPLE PREPARATION AND HANDLING

The glassware used for preparing samples was dipped into a solution of 5 per cent hydrofluoric acid, 33 per cent nitric acid, 62 per cent distilled water and a small pinch of soap. Then the glassware was rinsed alternately in distilled water and aqua regia three or four times, rinsed about ten times with conductance water, and then dried in a vacuum dessicator.

The sample cells were washed with a detergent solution after it was filtered, rinsed ten times with conductance water, and dried in a vacuum dessicator. The cells were stored in a vacuum dessicator and flushed with the sample of interest, just before use, until no speckling of a laser beam was evident.

The conductance water, used primarily for cleaning, was prepared by first passing distilled water through a commercial demineralizer and then distilling it through a column 1.5 meter tall and packed with 7 mm sections of 7 mm OD glass tubing. After discarding the first 200 cc. of distillate (distillation flask initially filled with 2 liters), the next liter was collected and stored in a



large polyethylene bottle until used. The nonvolatile residue was found to be 0.34 ppm.

Reagent grade benzene was used. The large quantities used for cleaning were distilled once, without ebullition, and stored in a sealed container. The benzene used for scattering samples was also fractionally crystallized and dried by vacuum distillation just before use.

Sealed, pint bottles of reagent grade carbon tetrachloride were used for cleaning purposes. It was found to be dust free enough for that purpose. The scattering samples were distilled under vacuum just before use.

The glycerine was reagent grade. It was heated to 105° C for two hours under a vacuum to remove volatile impurities just before its spectra was taken.

A sample of fluorescein was recrystallized from reagent grade ethanol solutions twice and then dissolved in ethanol.





## CHAPTER VII

### EXPERIMENTAL RESULTS

#### Temperature Dependence of Depolarization Ratio

In the past, many different methods have been devised to measure depolarization ratios, for example see Fabelinskii (97). With the advent of the laser, new techniques are evolving, see Anderson (82) and Porto (100). The primary difference between the traditional and laser techniques is the measurement of  $\rho_u$  or  $\rho_v$ , which is more desirable. Even though it was demonstrated that several techniques could be utilized on this instrumental system; only a technique similar to that of Anderson (82) and Dosser (101) was extensively investigated.

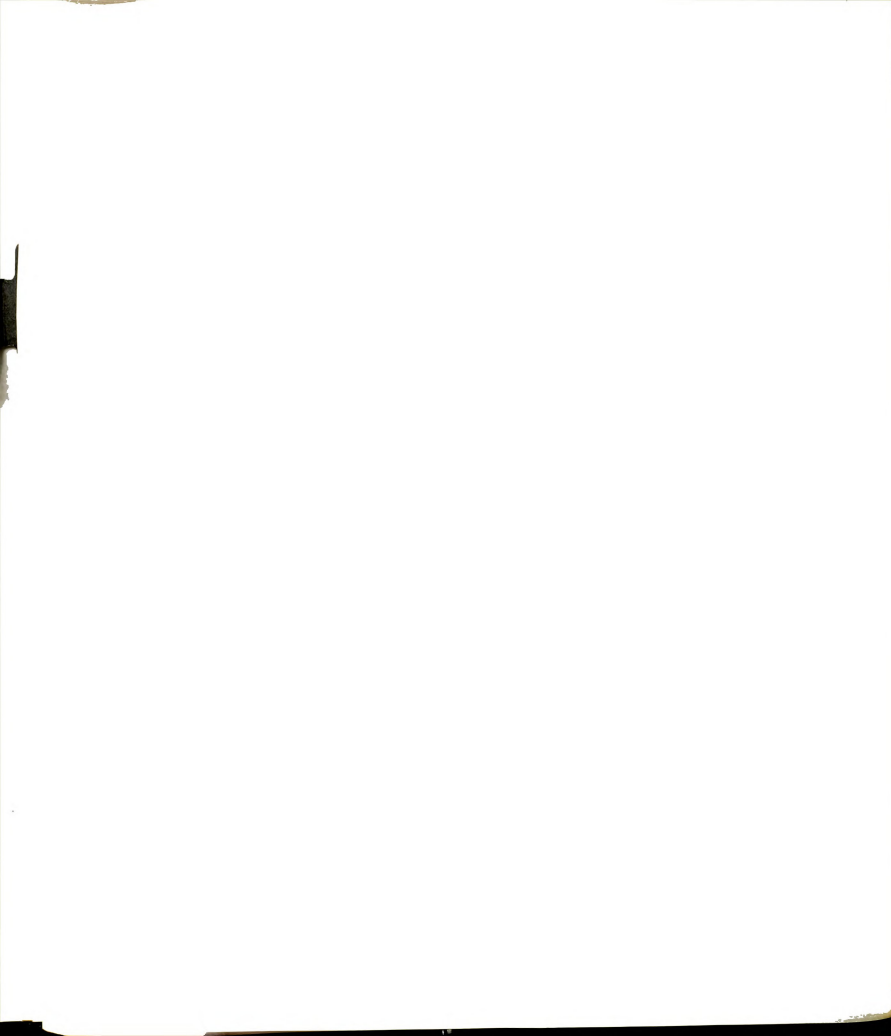
An important difference between this experimental apparatus and Anderson's (82), Dosser's (101) and most of the traditional apparatus is the relatively large distances between the light sources, sample cell and detection optics. (This advantage could be increased by removing the collection optics and only using a polarization analyzer near the photomultiplier.) From a point of view of accuracy, it is best to leave the photomultiplier tube in its normal position rather than mounting it onto the rotating table. The alignment technique for this instrument differs in that



only one polarizing element is used in the optical detection subsystem instead of two. The latter difference reduces errors associated with polarizer alignments and uncertainties in the ratio of maximum transmission for two polarizing elements.

The experimental method consists of aligning the incident laser beam (angle of incidence and polarization vector) and using a pentaprism to reflect the incident beam into the detection system for alignment of the collection optics which include an Ealing precision polarizer/analyzer unit with 3 minute resolution. The laser used for these depolarization studies was a Spectra Physics model 120/256 Stabilite, helium-neon laser with a measured 3.8 milliwatt output power and approximately 1.7 milliradian beam divergence. A model 310 polarization rotator was mounted onto the laser to align the polarization vector. After passing through the interferometer housing without its mirrors installed, the beam was still focused onto the photomultiplier tube. The picoammeter output was fed into the digital voltmeter. The digital voltmeter reduces the scaling difficulties for small depolarization ratios.

The polarization analyzer was rotated, searching for its position which minimized the photomultiplier output (minima easier to locate than maxima). This analyzer reading, defining the orientation for horizontal polarization component measurements was recorded. The orientation



for measuring the beam's vertical component simply corresponds to a 90 degree rotation of the analyzer.

With the sample in a square cell appropriately aligned relative to the incident beam, the temperature controller was set and a sufficient amount of time allowed for the sample to reach thermal equilibrium. Digital voltmeter readings for the vertical and horizontal orientations of the analyzer were recorded along with an independent temperature measurement. A new temperature setting was made and this measurement cycle repeated until the desired temperature range was fully scanned.

The results for benzene and carbon tetrachloride are in Table 7.1 and Table 7.2; a graphical comparison is made to the Anderson and Dosser results in Figure 7.1 and 7.2.

The graphs are of the Arrhenius type and after a data transformation from

$$\rho_v = \rho_{v0} e^{-\Delta E/RT} \quad (7-1)$$

to

$$-\ln \rho_v = -\ln \rho_{v0} + \frac{\Delta E}{1000R} \left( \frac{1000}{T} \right) \quad (7-2)$$

a simple least square, linear regression analysis was undertaken for the different data sets, Table 7.3 and 7.4.

Included in this table are some back calculations. The

$\delta \rho_v$ 's were calculated from



TABLE 7.1.--Depolarization Ratio Versus Temperature for Benzene.

Temp Setting (°C)	Measured Temp (°C)	Depolarization Ratio	$1/T \times 10^3$ (°K <sup>-1</sup> )	$-\ln \rho_v$
11	11.1	0.2776	3.5174	1.2816
15	15.2	0.2707	3.4674	1.3067
20	20.3	0.2647	3.4072	1.3292
25	24.6	0.2577	3.3580	1.3560
30	29.7	0.2488	3.3014	1.3911
35	34.8	0.2439	3.2468	1.4110
40	39.7	0.2354	3.1959	1.4465
45	44.5	0.2307	3.1476	1.4666
50	49.5	0.2240	3.0989	1.4961
55	54.4	0.2207	3.0525	1.5110
60	59.2	0.2139	3.0084	1.5422
65	64.3	0.2077	2.9630	1.5717
70	69.1	0.2048	2.9214	1.5857
75	74.1	0.1992	2.8794	1.6134





TABLE 7.2.--Depolarization Ratio Versus Temperature for  
Carbon Tetrachloride.

Temp Setting (°C)	Measured Temp (°C)	Depolarization Ratio	$1/T \times 10^3$ (°K <sup>-1</sup> )	$-\ln \rho_v$
12	12.3	0.01710	3.5026	4.069
15	15.3	0.01693	3.4662	4.079
20	20.2	0.01658	3.4083	4.100
25	24.7	0.01624	3.3568	4.120
30	29.8	0.01571	3.3003	4.153
35	34.7	0.01537	3.2478	4.175
40	39.6	0.01492	3.1969	4.205
45	44.6	0.01467	3.1466	4.222
50	49.4	0.01431	3.0998	4.246
55	54.3	0.01414	3.0534	4.259
60	59.3	0.01372	3.0075	4.289
65	64.3	0.01353	2.9630	4.306
70	69.1	0.01309	2.9214	4.335

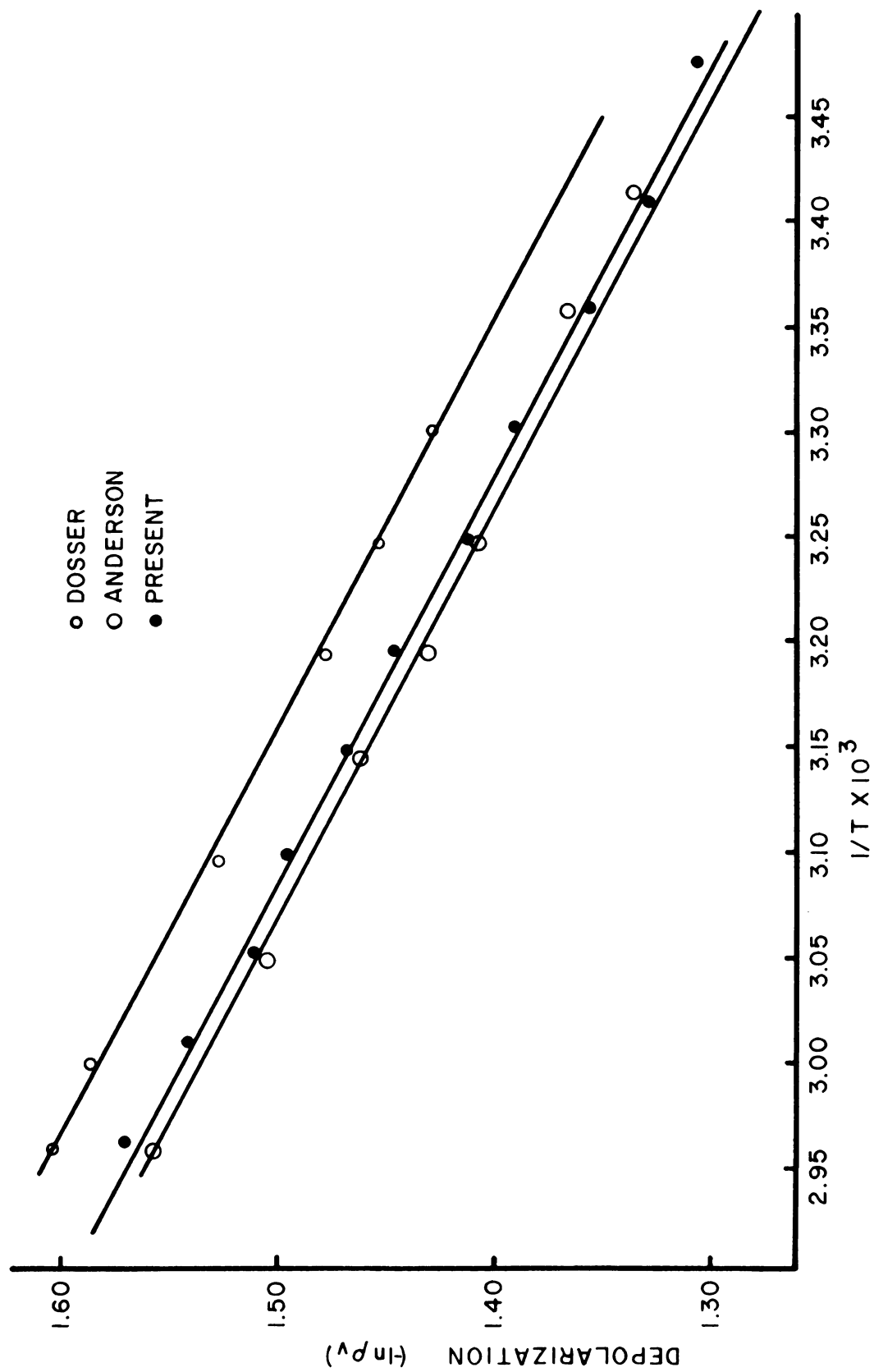


Figure 7.1. Temperature Dependence of Benzene Depolarization.

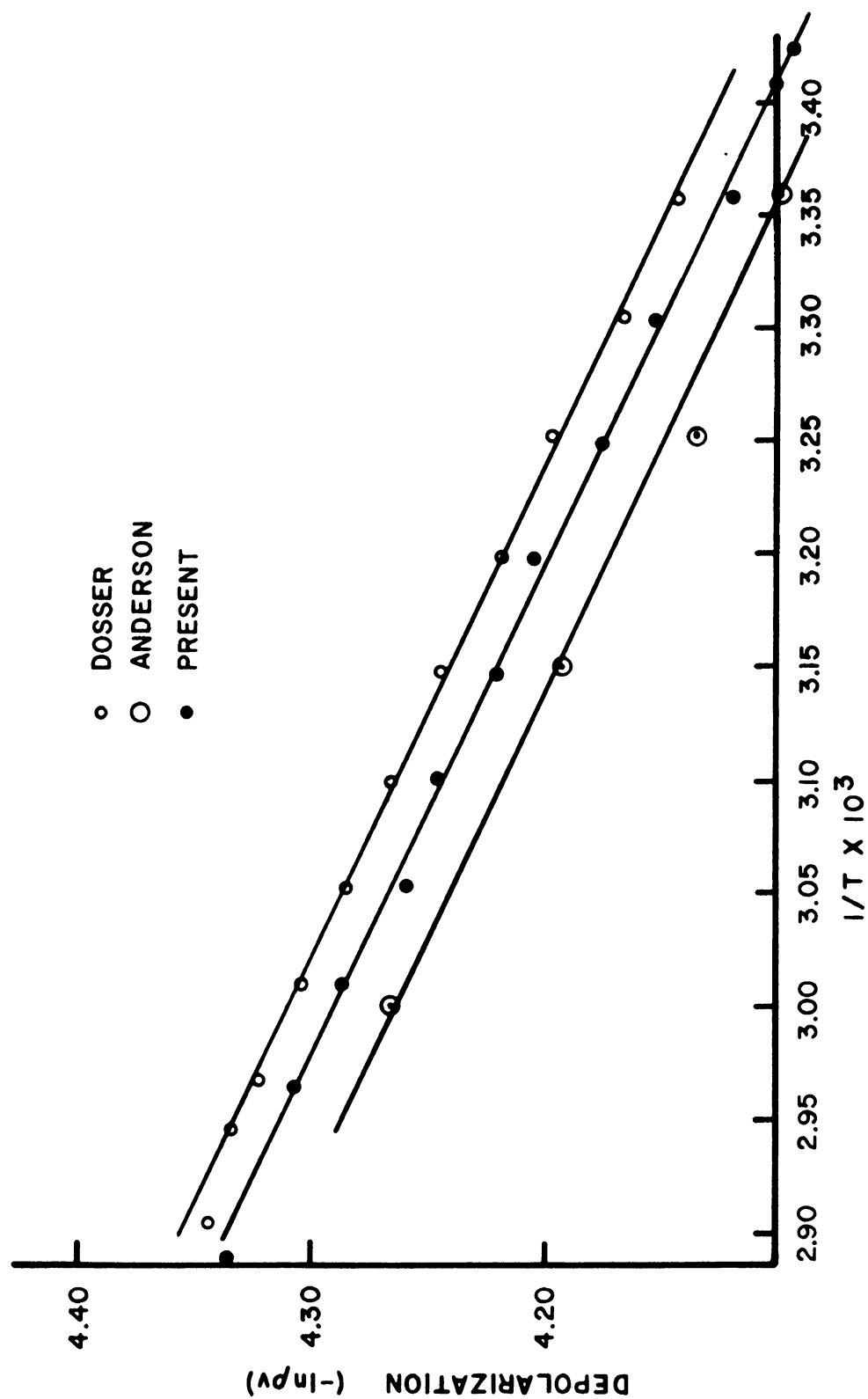


Figure 7.2. Temperature Dependence of Carbon Tetrachloride Depolarization.



TABLE 7.3.--Analysis of Benzene Depolarization Data.

	Present	Dosser	Anderson
Total Mean Square Deviation	$11.68 \times 10^{-3}$	$4.73 \times 10^{-3}$	$6.08 \times 10^{-3}$
Regression Mean Square Deviation	$15.16 \times 10^{-2}$	$1.88 \times 10^{-2}$	$3.63 \times 10^{-3}$
Error Mean Square Variation	$2.19 \times 10^{-5}$	$4.17 \times 10^{-5}$	$3.72 \times 10^{-5}$
Index of Determination	0.99827	0.99339	0.99491
Correlation Coefficient	-0.99914	-0.99669	-0.99745
F-Ratio	6930.0	451.1	977.3
Parameter			
A= $-\ln \rho_{VO}$	3.11179	2.99179	2.98135
B= $\Delta E/1000R$	-0.52185	-0.49581	-0.48289
Number of Observations	14	5	7
Subsequent Calculations			
$\rho_{VO}$	0.0442	0.0502	0.0507
$-\Delta E$	1036.9	985.1	959.5
$\delta \rho_V$ (25°C)	0.0031	0.0012	0.0016



TABLE 7.4.--Analysis of Carbon Tetrachloride Depolarization Data.

	Present	Dosser	Anderson
Total Mean Square Deviation	$7.86 \times 10^{-3}$	$3.80 \times 10^{-3}$	$3.13 \times 10^{-3}$
Regression Mean Square Variation	$9.41 \times 10^{-2}$	$5.06 \times 10^{-2}$	$1.23 \times 10^{-2}$
Error Mean Square Variation	$2.64 \times 10^{-5}$	$19.76 \times 10^{-5}$	$7.29 \times 10^{-5}$
Index of Determination	0.99693	0.95170	0.98253
Correlation Coefficient	-0.99846	-0.97555	-0.99123
F-Ratio	3566.8	256.2	168.7
Parameter			
A= $-\ln \rho_{vo}$	5.66648	5.55416	5.38957
B= $\Delta E/1000R$	-0.45850	-0.417741	-0.38464
Number of Observations	13	15	5
Subsequent Calculations			
$\rho_{vo}$	$3.460 \times 10^{-3}$	$3.871 \times 10^{-3}$	$4.564 \times 10^{-3}$
$-\Delta E$	911.0	830.1	764.2
$\delta \rho_v$ (25°C)	$1.3 \times 10^{-4}$	$0.6 \times 10^{-4}$	$0.5 \times 10^{-4}$





$$\delta \rho_V = \rho_V \delta (\ln \rho_V) \quad (7-3)$$

and are a measure of the precision of the  $\rho_V$  measurements. The  $\Delta E$ 's are activation energies, energy barriers for the depolarization mechanism.

It is interesting to note that the plots of the three different sets of data, for a given sample, are very nearly parallel; and the scatter of the present sets of data seem to be worse. The distance between these parallel lines represent the logarithm of a constant factor which may be taken as a measure of accuracy. For carbon tetrachloride and benzene, the accuracies are respectively 3.6% and 4.7% of the actual depolarization ratio.

A detailed study of the statistical parameters in Tables 7.3 and 7.4 implies that the present technique may be more accurate even though it is less precise for a given data point; that is, for this apparatus and experimental technique, accuracy more closely approaches precision. The reduced precision of the present scheme is easily explained by noting that no averaging was applied to the individual data points and the resetability of the polarization analyzer's rotations is less than that for the fixed polarization analyzers in the Anderson and Dosser apparatus. The increase in accuracy, due to instrumental geometry etc., agrees with an error analysis, for depolarization ratio measurements, detailed in Anderson's work. The accuracy



estimates for this apparatus are approximately 2% for depolarization ratios of about 0.01 and less than 0.1% for depolarization ratios greater than 0.25.

Wavelength Dependence of Benzene  
Depolarization Ratio

With the acquisition of the argon ion laser, it was deemed desirable to run a series of depolarization experiments on benzene at various wavelengths. The experimental system was aligned in the same manner as in the previous depolarization ratio experiments. The benzene sample was held at 25.0° C in a square cell by the temperature controller. The previous method wherein the vertical and horizontal polarization components were measured and the depolarization ratio calculated was used. The procedure was repeated five times; an average and standard deviation were calculated and tabulated in Table 7.5.

Included in Table 7.5 is the value at 25° C previously obtained using a helium-neon laser. Additional depolarization ratios were measured using a mercury vapor lamp. Collimating lenses and apertures were used to give a collimated, small diameter beam. The beam had a diameter of 5 mm at the scattering cell and an estimated divergence angle of 8 milliradians. The beam was polarized with Polaroid type HN-32 material. Different wavelengths were obtained using narrow band filters.



TABLE 7.5.--Vertical Depolarization Ratio Versus Wavelength for Benzene.

Light Source	Wavelength (nm)	Vertical Depolarization Ratio
Mercury Vapor Lamp	366	$0.285 \pm 0.008$
Mercury Vapor Lamp	436	$0.272 \pm 0.011$
Argon Ion Laser	457.9	$0.269 \pm 0.005$
Argon Ion Laser	488.0	$0.263 \pm 0.005$
Mercury Vapor Lamp	546	$0.261 \pm 0.008$
Helium-Neon Laser	632.8	$0.258 \pm 0.003$

The depolarization ratios are plotted in Figure 7.3. Extensive effort was not applied in the data collection or analysis; hence, one cannot conclude confidently relative to these results. However, these data imply the vertical depolarization ratio for benzene, at 25° C, may be a non-linear function of wavelength and it may be worthwhile to pursue this topic more extensively. The experiment is a good illustration of the use of different light sources (wavelengths) to expand the versatility of this light scattering apparatus.

#### Polarization Coherency Matrix for Benzene Scattered Light

This experiment illustrates the possibility of using this instrument for the determination of the polarization coherency matrix (PCM) of a light beam. The light beam studied was the light scattered at 90 degrees from a benzene sample in a square cell, temperature maintained at 25° C, and illuminated with a 5 milliwatt helium-neon laser. Momentarily, ignoring the analyzer optics, the optics were aligned as discussed in the alignment chapter except the interferometer mirrors were not installed. The picoammeter output was fed into the digital voltmeter; functioning on a ten second base, the digital voltmeter provided averaged data in a digital form.

Although many experimental techniques are possible, the straightforward technique (advantageous for demonstration

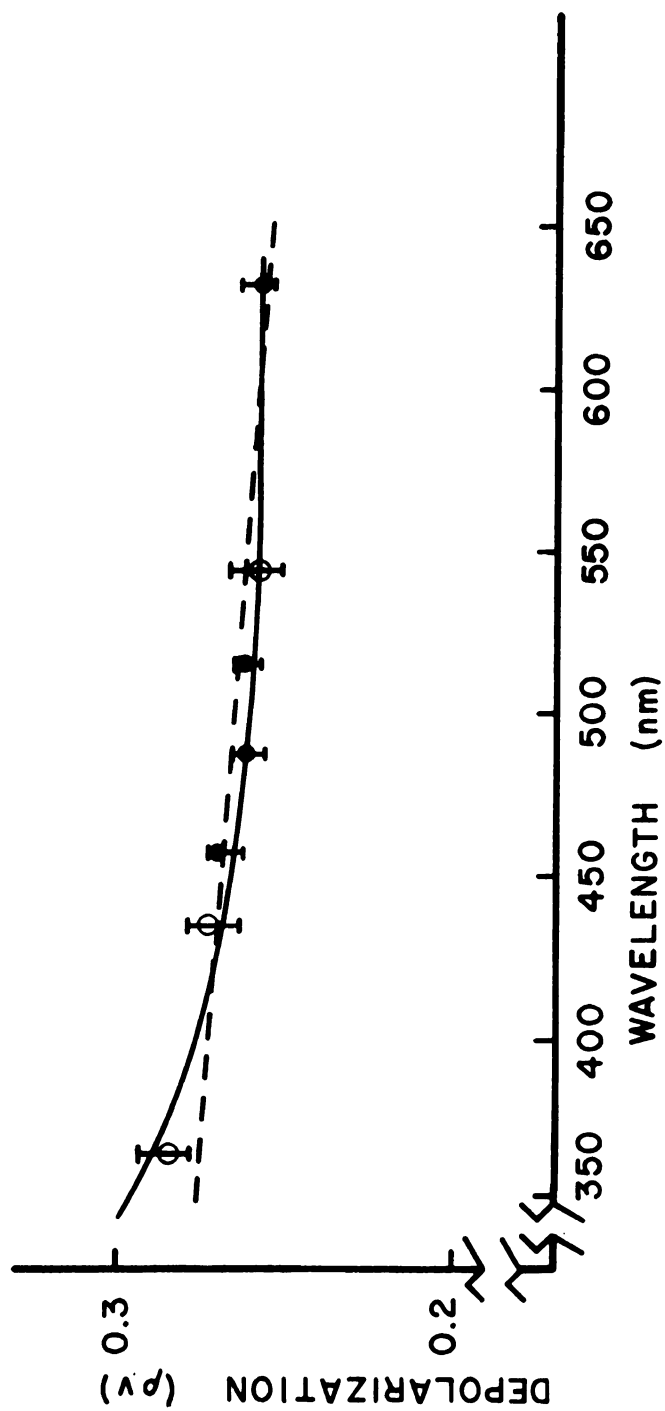


Figure 7.3. Wavelength Dependence of Benzene Depolarization.





purposes) outlined by equations (2-51,54) was adopted. A precision polarizer/analyzer unit was inserted into the beam and the transmitted intensity measured for  $0^\circ$  (vertical),  $45^\circ$ ,  $90^\circ$  and  $135^\circ$ . The six intensity values were substituted into equations (2-51,54) and the PCM elements were calculated.

Before the sample was measured, a vertically polarized laser beam was sent along the system's optical axis by substituting a pentaprism for the sample. The polarization analyzer's reading, zero or vertical reference point, for maximum transmission was noted. The quarter wave plate was then inserted and its orientation locked at the orientation yielding a maximum transmitted intensity; the vertical polarization vector was not rotated. Now, by comparing these two maximum transmittance values, one obtains a transmittance correction factor for inserting the quarter wave plate. The factor is  $0.972^3$  (average of five such comparisons) and has been applied to the  $I(\frac{\pi}{4}, \frac{\pi}{2})$  and  $I(\frac{3\pi}{4}, \frac{\pi}{2})$  data in Table 7.6. The entire data set, hence the PCM elements, was normalized by inserting an attenuator between the picoammeter and the DVM and adjusting it to yield a DVM reading of 1.000 when the scattered beam was incident on the polarization analyzer in its vertical position.

The tabulated  $I(\theta, \epsilon)$  data points were averaged for the five different experimental sequences and the average



TABLE 7.6.--Polarization Coherency Matrix Data for Benzene.

Run	$I(\theta, \epsilon)$					
	$I(0,0)$	$I(\frac{\pi}{2},0)$	$I(\frac{\pi}{4},0)$	$I(\frac{3\pi}{4},0)$	$I(\frac{\pi}{4},\frac{\pi}{2})$	$I(\frac{3\pi}{4},\frac{\pi}{2})$
1	1.021	0.263	0.642	0.639	0.645	0.641
2	1.000	0.258	0.629	0.631	0.627	0.630
3	0.988	0.255	0.621	0.625	0.626	0.618
4	1.008	0.260	0.636	0.635	0.631	0.633
5	0.995	0.257	0.624	0.623	0.623	0.627
ave	$1.002^4$	$0.258^6$	$0.630^4$	$0.630^6$	$0.630^4$	$0.629^8$



values were used in equations (2-51,54) to calculate the PCM elements:

$$\mathbf{J} = \begin{bmatrix} 1.002^4 & -0.000^2 + 0.000^6 i \\ -0.000^2 - 0.000^6 i & 0.258^6 \end{bmatrix}$$

The depolarization ratio

$$\rho_v = \frac{0.258^6}{1.002^4} = 0.258^0$$

agrees with the values in the previous sections. The degree of coherence

$$\frac{|J_{xy}|}{\sqrt{J_{xx}} \sqrt{J_{yy}}} = 0.00^{12}$$

indicates the polarization incoherence of the scattered light; the scattering centers are uncorrelated over the scattering volume element. Although the PCM off diagonal elements are known to be zero for light scattered from a liquid, this experiment may become informative when applied to crystals, highly oriented polymers, liquid crystals, or optically active compounds. Perhaps the polarization coherence studies may be augmented with Mallick (102,88) spatial-time coherence experiments.

### Angular Dependence of Light Scattering

As stated in the alignment and calibration chapter, this experiment represents a test for a cylindrical sample cell's alignment. It is an example of a photometric versus scattering angle experiment and a possible technique for determining depolarization ratios.

Coumou (90) has published measurements of the Rayleigh factor of several liquids as a function of the scattering angle. This experiment is based upon one of Coumou's equation rearranged to

$$\frac{L_{\theta}}{L_{90}} \sin^2 \theta = 1 + \left( \frac{1 - \rho_u}{1 + \rho_u} \right) \cos^2 \theta \quad (7-4)$$

$L_{\theta}$  is the scattered light flux viewed by the detection optics at the scattering angle  $\theta$ .  $\rho_u$  is the depolarization ratio for an unpolarized incident beam at a 90 degree scattering angle. Equation (7-4) avoids the need for correction factors, known solid angle of collection cone, calibration of photomultiplier currents in terms of an absolute light intensity, etc. When one plots the left hand side of this equation as a function of  $\theta$ , the symmetry of this plot is a test of the system's alignment, optical quality of the cylindrical sample cell and cleanliness of the sample. If one assumes a value for  $\rho_u$ , the calculated right hand side of equation (7-4) may be compared to the measured left hand side. A least square analysis of



$L_{\theta} \sin\theta/L_{90}$  versus  $\cos^2\theta$  will yield  $\rho_u$  from the slope and then  $\rho_v$  from the Krishnan relationship.

The incident beam was provided by the Siemens LG-64 laser; functioning in its multimode option, it provided an incident intensity of about 8.9 milliwatts at the sample cell. The incident beam was effectively depolarized by passage through a rotating half wave plate. The cylindrical sample cell and alignment techniques are elucidated in the previous chapters. The suppression network on the picoammeter was used to suppress the dark current (approximately  $7.1 \times 10^{-10}$  amp); with the damping constant at a maximum setting, the picoammeter was read directly. The readings are recorded in Table 7.7. A fluorescein solution was diluted until it yielded photomultiplier currents comparable to those for the other samples. All three liquids were temperature controlled at  $25.0^\circ \text{C}$ . The range of values is limited, by the width of the flat windows, between  $12^\circ$  and  $178^\circ$ ; however, due to inconveniences and emphasized effects of sample impurities at these low angles. Measurements were only done between  $20^\circ$  and  $160^\circ$ .

After appropriate transformation of the data in Table 7.7, a least square analysis ultimately yielded  $\rho_v$  values of  $0.0161^5$  and  $0.256^4$  for carbon tetrachloride and benzene respectively. These values agree well with those in the previous sections of this chapter. Using these





TABLE 7.7.--Angular Dependence of Light Scattering Data.

Scattering Angles (degrees)	$L_{\theta}$ , units of PMT current $\times 10^7$		
	Fluorescein Solution	Benzene	Carbon Tetrachloride
20	7.37	6.92	3.15
30	5.07	4.50	1.99
40	3.96	3.38	1.39
50	3.38	2.65	1.05
60	2.99	2.20	0.835
70	2.76	1.92	0.686
80	2.61	1.77	0.610
90	2.57	1.73	0.582
100	2.58	1.75	0.606
110	2.71	1.90	0.685
120	3.04	2.18	0.837
130	3.39	2.62	1.07
140	4.00	3.34	1.38
150	5.12	4.52	2.02
160	7.56	6.95	3.18

least square values, the right hand side of equation (7-4) was evaluated and is represented by the solid lines in Figure 7.4. Visual inspection of Figure 7.4 illustrates the good alignment of the system. The scatter of the experimental points about the calculated curves is easily accounted for by uncertainty in the picoammeter readings.

#### Landau-Placzek Ratio and Relative Brillouin Shift for Glycerine

While the instrument was being optically diagnosed, the adjustments optimized and the sample cell subsystem thermally calibrated, several Brillouin spectra were recorded for glycerine samples. Because of poor frequency resolution (optical misalignment etc.), uncalibrated Fabry-Perot interferometer and uncalibrated temperature settings, this data was not initially utilized for any purpose other than the determination of instrumental malfunctions. Afterwards, it was deemed that, at least approximate, Landau-Placzek ratios and a Brillouin shift expressed as a function of the interferometer's free spectral range could be obtained. In addition to providing guidelines for further experiments with glycerine, these results illustrate the instrument's utility in several manners. Therefore, on a qualitative basis, some of the better spectra were selected from the numerous recordings; Landau-Placzek ratios and relative Brillouin shifts were obtained

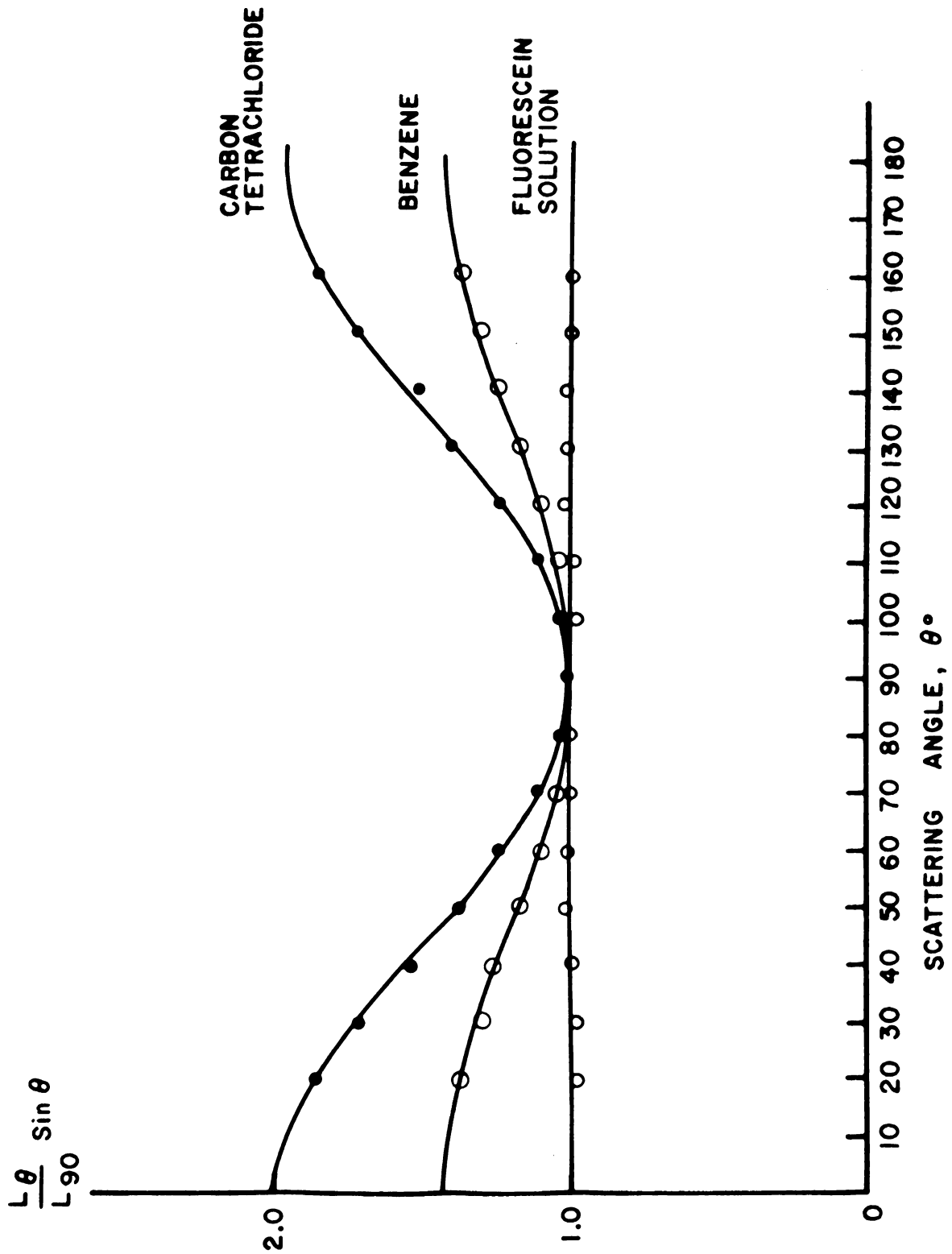


Figure 7.4. Angular Dependence of Light Scattering.

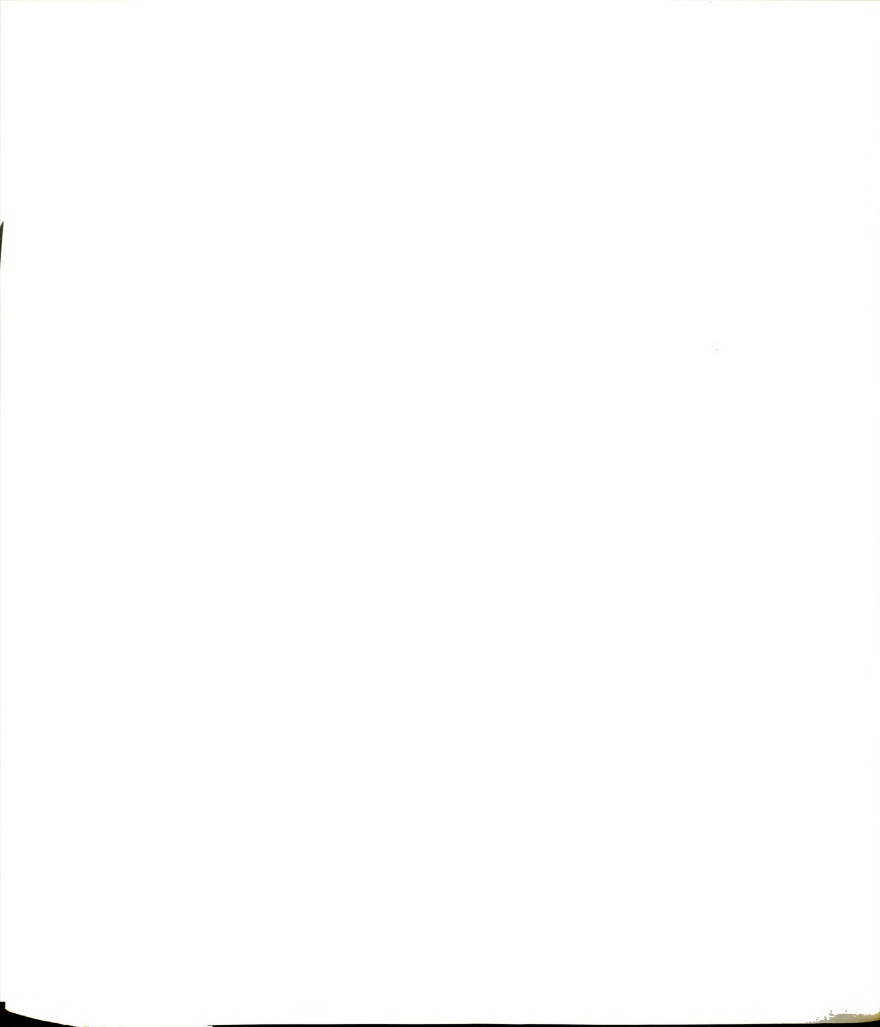
from them, in a manner described below, as a function of temperature.

For the selected spectra, the Spectra Physics model 125 (measured 78 milliwatt output) helium-neon laser was used. A square sample cell was aligned for a 90 degree scattering angle. The interferometer contained  $\lambda/100$ , 95% reflectance mirrors.

The pertinent linewidths were all measured as a fraction of the free spectral range; on the recorded spectra, the linewidths were measured as a fraction of the distance between two central Rayleigh peaks corresponding to adjacent interferometer modes. The areas, integrated intensities, were measured by "cutting the curve out" and weighting the paper. Then, following the three observations below, the Landau-Placzek ratios were calculated. First, Litovitz's group (120) has shown that

$$I_B = 2 I_+ (1 + \Delta_+ / \omega_p) \quad (7-5)$$

where  $I_B$  is the integrated intensity of a Brillouin peak;  $I_+$  is the integrated intensity of the high frequency half of a Brillouin peak (It is obtained at a lower error than  $I_B$  because of overlapping from the central line, etc.);  $\Delta_+$  is the halfwidth at halfheight corresponding to  $I_+$ , of the Brillouin peak;  $\omega_p$  is the Brillouin shift. Second, corresponding to Litovitz's experimental definition of the Landau-Placzek ratio, "the scattering spectrum due to



density fluctuations alone may be determined by subtracting 7/6 of the depolarized spectrum from the polarized spectrum". Finally, assuming the instrumental profile, measured and true spectral peaks are lorentzian functions, for the purpose of calculating Landau-Placzek ratios, it may be shown that an approximate deconvolution may be accomplished by:

$$A_t = A_m (1 + \Gamma_i / \Gamma_m) \quad (7-6)$$

wherein  $A_t$  is the area corresponding to the true spectrum,  $A_m$  corresponds to the experimental spectrum and  $\Gamma_i$  and  $\Gamma_m$  are the halfwidths at half height for the instrumental profile and experimental peak respectively.

To summarize, the detailed procedure was: (1) The halfwidths, at half height,  $\Delta_+$  and  $\omega_p$  were measured as a fraction of the free spectral range. (2) With the dark current as a baseline, the total area for the polarized spectra was evaluated. (3) The area for the depolarized spectra was obtained and 7/6 of its value was subtracted from the total area above. (4) The region for  $I_+$  was graphically isolated; cutting this portion away from the total area, this area was evaluated by weighing the paper. (5) Equation (7-5) was used to obtain a value for the Brillouin line and twice this value was subtracted from the total to obtain a value for the central Rayleigh line. (6) The Brillouin and Rayleigh areas were corrected for instrumental





broadening by applying equation (7-6); the instrumental profile halfwidth was approximated by the halfwidth of the central peak of a Brillouin spectra of benzene. (7) Finally, the Landau-Placzek ratio,  $I_C/2I_B$  was calculated from one-half of the ratio of these two areas. Note, in this data analysis procedure, all of the quantities appear as ratios in the calculation of the Landau-Placzek ratio hence their unconventional units cancel out.

The results are tabulated in Table 7.8. The Landau-Placzek ratios are graphed in Figure 7.5 as a function of temperature where they are compared to Litovitz's results. The relative Brillouin shifts are graphed in Figure 7.6 as a function of temperature. The utility of these plots are discussed by Litovitz. These two sets of Landau-Placzek ratios seem to agree quite well. The relative Brillouin shift data could be converted to actual Brillouin shifts by assuming one value, at one temperature, from some other work as a standard. This standard sample can be any liquid as long as it is also measured with the same Fabry-Perot mirror spacing. Perhaps this is a convenient calibration technique.

The temperature values in Table 7.8, have a  $0.2^\circ \text{C}$  uncertainty. The free spectral range, estimated from a measurement of the Fabry-Perot mirror separation at a later date is roughly 21.5 GHz (mirror separation of 1.395 cm).

TABLE 7.8.--Landau-Placzek Ratio and Relative Brillouin Shift for Glycerine.

Temperature, C	Landau-Placzek Ratio	Relative Brillouin Shift
10	1.90	0.432
20	1.82	0.411
30	1.71	0.400
40	1.56	0.383
50	1.22	0.358
60	1.01	0.331
70	0.70	0.310
80	0.48	0.292
90	0.32	0.283
100	0.33	0.270
110	0.22	0.260
120	0.25	0.251



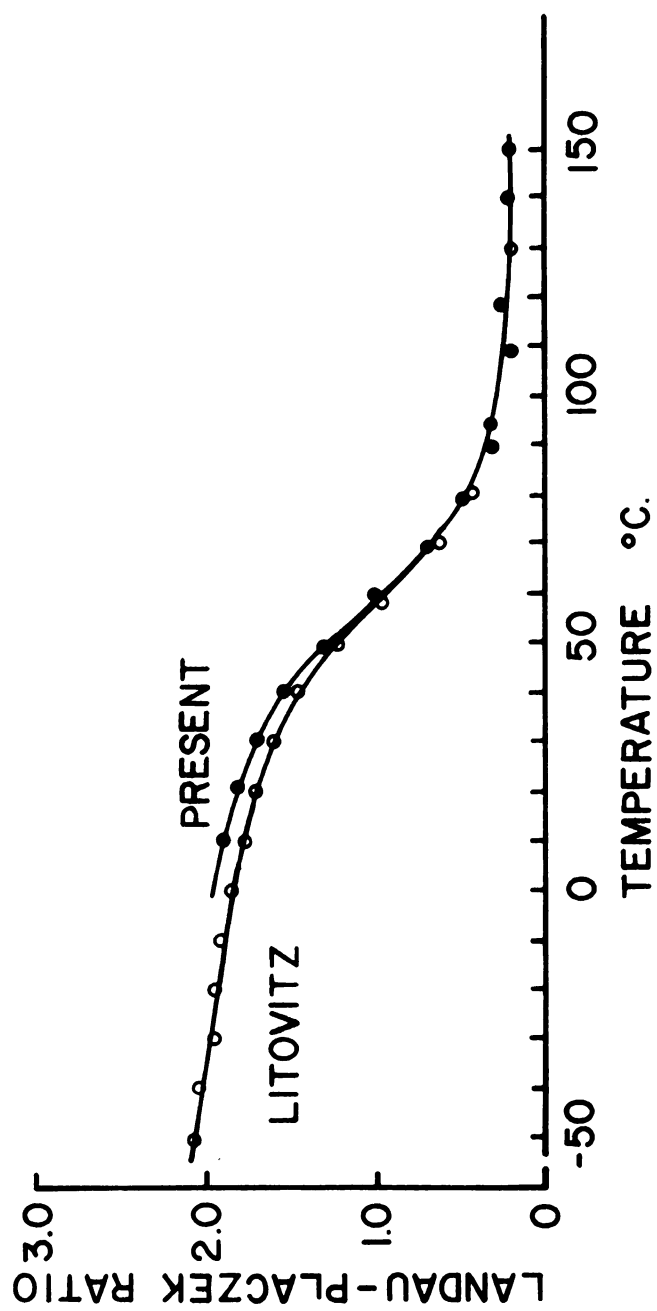


Figure 7.5. Temperature Dependence of Landau-Placzek Ratio for Glycerine.



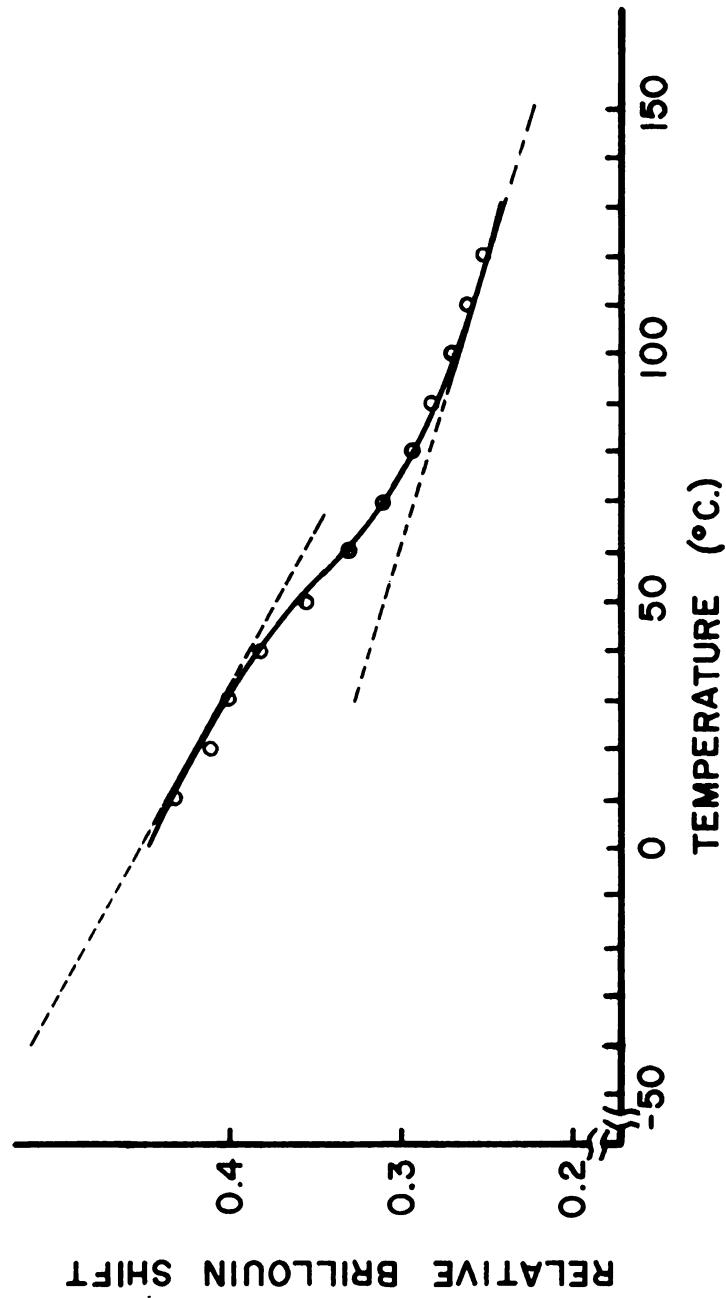


Figure 7.6. Temperature Dependence of Relative Brillouin Shift for Glycerine.



Brillouin Spectra of Carbon  
Tetrachloride

In order to examine the performance of the instrument in its most important mode, namely, as a Brillouin spectrophotometer, and to examine the use of the data analysis technique of Chapter III, several spectra of carbon tetrachloride were collected. Carbon tetrachloride was selected as a sample because: (1) Nichols and Carome (28) have demonstrated good agreement between theory (single relaxation) and experiment for  $6328 \text{ \AA}$  incident radiation. (2) The material parameters for theoretical calculations are readily available.

The argon ion laser was used in its stable, single mode configuration to excite the light scattering. Approximately 420 milliwatt, at  $4880 \text{ \AA}$ , was incident on the sample and the sample was viewed at 90 degrees. The sample, in a square cell, was temperature controlled at  $25.0^\circ \text{ C}$ . The interferometer's mirror spacing was set at 1.000 cm producing a 15.000 GHz free spectral range. This was accomplished by locking a telescope gauge to 1.000 cm "inside" a micrometer and then adjusting the mirror's position using the telescope gauge as a spacer. The ramp voltage to the piezoelectric transducer was first adjusted to yield a spectrum which could be conveniently reproduced in Figure 7.7; then, the ramp voltage was adjusted to a slow rate (about 1 volt/sec) and the recorder was operated



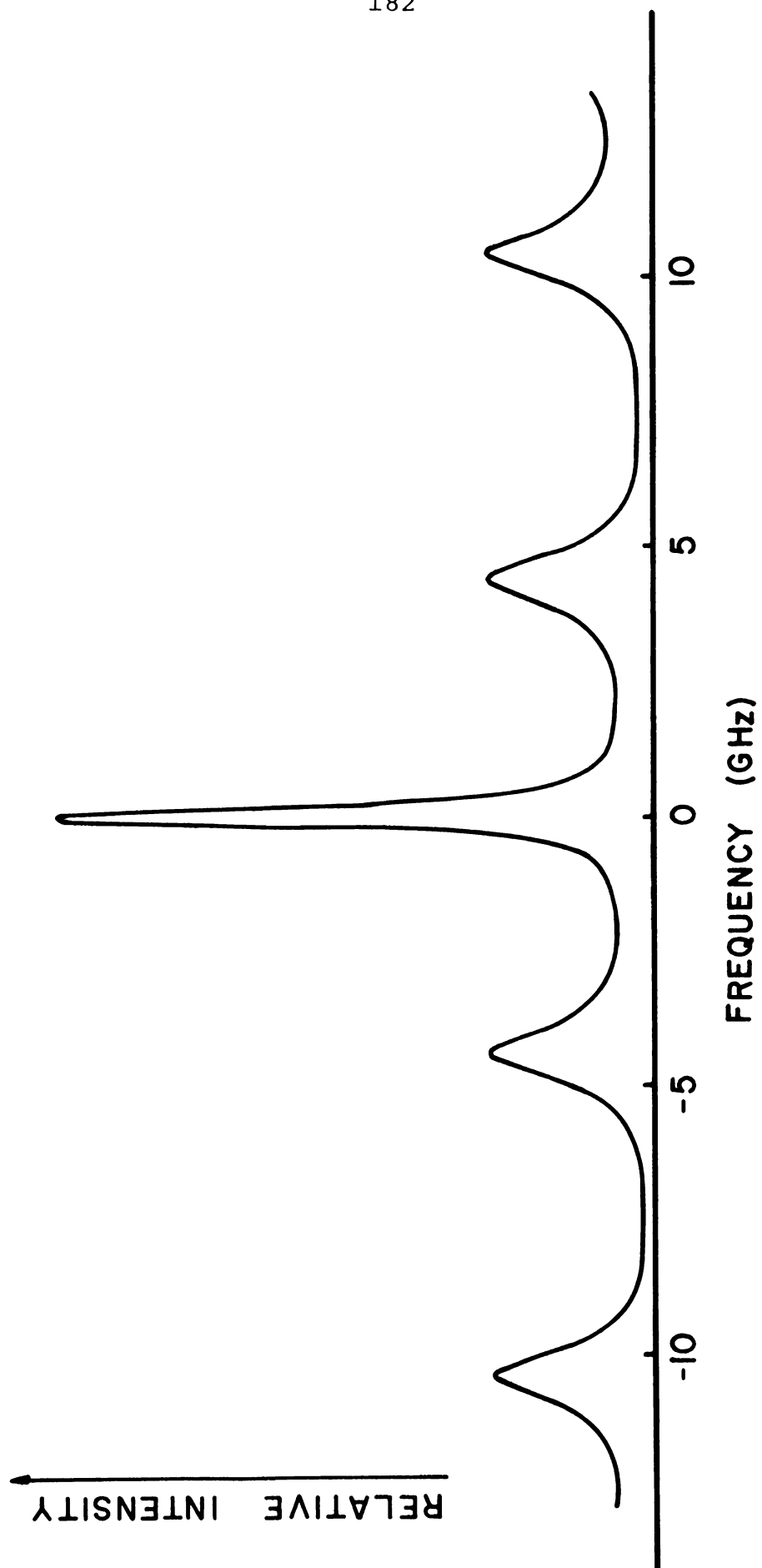


Figure 7.7. Brillouin Spectra for Carbon Tetrachloride.

at its fast chart speed in order to collect data with a relatively high frequency resolution. In order to determine the instrumental profile, the scattering process was simulated by focusing the incident laser beam onto an opal glass plate with a short focal length lens. The opal plate was first aligned so that it reflected the incident laser beam along the detection optics axis. The spectrophotometer alignment was optimized between individual runs.

Nine spectra were obtained but only one, chosen because it had the narrowest central line, corresponding to best instrumental finesse, was analyzed in detail. The rms difference between this experimental curve and a best fit curve is 0.63%. The instrumental bandwidth was 3.664 MHz corresponding to a finesse of 40.9. Both the instrumental profile and Brillouin spectrum data points were smoothed using a cubic, five data points, least square polynomial technique; data points at convenient frequency intervals were interpolated with these polynomials. The Brillouin spectrum was deconvoluted and curve fit using the techniques in Chapter III. The resulting spectral parameters (assuming the single relaxation model) are tabulated in Table 7.9.

In Table 7.9 is a set of theoretical values for the spectral parameters. They were calculated using the theory outlined in Chapter II and discussed by Nichols and Carome (28). Except for the refractive index, the



TABLE 7.9.--Theoretical and Experimental Values for Carbon Tetrachloride  
Brillouin Spectra Parameters.

Parameter	Symbol	Theoretical*	Experimental Best Fit Curve
Brillouin Shift	$\omega_B$	4.5005	4.5008
Brillouin Halfwidth	$\Gamma_B$	0.4495	0.4526
Thermal Damping Halfwidth	$\Gamma_{CT}$	0.0095	0.0126
Relaxational Damping Halfwidth	$\Gamma_{CI}$	2.2090	2.2121
Amplitude of Thermal Line	$A_{CT}$	0.31594	0.31596
Amplitude of Relaxational Line	$A_{CI}$	0.16836	0.16859
Amplitude of Symmetric Part of Brillouin Line	$A_{BS}$	0.27252	0.27271
Amplitude of Antisymmetric Part of Brillouin Line	$A_{BA}$	0.07826	0.03925

\* Units of GHz.

material parameters used in these calculations are those in Nichols' Table I. A refractive index of 1.4675 was interpolated, relative to wavelength and temperature, from the literature data (103).

Figure 7.8 is a comparison of curves calculated from the theoretical and experimental parameters in Table 7.9. The curves represent true spectra convoluted with the instrumental profile. Contributions due to adjacent interferometer modes are not included. This simplification helps illustrate the asymmetric component of the Brillouin peaks and experimentally corresponds to a higher free spectral range. The rms difference between these two curves is 0.99%, insignificantly larger than the rms difference between the experimental and best fit curve, 0.63%.

Another Brillouin experiment (104) on carbon tetrachloride (at 4880 Å incident radiation and at 25° C) yielded a value of 4.70 GHz for the Brillouin shift. The standard deviation of those measurements was greater than 4%; therefore, this Brillouin shift does not differ significantly from the one obtained in the present experiment.

The most important conclusion relative to this experiment is that good Brillouin spectra are obtainable from this instrumental system and they may be analyzed by the techniques of Chapter III. The small differences between the theoretical and experimental parameters in Table 7.9 should not be over emphasized as a measure of

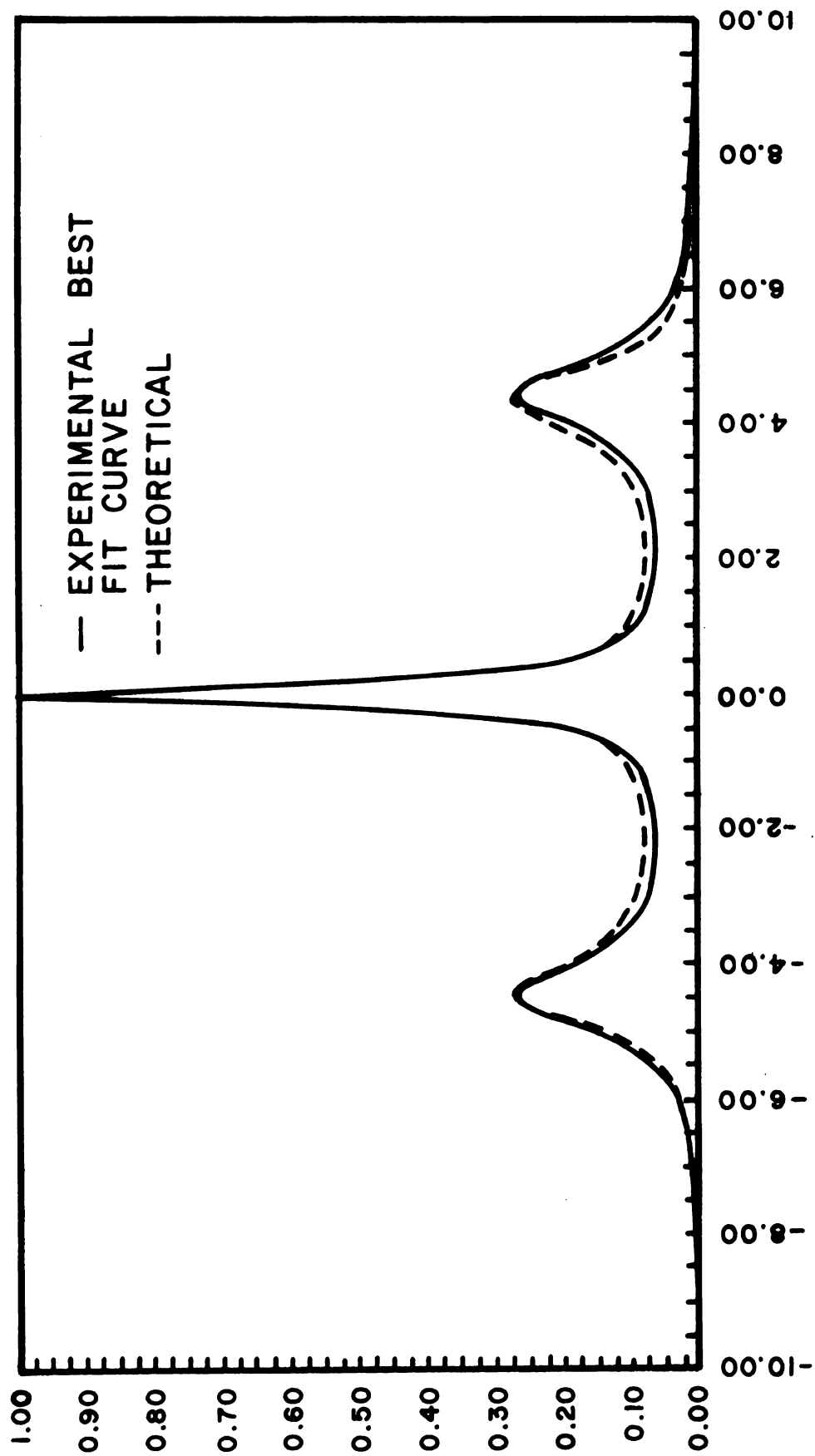


Figure 7.8. Calculated Brillouin Spectra for Carbon Tetrachloride.



the instrument's precision and accuracy since these data represent the best of nine spectra. The lack of a larger number of these "good spectra" is due to the interferometer's instability which should be reduced before one seriously considers the instrument's precision and accuracy of performance.



## CHAPTER VIII

### CONCLUSIONS

#### Summary

The instrumental system described in Chapters IV and V has proven to be useful and versatile. The experiments described in Chapter VII illustrate measurement of parameters which characterize the incident light beam, the response of the sample (and its scattering mechanism) and the scattered light beam. With the instrument in a photometric mode, the depolarization ratio of scattered light was measured as a function of the sample's temperature and the wave length of the incident light beam. The angular dependence of scattered light intensity was also studied. Spectrophotometrically, the Landau-Placzek ratio and relative Brillouin shift of glycerin were obtained as a function of the sample's temperature. A high quality Brillouinspectrum of carbon tetrachloride was obtained when the instrument was properly aligned; thus the primary objective of this research project to design and construct an instrument for this purpose was met.

Illustration of the instrument's versatility is presently being supplemented and expanded by the research

of several colleagues; among the projects are: (a) The depolarization ratio and Brillouin spectra of several sugars in the temperature region around the glass transition temperature have been determined (87,97). (b) The association of dimethyl sulfoxide in the liquid state is being studied using Landau-Placzek ratio measurements (87,86). (c) A new spectroscopic technique original with Miller (105 to 108) is being used to determine the molecular weight of polymers. (d) The Brillouin spectra (109) of polymer solutions are being investigated. (3) Photometric measurements of light scattering by inhomogeneities of polymers in the amorphous phase (88,110) are being made at low scattering angles with high angular resolution. (f) Stiso (105) has substituted a wave analyzer for the instrument's normal detection electronics, converting the system into a light beating spectrometer.

#### Future Research

The most serious deficiencies of this instrumental system are the interferometer's instability and the limit on finesse resulting from acceptance angle of the collection optics. The present interferometer's instability may be improved by housing it in a thermostat and reconstructing key portions, with a material of lower thermal expansion such as Invar. Solid etalon spaced interferometers with pressure scanning can provide a more linear scan (111,112).

Recently (113), "a highly stable alignment device using self-aligning bearings coupled with piezoelectric expansion columns has been developed and applied to a Fabry-Perot etalon. The accuracy of alignment was (reported to be) greater than  $\pm 10^{-7}$  radians." This is better than twice the accuracy claimed by the manufacturer of the present interferometer. Electronically stabilized, "double-passed" scanning interferometers have been reported recently (114).

The collection optics could be changed to reduce the acceptance angle of the interferometer; however alignment difficulties would increase. The acceptance angle could be decreased by focusing a small image of the scattering volume onto a very small pinhole. The beam transmitted through the pinhole would be a closer approximation to light emanating from a pin point. This option was considered in the early designs but was rejected because of the associated difficulties in optical alignment.

The polymeric foam in the optical table shows fatigue, thereby causing the optical table to become tilted, requiring realignment. Eventually, this effect may seriously reduce the foam's ability to attenuate acoustic vibrations. It is recommended that air filled inner tubes be considered as a replacement for the foam.

Collection of Brillouin spectra of a high quality has become a routine procedure with the result that data

analysis has become the limiting factor of useable output. Since this research was undertaken, Jansson (115) has published a method for "resolution enhancement of spectra" by deconvolution. It is recommended that this method, with analog-to-digital data collection, be given serious consideration. Day (116), Hildum (117) and others have recently discussed a technique useful for the deconvolution of Fabry-Perot profiles when one is willing to assume Lorentzian, Voigt or Gaussian shaped lines.

## BIBLIOGRAPHY

1. Richter, J. R., Ueber die neuern Gegenstande der Chemie, 11, 81 (1802).
2. Tyndall, J., Phil. Mag., 37, 384 (1869).
3. Lord Rayleigh, Phil. Mag., 41, 447 (1871); Ibid., 42, 81 (1881).
4. Einstein, A., Ann. Phys. Lpz., 33, 1275 (1910).
5. Mie, P., Ann. Phys. Lpz., 25, 3, 771 (1908).
6. Raman, C. V., Indian J. Phys., 2, 1 (1928).
7. Debye, P., J. Appl. Phys., 15, 338 (1944).
8. Fixman, M., J. Chem. Phys., 23, 2074 (1955).
9. Zimm, B. H., J. Chem. Phys., 13, 141 (1945).
10. Buckingham, H. D., and M. J. Stephen, Trans. Farad. Soc., 53, 884 (1957).
11. Carr, C. I. Jr., and B. H. Zimm, J. Chem. Phys., 18, 1616 (1950).
12. Benoit, H., and W. H. Stockmayer, J. Phys. Rad., 17, 21 (1956).
13. Anselm, A., Zh. Eksperim. i Teor. Fiz., 17, 489 (1947).
14. Prins, J. H., and W. Prins, Physica, 22, 576 (1956); Ibid., 23, 253 (1957).
15. Kielich, S., Bull. Acad. Polon. Sci. Ser. Sci. Math. Astron. Phys., 6, 215 (1958).
16. Pecora, R., and W. A. Steele, J. Chem. Phys., 42, 1872 (1965).
17. Shakhparonov, M. I., Dokl. Akad. Nauk., 136, 1162 (1961); Ukr. Fiz. Zh., 7, 782 (1962).

18. Theimer, O., and R. Paul, J. Chem. Phys., 42, 2508 (1965).
19. Frisch, H. L., and J. McKenna, Phys. Rev., 139, 168 (1965).
20. Komarov, L. I., and I. F. Fisher, Soviet Physics JETP 16, 1358 (1963).
21. Van Hove, L., Phys. Rev., 95, 249 (1954).
22. Mountain, R. D., J. Research NBS, 70A, 207 (1966).
23. Mountain, R. D., Rev. Mod. Phys., 38, 205 (1966).
24. Mountain, R. D., J. Research, NBS, 69A, 523 (1965).
25. Mountain, R. D., J. Acoust. Soc. Am., 42, 516 (1967).
26. Mountain, R. D., J. Chem. Phys., 44, 832 (1966).
27. Mountain, R. D., J. Research NBS, 72A, 95 (1968).
28. Nichols, W. H., and E. F. Carome, J. Chem. Phys., 49, 1000 (1968); Ibid., 49, 1013 (1968).
29. Bhatia, A. B., and E. Tong. Phys. Rev., 173, 231 (1968).
30. Brillouin, L., Ann. de physique, 17, 88 (1922).
31. Gross, E., Z. Physik., 63, 685 (1930); Nature, 126, 201 (1930), Ibid., 126, 400 (1930).
32. Cummins, H. Z., and R. W. Gammon, Appl. Phys. Letters, 6, 171 (1965); J. Chem. Phys., 44, 2785 (1966).
33. Gornall, W. S., G. I. A. Stegeman, B. P. Stoicheff, R. H. Stolen and V. Volterra, Phys. Rev. Letters, 17, 297 (1966).
34. Rank, D. H., J. S. McCartney, and G. J. Szasz, J. Opt. Soc. Am., 38, 287 (1948).
35. Rank, D. H., E. M. Kiess, Uwe Fink, and T. A. Wiggins, J. Opt. Soc. Am., 55, 925 (1965).
36. Rank, D. H., E. M. Kiess, and Uwe Fink, J. Opt. Soc. Am., 56, 163 (1966).
37. Landau, L., and G. Placzek, Physik. Zeits. Sowjetunion, 5, 172 (1934).

38. Maiman, T. H., Phys. Rev., 123, 1145 (1961).
39. Javan, A., W. R. Bennett, Jr. and D. R. Herriott, Phys. Rev. Letters, 6, 106 (1961).
40. Montrose, C. J., V. A. Solov'yev, and T. A. Litovitz, J. Acoust. Soc. Am., 43, 117 (1968).
41. Miller, G. A., J. Phys. Chem., 71, 2305 (1967); Ibid., 72, 4644 (1968).
42. Berne, B. J., and H. L. Frisch, J. Chem. Phys., 47, 3675 (1967).
43. Freedman, E., J. Chem. Phys., 21, 1784 (1953).
44. Born, M., and E. Wolf, Principles of Optics, Third Edition, Pergamon Press, Oxford, 1965.
45. Jenkins, F. A., and H. E. White, Fundamentals of Optics, Third Edition, McGraw-Hill Book Company, New York, 1957.
46. Francon, M., Optical Interferometry, Academic Press, New York, 1966.
47. Stone, J. M., Radiation and Optics: An Introduction to the Classical Theory, McGraw-Hill Book Company, New York, 1963.
48. Meissner, K. W., J. Opt. Soc. Am., 31, 405 (1941).
49. Meissner, K. W., J. Opt. Soc. Am., 32, 185 (1942).
50. Dufour, C., and R. Picca, Rev. Opt., 24, 19 (1945).
51. Chabbal, R., Rev. Opt., 37, 49 (1958).
52. Chabbal, R., Rev. Opt., 37, 336 (1958).
53. Chabbal, R., Rev. Opt., 37, 501 (1958).
54. Chabbal, R., J. Phys. Radium, 19, 295 (1958).
55. Deverall, G. V., K. W. Meissner, and G. J. Zissis, J. Opt. Soc., 43, 673 (1953).
56. Met, V., Laser Tech., 45 (1967).
57. Jacquinet, P., J. Opt. Soc. Am., 44, 761 (1954).





58. Davis, S. P., Appl. Opt., 2, 727 (1963).
59. Jacquinet, P., Rept. Progr. Phys., 23, 267 (1960).
60. O'Neill, E. L., Introduction to Statistical Optics, Addison-Wesley Publishing Co., Reading, Mass., 1963.
61. Beran, M. J., and G. B. Parrent, Jr., Theory of Partial Coherence, Prentice-Hall, Inc., Englewood Cliffs, N.J., 1964.
62. Simmons, J. W. and M. J. Guttman, States, Waves and Photons: A Modern Introduction to Light, Addison-Wesley Publishing Co., Reading, Mass., 1970.
63. Fymat, A. L., Appl. Optics, 11, 160 (1972).
64. Cooley, J. W., P. A. W. Lewis, and P. D. Welch, IEEE Trans. Audio and Electroacoustics, AU-15, 79 (1967).
65. Cooley, J. W. and J. W. Tukey, Math. Comput., 19, 297 (1965).
66. Singleton, R. C., Comm. ACM, 10, 647 (1967).
67. Singleton, R. C., Comm. ACM, 11, 773 (1968).
68. Singleton, R. C., Comm. ACM, 11, 776 (1968).
69. Ralston, A. and H. S. Wilf, Mathematical Methods for Digital Computers, John Wiley and Sons, Inc., New York, 1960.
70. Knirk, D. L., Subroutine Graph, Chem. Dept., Michigan State University, (1967).
71. Wentworth, W. E., J. Chem. Ed., 42, 96 (1965).
72. Wolberg, J. R., Prediction Analysis, Van Nostrand, Inc., Princeton, 1967.
73. Deming, W. E., Statistical Adjustment of Data, John Wiley and Sons, Inc., New York, 1943.
74. Powell, M. J. D., The Computer Journal, 7, 155 (1964).
75. Davidon, W. C., Variable Metric Method for Minimization, Argonne National Laboratory Report No. ANL 5990 (Rev.), 1959.

76. Curl, R. F. Jr., J. Comp. Phys., 6, 367 (1970).
77. Savitzky, A., and M. J. Golay, Anal. Chem., 36, 1627 (1964).
78. Bloom, A. L., Gas Lasers, John Wiley and Sons, Inc., New York, 1968.
79. Garrett, C. G. B., Gas Lasers, McGraw-Hill Book Company, New York, 1967.
80. Heard, H. G., Laser Parameter Measurements Handbook, John Wiley and Sons, Inc., New York, 1968.
81. Tomiyasu, K., The Laser Literature, Plenum Press, New York, 1968.
82. Anderson, R. J., The Depolarization of Rayleigh Scattered Light, Ph.D. Thesis, Michigan State University, 1967.
83. Collins, S. A. and R. G. White, Appl. Optics, 2, 448 (1963).
84. Moss, G. E., Appl. Optics, 10, 2565 (1971).
85. Dowley, M. W., Single Frequency Operation of Ion Lasers, Coherent Radiation Technical Bulletin 106.
86. Chiao, R. Y. and P. A. Fleury, Physics of Quantum Electronics: Conference Proceedings, ed. P. L. Kelly, B. Lax, and P. E. Tannenwald, McGraw-Hill Book Company, New York, 1966.
87. Tannahill, M., thesis to be published, 1972.
88. Yuen, H., thesis to be published, 1972.
89. Witnauer, L. P. and H. J. Scherr, Rev. Sci. Inst., 23, 99 (1952).
90. Coumou, D. J., J. Colloid Sci., 15, 408 (1960).
91. Jones, R., C. J. Oliver, and E. R. Pike, Appl. Optics, 10, 1673 (1971).
92. Foord, R., R. Jones, C. J. Oliver, and E. R. Pike, Appl. Optics, 10, 1683 (1971).
93. Young, A. T., Appl. Optics, 10, 1681 (1971).

94. Ingle, J. D. Jr. and S. R. Crough, "A Critical Comparison of Photon Counting and Direct Current Measurement Techniques for Quantitative Spectrometric Methods," to be published, also private communications.
95. Malmstadt, N. V. and C. G. Enke, Digital Electronics for Scientists, W. A. Benjamin, Inc., New York, 1969.
96. Zatzick, M. R., Research/Development, 16 (1970).
97. Fabelinskii, I. L., Molecular Scattering of Light, Plenum Press, New York, 1968.
98. Shoemaker, D. P., and C. W. Garland, Experiments in Physical Chemistry, McGraw-Hill Book Company, New York, 1962.
99. Enagonio, D. P., E. G. Pearson and C. P. Saylor, Temperature, Its Measurement and Control in Science and Industry, Reinhold Publishing Corp., New York, 1962.
100. Leite, R. C. C., R. S. Moore, and S. P. S. Porto, J. Chem. Phys., 40, 3471 (1964).
101. Dosser, L. R., An Instrument for the Measurement of the Depolarization of Rayleigh Scattered Light, M. S. thesis, Michigan State University, 1970.
102. Mallick, S., Appl. Optics, 8, 2501 (1969).
103. American Institute of Physics Handbook, 2nd ed., D. E. Gray, Ed., McGraw-Hill Book Company, New York, 1963.
104. Shapiro, S. L., M. McClintock, D. A. Jennings, and R. L. Barger, Trans. IEEE, QE-2, 89 (1966).
105. Stiso, S. N., thesis to be published 1972.
106. Miller, G. A., and C. S. Lee, J. Phys. Chem., 72, 4644 (1967).
107. Miller, G. A., F. I. San Fillippo, and D. K. Carpenter, Macromolecules, 3, 125 (1970).
108. Miller, G. A., J. Phys. Chem., 71, 2305 (1967).
109. Nordhaus, D., thesis to be published, 1972.



110. Debye, P. and A. M. Bueche, J. Appl. Phys., 20, 518 (1949).
111. Rank, D. H. and J. N. Shearer, J. Opt. Soc. Am., 46, 463 (1956).
112. Biondi, M. A., Rev. Sci. Inst., 27, 36 (1956).
113. Simic-Glavaski, B. and D. A. Jackson, J. Phys. E., 3, 660 (1970).
114. Sandercock, J. R., Opt. Comm., 2, 73 (1970).
115. Jansson, P. A., J. Opt. Soc. Am., 60, 184 (1970).
116. Day, R. A., Appl. Optics, 9, 1213 (1970).
117. Hildum, J. S., Appl. Optics, 10, 2567 (1971).
118. Smith, P. W., IEEE J. Quant. Elect., QE-1, 343 (1965); Ibid., QE-2, 666 (1966).
119. Crowell, M. H., IEEE J. Quant. Elect., QE-1, 12 (1965).
120. Pinnow, D. A., S. J. Candau, J. T. LaMacchia, and T. A. Litovitz, J. Acoust. Soc. Am., 43, 117 (1968).



## APPENDIX

### Frequency Stabilized Lasers

#### Short Plasma Tube

A laser was constructed with an optical cavity short enough that only a single axial mode lased and the frequency of this mode was stabilized by the incorporation of a Lansing Research Corporation model 80.210 lock-in stabilizer. The laser is schematically represented in Figure 10.1.

The plasma tube is a 1 mm bore, 12 cm long tube with Brewster end windows and is filled with a 7:1 mixture of the  $^3\text{He}$  and  $^{20}\text{Ne}$  gases at a total pressure of 3.6 torr. A Jodon model PS-100 power supply provides dc excitation to the coaxial, hot cathode electrode system. The cathode is operated at 6.2 volts and 1.46 amperes. The plasma saturation current is 4.2 ma; cathode-anode voltage is 500 volts. This bore diameter, total gas pressure, helium neon ratio and exciting current correspond to optimum output power. Utilization of  $^3\text{He}$  and  $^{20}\text{Ne}$  isotopes insure a significant Lamb dip in output power versus mirror separation alleviating frequency stabilization difficulties.

The tube was clamped into a block of Invar which in turn was bolted to an Invar plate. The mirror

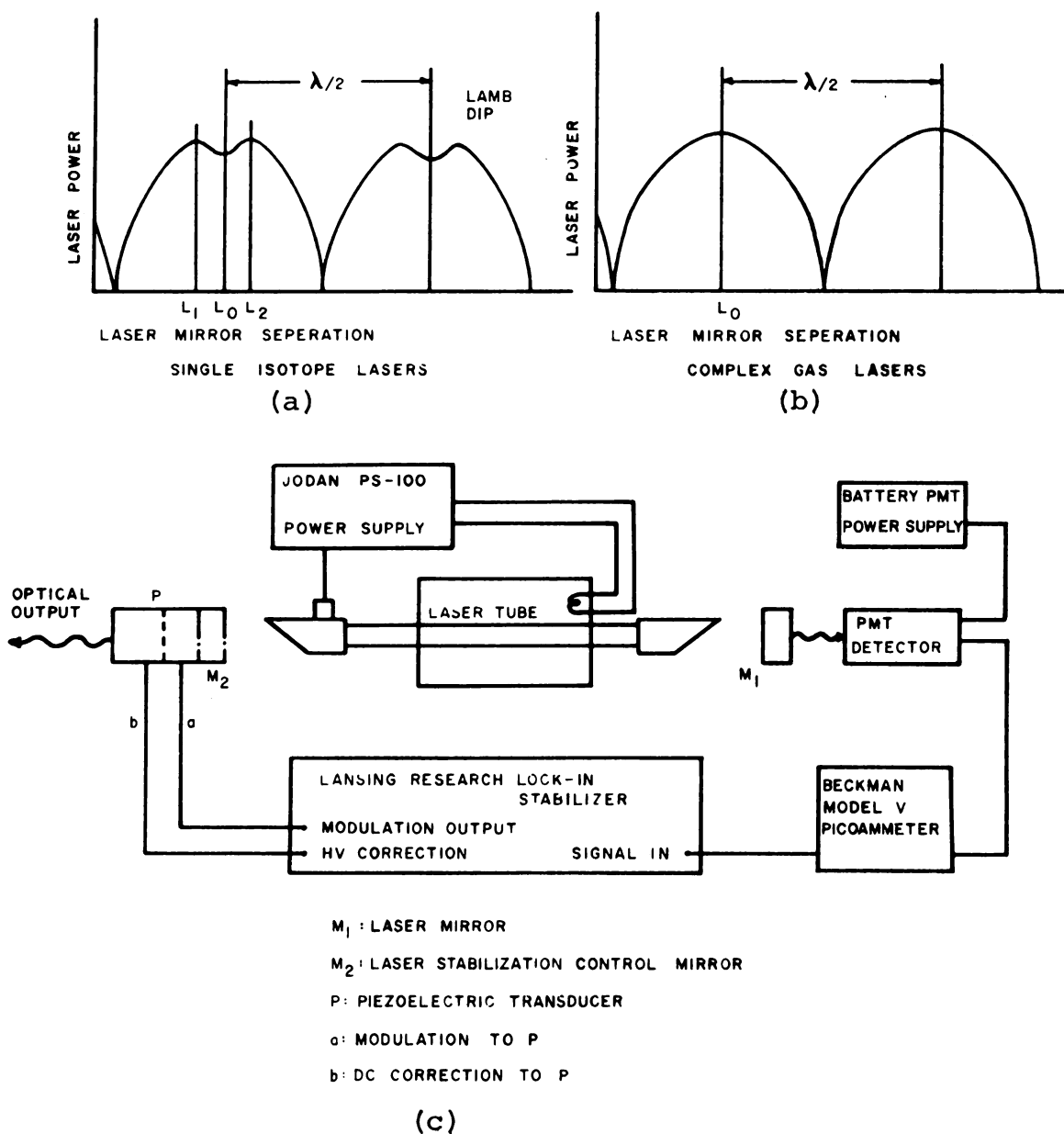


Figure 10.1. Frequency Stabilized Short Plasma Tube Laser.



holders were also bolted to this Invar plate so that the mirrors were 15 cm apart. Note that mirror spacing is the parameter dominant in causing the laser to lase in a single axial mode. The small tube diameter does not allow other off axis modes to lase. Unfortunately, this single mode technique compromises output power; when properly aligned, the laser's output power exceeds 230  $\mu$ watts.

Both high precision gimbal mounts were purchased from Lansing Research. One mount has an adaptor for a one-inch diameter mirror; the other mount has a two input option, piezoelectric translator (model 21.8.4) with an adaptor for a one-inch diameter mirror. Both mirrors are Oriel  $\lambda/20$ , one-inch diameter, two meter radius mirrors. One mirror is coated for a reflectance as close to 100% as is practical; the output mirror is coated for 99.5% reflectance at 6328  $\text{\AA}$ .

Optical alignment is achieved by using another laser to define an optical axis coincident with the bore of the laser tube. The far-end mirror is mounted and adjusted until the incident beam reflects back onto itself as closely as can be judged visually. Then the other mirror is mounted and adjusted so that the beam reflected from the mirror's back surface is coincident with the incident beam. Since the mirrors are slightly wedge-shaped, the present status does not correspond to correct alignment; however, it is close enough that with systematic rocking of the micrometer's, the system can be brought into sufficient alignment to cause

lasing. To optimize, all four micrometers are systematically varied to maximize the optical output power. Now frequency stabilization is accomplished by following the extensive procedure explained in the lock-in stabilizer's manual.

Two frequency selective elements are present in every laser: (1) The laser medium exhibits a useful gain over a frequency range centered near the optical transition frequency  $\nu_0$ . (2) The optical cavity which exhibits high Q modes at integral multiples of  $c/2L$ .  $c$  is the phase velocity of light in the optical medium and  $L$  is the length of the optical resonator, that is, the mirror spacing. This  $c/2L$  spacing is analogous to the free spectral range of a Fabry-Perot interferometer under the approximation of large radius spherical surfaces to plane surfaces over a small region. Several resonator mode frequencies lie within the frequency range over which the laser medium's optical gain exceeds optical loss; therefore, the laser may oscillate at several frequencies. For inhomogeneously broadened optical transitions, e.g. Doppler broadening, the laser will oscillate simultaneously at each mode frequency for which the gain exceeds the loss. The simultaneous oscillations are not truly independent; through the action of optical saturation of gain about each oscillating mode, the resonator modes couple to stimulate atoms to emit. The resulting mode competition introduces instability. Also,



in multimode operation, the available output power is distributed among the competing modes.

Since the  $Q$  of the optical resonator is typically much higher than the  $Q$  of the medium's emission line, the frequency of the resonator mode determines the frequency of oscillation, to within first order. High order effects arise from dispersion in the medium and "mode pushing". However, a resonator functioning near  $\nu_0$  is very nearly independent of these high order effects. This is the condition achieved for laser stabilization.

Since the optical resonator frequencies are a strong function of the resonator's length, laser stabilization may be accomplished by the stabilization of the optical path length of the resonator.

While many schemes for stabilization have been devised (see Tomiyasu's bibliography) only two were practical until very recently: One is "stabilization to the Lamb dip" or maximizing the output power and is used for this short plasma tube laser. The second scheme is the locking of a resonant cavity interferometer (internal or external) to a laser line. It was used for the long plasma tube laser. The latter technique is very similar to the technique adapted in the very recently, commercially available frequency stabilized lasers. Even though not presently practical for many applications, another method of stabilization worth consideration for some applications



is the "four mirror stabilization of long lasers" discussed by Smith (118).

When  $c/2L$  exceeds the Doppler width, only one optical resonator mode has enough gain to sustain oscillation. The laser's optical output power will vary as shown in Figure 10.1(a) when  $L$  is varied by  $\lambda/2$  so that the resonator mode sweeps over the gain region. The dip in laser power at  $\nu_0$  is the Lamb dip and is a very significant feature in low power, single isotope lasers. When this dip does not exist, the stabilization system can be locked to a power peak.

A system for stabilizing the laser to the Lamb dip frequency,  $\nu_0$ , is illustrated in Figure 10.1(c). The position of mirror 2 is sinusoidally modulated (A voltage corresponding to a small fraction of  $\lambda/2$  is applied to the piezoelectric mounting element P.) thereby modulating the optical resonator length and hence the optical resonator's mode frequency. The laser output power is thereby sinusoidally modulated at this modulation frequency with the following characteristics, provided the modulation amplitude is small: The modulation index is zero when the mode frequency is  $\nu_0$  since the slope of the laser power output versus  $\nu$  is zero for  $\nu$  equal to  $\nu_0$ . The phase of the modulated component of the laser power relative to the modulating voltage applied to P is opposite for  $\nu > \nu_0$  relative to the phase for which  $\nu < \nu_0$ . The modulated



component of the laser power is detected, preamplified and phase sensitively detected in the Lansing Research model 80.210 lock-in stabilizer. The phase sensitively detected signal, after filtering, provides a discriminator signal which is zero for resonator lengths corresponding to a mode frequency  $\nu_0$ . It is positive on one side of  $\nu_0$  and negative on the other side of  $\nu_0$ . This discriminator signal is dc amplified and applied to the piezoelectric translator P with a phase appropriate for stable negative feedback. The result is that the resonator's length is controlled in a manner insuring optical oscillation only at  $\nu_0$ .

The mode structure of the stabilized laser was studied with the use of the Spectra-Physics model 420 optical spectrum analyzer plug-in unit and a Tektronix 564B oscilloscope. It was truly a single mode laser. Instantaneously, the laser's bandwidth was about 35 MHz and the stabilizer held the center frequency constant to within about 48 MHz for several hours before it would seriously drift. The stability may be improved with a temperature controlled housing for the laser. However, because of the low output power, and other problems of the instrumental system, research and application of this laser was abandoned. Even if the low intensity could be tolerated with photon counting detection, alignment difficulties arise from the non visibility of a scattered beam along the optical detection train.





### Long Plasma Tube

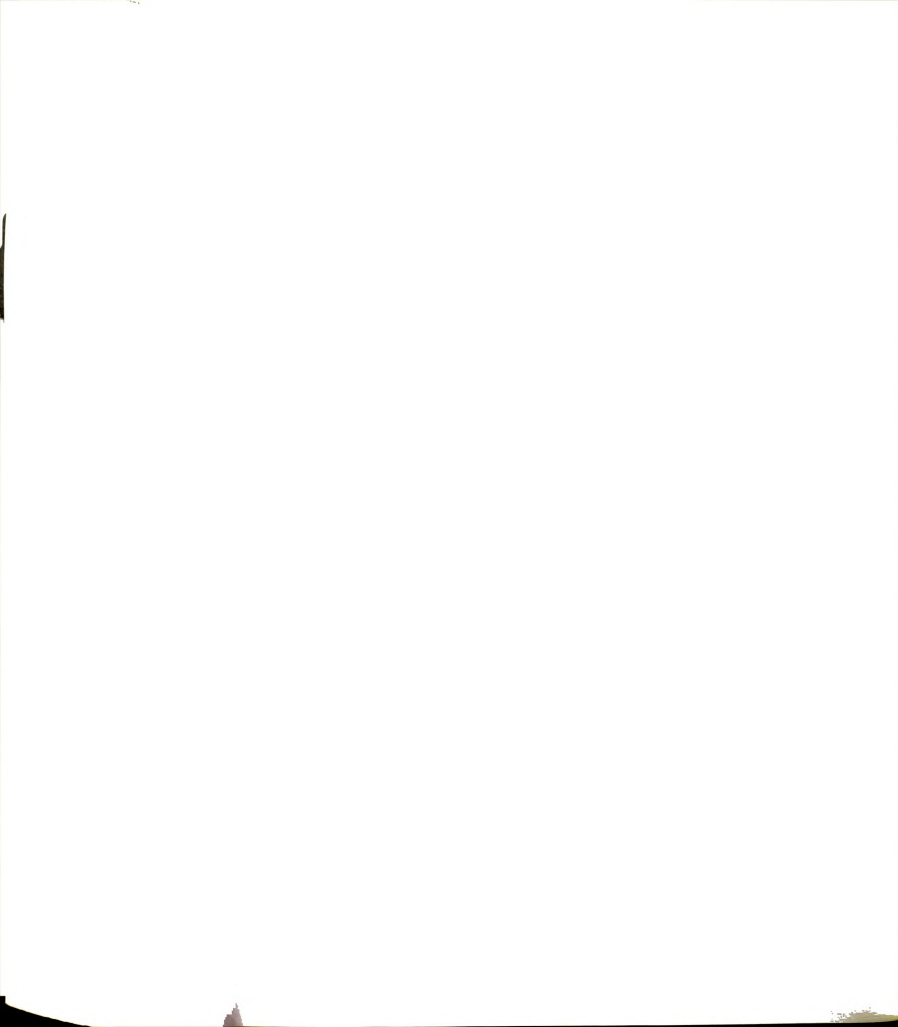
A second laser was constructed to provide a single mode output of greater intensity. Stabilization was to be achieved by locking an external interferometer cavity, functioning as a filter, to one of the laser's frequency modes which had been stabilized by AM or FM mode locking. Tomiyasu (81) and Crowell (119) provide a good explanation of these mode locking schemes.

The frequency locking of the laser to an external resonant interferometer cavity was investigated. It is the second technique referred to in the previous section and a good introduction is Met's "Working with Etalons" (56). Briefly, this technique amounts to the locking of a narrow bandwidth optical filter to one of the laser's oscillating (axial) modes. An interferometer with piezoelectric control of one of its mirrors was used in a manner similar to that described in the previous section. The laser's output was passed through this external interferometer cavity (a Tropel model 240 interferometer normally used as a spectrum analyzer) whose piezoelectrically mounted mirror was modulated. The resulting correction voltage was applied to the piezoelectric mount in a manner which maximized the transmitted power. Thus, the inherently multi-mode laser was filtered to yield a single frequency output.

This laser design is illustrated in Figure 10.2. The laser tube is a commercial 3 mm bore, 90 cm long tube filled with a helium-neon gas mixture to yield a maximum output of 58 milliwatts functioning in a multimode fashion. It has a hot cathode in a bulb connected to the center of the tube and anodes near each end. Brewster windows were attached via ground glass joints to allow them to be aligned relative to one another. Magnets are mounted along the tube utilizing the Zeeman effect to suppress laser oscillation at  $3.39 \mu$  which competes significantly with the lines  $6328 \text{ \AA}$  for long plasma tubes. A Sorensen model QB6-8 dc power supply was used to excite the hot cathode with 6.3 volts and 3.4 amp. The anode-cathode voltage (1800 volts) which optimized the output was supplied by an Alfred model 233A regulated high voltage power supply. The total current was 32 ma. The tube was mounted at two points, with modified microscope x-y positioners, to an optical rail.

The mirrors were both Oriel  $\lambda/20$ , one-inch diameter, two meter radius mirrors. One mirror was coated for nearly 100% reflectance and the other mirror was coated for 97% reflectance. They were spaced about 95 cm apart and mounted in Lansing Research model GS-203 gimbal mounts which in turn were mounted onto the optical rail.

After the laser was aligned using the technique described in the previous section, it was stabilized using



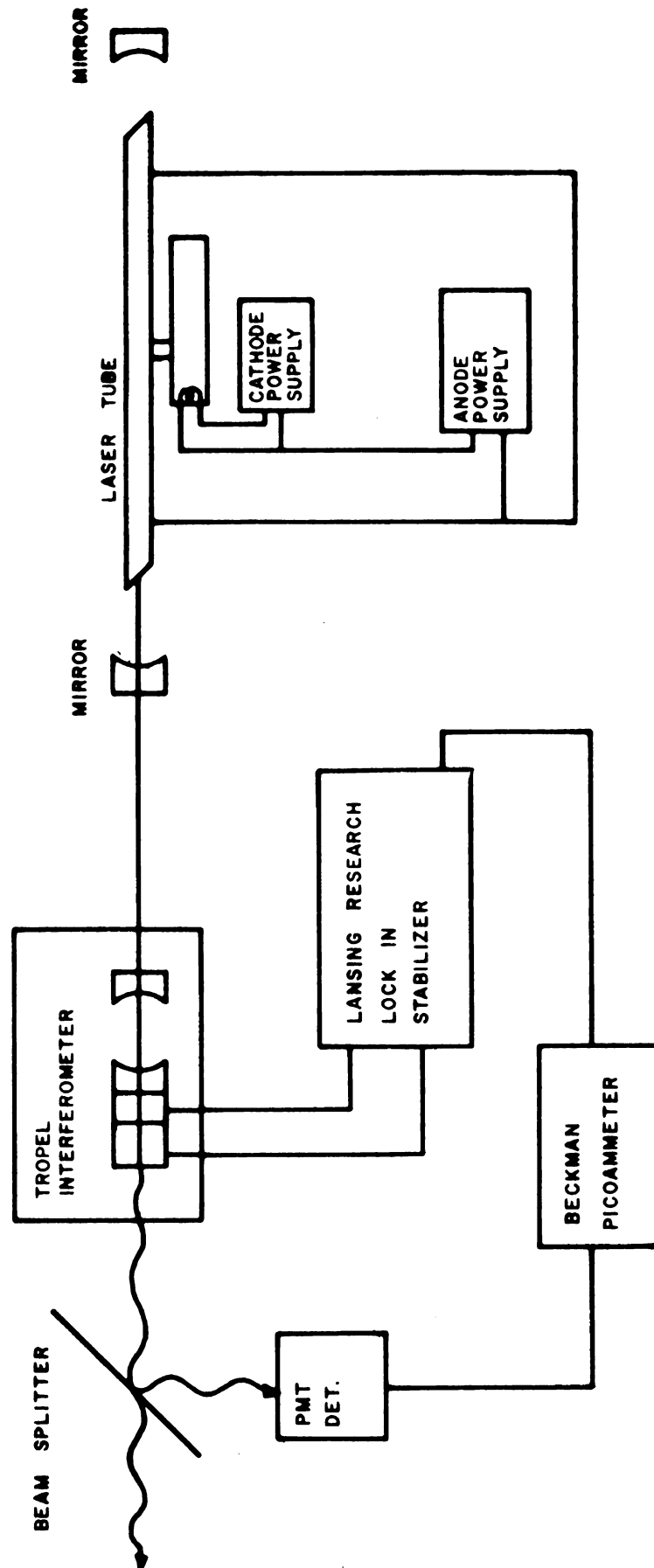


Figure 10.2. Frequency Stabilized Long Plasma Tube Laser.

the Lansing Research lock-in stabilizer coupled to the Tropel interferometer. After optimizing the laser's parameters, its multimode output power was 38 milliwatts; when "filtered," a maximum output power of 4.1 milliwatts was obtained. The bandwidth of the "filtered" laser beam was 7 Mc, instantaneously. However, the center frequency of this band drifted seriously because the laser was not yet mode locked.

During the investigation of this long laser tube's properties, two difficulties with the plasma tube became apparent. The tube tended to twist with time causing the Brewster windows to misalign and reduce the laser's output power. Secondly, the tube was warping, decreasing the effective volume of the active media hence decreasing the output power.

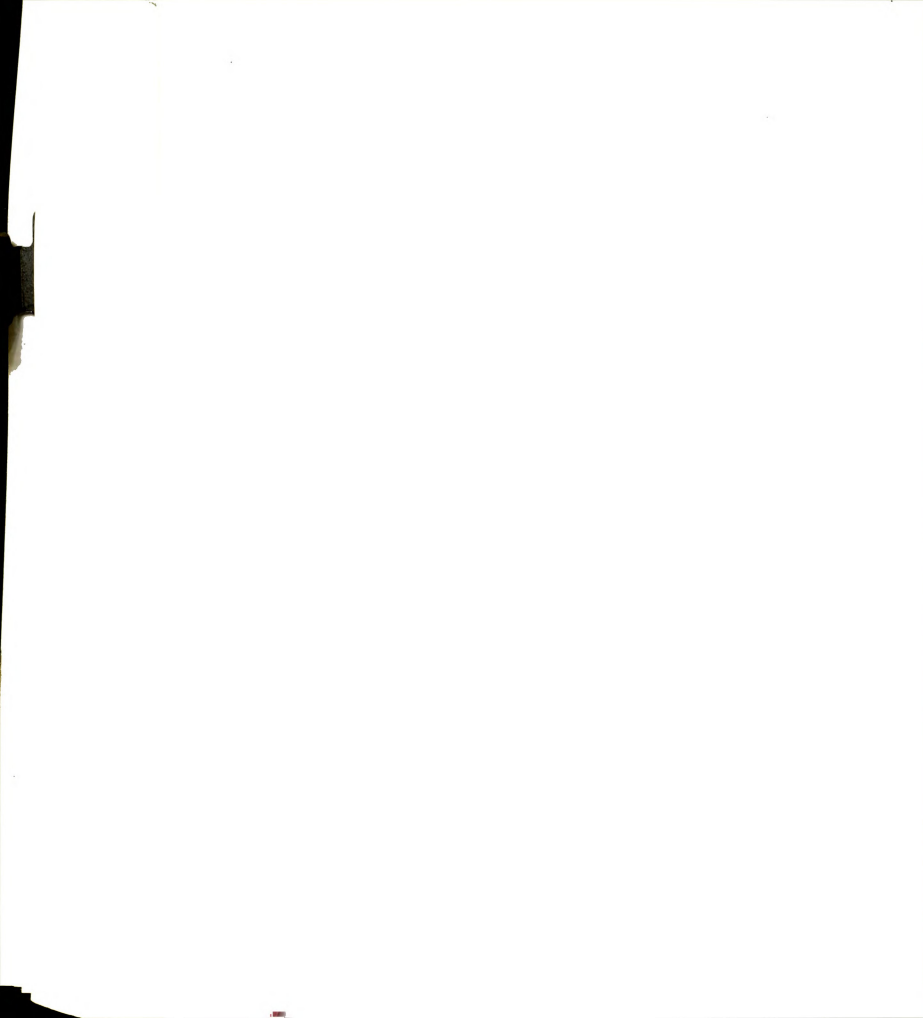


















MICHIGAN STATE UNIVERSITY LIBRARIES



3 1293 03061 2331